

## Article

# Compositional and Numerical Geomorphology Along a Basement–Foreland Transition, SE Germany, with Special Reference to Landscape-Forming Indices and Parameters in Genetic and Applied Terrain Analyses

Harald G. Dill <sup>1,\*</sup> , Andrei Buzatu <sup>2</sup>, Sorin-Ionut Balaban <sup>3</sup> and Christopher Kleyer <sup>4</sup>

<sup>1</sup> Department of Mineralogy, Gottfried Wilhelm Leibniz University, Welfengarten 1, D-30167 Hannover, Germany

<sup>2</sup> Department of Geology, Faculty of Geography and Geology, “Alexandru Ioan Cuza” University of Iași, 20A, Carol I Boulevard, RO-700505 Iași, Romania; buzatu\_andrei@yahoo.com

<sup>3</sup> Department of Earth and Planetary Sciences Birkbeck, University of London Malet Street, Bloomsbury, London WC1E 7HX, UK; balaban\_sorin\_ionut@yahoo.com

<sup>4</sup> Department of Geology, Gottfried Wilhelm Leibniz University, Welfengarten 1, D-30167 Hannover, Germany; chriskeyer72@googlemail.com

\* Correspondence: haralddill@web.de

**Abstract:** The Münchberg Gneiss Complex (Central European Variscides, Germany) is separated by a deep-seated lineamentary fault zone, the Franconian Lineamentary Fault Zone, from its Mesozoic foreland. The study area offers insight into a great variety of landforms created by fluvial and mass wasting processes together with their bedrocks, covering the full range from unmetamorphosed sediments to high-grade regionally metamorphic rocks. It renders the region an ideal place to conduct a study of compositional and numerical geomorphology and their landscape-forming indices and parameters. The landforms under consideration are sculpted out of the bedrocks (erosional landforms) and overlain by depositional landforms which are discussed by means of numerical landform indices (LFIs), all of which are coined for the first time in the current paper. They are designed to be suitable for applied geosciences such as extractive/economic geology as well as environmental geology. The erosional landform series are subdivided into three categories: (1) The landscape roughness indices, e.g.,  $VeSi_{val}$  (vertical sinuosity—valley of landform series) and the  $VaSlAn_{alti}$  (variation in slope angle altitude), which are used for a first order classification of landscapes into relief generations. The second order classification LFIs are devoted to the material properties of the landforms’ bedrocks, such as the rock strength ( $VeSi_{lith}$ ) and the bedrock anisotropy ( $VaSlAn_{norm}$ ). The third order scheme describes the hydrography as to its vertical changes by the inclination of the talweg and the different types of knickpoints ( $IncTal_{lith/grad}$ ) and horizontal sinuosity ( $HoSi_{lith/grad}$ ). The study area is subjected to a tripartite zonation into the headwater zone, synonymous with the paleoplain which undergoes some dissection at its edge, the step-fault plain representative of the track zone which undergoes widespread fluvial piracy, and the foreland plains which act as an intermediate sedimentary trap named the deposition zone. The area can be described in space and time with these landform indices reflecting fluvial and mass wasting processes operative in four different stages (around 17 Ma, 6 to 4 Ma, <1.7 Ma, and <0.4 Ma). The various groups of LFIs are a function of landscape maturity (pre-mature, mature, and super-mature). The depositional landforms are numerically defined in the same way and only differ from each other by their subscripts. Their set of LFIs is a mirror image of the composition of depositional landforms in relation to their grain size. The leading part of the acronym, such as  $QuantSan_{heav}$  and  $QuantGrav_{lith}$ , refers to the process of quantification, the second part to the grain size, such as sand and gravel,



Academic Editor: Paul R. Eizenhöfer

Received: 28 October 2024

Revised: 26 December 2024

Accepted: 26 December 2024

Published: 23 January 2025

**Citation:** Dill, H.G.; Buzatu, A.; Balaban, S.-I.; Kleyer, C. Compositional and Numerical Geomorphology Along a Basement–Foreland Transition, SE Germany, with Special Reference to Landscape-Forming Indices and Parameters in Genetic and Applied Terrain Analyses. *Geosciences* **2025**, *15*, 37. <https://doi.org/10.3390/geosciences15020037>

**Copyright:** © 2025 by the authors. Licensee MDPI, Basel, Switzerland. This article is an open access article distributed under the terms and conditions of the Creative Commons Attribution (CC BY) license (<https://creativecommons.org/licenses/by/4.0/>).

and the subscript to the material, such as heavy minerals or lithological fragments. The three numerical indices applicable to depositional landforms are a direct measurement of the hydrodynamic and gravity-driven conditions of the fluvial and mass wasting processes using granulometry, grain morphology, and situmetry (clast orientation). Together with the previous compositional indices, the latter directly translate into the provenance analysis which can be used for environmental analyses and as a tool for mineral exploration. It creates a network between numerical geomorphology, geomorphometry, and the E&E issue disciplines (economic/extractive geology vs. environmental geology). The linguistics of the LFIs adopted in this publication are designed so as to be open for individual amendments by the reader. An easy adaptation to different landform suites worldwide, irrespective of their climatic conditions, geodynamic setting, and age of formation, is feasible due to the use of a software and a database available on a global basis.

**Keywords:** numerical geomorphology; basement–foreland transition; landform indices; mineralogical composition; Cenozoic

---

## 1. Introduction

The current mineralogical terrain analysis encompasses descriptive key elements known from the classical geomorphology with the focus placed on fluvial and mass wasting processes along a basement–foreland transition [1–8]. The main emphasis, however, is placed on a more numerical approach to landforms and landform series singled out as an entity of its own called geomorphometry [9–16]. The current study acts as a bridge between the classical geomorphology and geomorphometry when it comes to geomorphological environment analysis by providing numerical landform reference data beyond common sedimentary and geomorphological indices, such as stream gradient index (SL), channel steepness (ks), or erosion rate index (E), used during the examination of landforms and their evolution. The current type of publication lies between a research article and a manual, and it is intended to make the data applicable for genetic as well as applied geosciences using it as a tool for mineral exploration in economic geology to predict target landforms and landscapes that are promising in the search for mineral deposits [17–22].

That is why the current terrain analysis is combined with mineralogy, adding a compositional element to the land-forming processes, and supplemented with geochronological data from the literature to bolster the evolution of the reference landscape under study [23]. The scope of the present study is as follows:

1. To provide compositional and numerical landform data and discuss them as a function of the tripartite landscape maturity (pre-mature, mature, and super-mature)
2. To study the evolution of erosional and depositional landforms in relation to their bedrock composition and characterize them by landform indices (LFIs).
3. To discuss these landscape-forming indices on different scales regarding lithology, altitude, and gradient and last-but-not least to elaborate facies markers for environment analysis.
4. To bridge the gap between genetic and applied geomorphology so as to make them useful for extractive and environmental geology. Due to the senior author's focal disciplines, emphasis is placed on applied geomorphology in the search for mineral deposits from Al to Zr [24].

Table 1 constitutes the key elements for the understanding of the ensuing sections.

**Table 1.** Terminology, definitions, and applications of landscape-forming indices.

(a) Overview and definitions of the landscape-forming indices, their general applications and their presentation. Shaded fields denote methods of particular interest for mineral exploration (“till exploration”).

Code of Land-Forming Index	Definition and Terminology of Land-Forming Index	Remarks (e.g., Application)
VeSi <sub>val</sub>	Vertical Sinuosity-Valley	Landform series and relief of landscape
VaSlAn <sub>alti</sub>	Variation of Slope Angle altitude	Inclination of the slope angle given in degree of a certain landscape
VeSi <sub>lith</sub>	Vertical Sinuosity-Lithology of landform	Rock strength of bedrocks which landforms have derived from
VaSlAn <sub>norm</sub>	Variation of Slope Angle normalized	Bedrock anisotropy of landforms built upon
IncTal <sub>lith/grad</sub>	Inclination of the Talweg-Lithology plus Gradient	Vertical changes of the talweg caused by changes of the bedrock lithology and the (paleo)gradient. The LFI describes the hydrography as to its vertical changes by the inclination of the talweg and the different types of knickpoints
HoSi <sub>lith/grad</sub>	Horizontal Sinuosity—Lithology plus Gradient	Horizontal changes of the talweg caused by changes of the bedrock lithology and (paleo)gradient. A straight line shows a sinuosity index of 1
Quant <sub>flu/mas</sub>	Quantification of Fluvial-Mass wasting deposits	This index reflects the aerial distribution of mass wasting and fluvial deposits in a 2D illustration of depositional landforms. The index data are presented in histograms and sector diagrams
QuantClaSil	Quantification Clay-silt-sized fraction	This index has only been handled qualitatively for technical reasons. Only the Rietveld refinement applied during XRD can provide reliable numerical results
QuantSan <sub>/ligh</sub>	Quantification Sand-sized light minerals fraction	This index is measure by means of thin sections and XRD and the data are presented in pie chart diagrams
QuantSan <sub>heav</sub>	Quantification Sand-sized heavy minerals	This index is measure by means of thin sections and XRD and the data are presented in pie chart diagrams
QuantGrav <sub>lith</sub>	Quantification Gravel-sized lithologies	This index is measure by means of thin section and the data are presented in pie-chart diagrams
QuantGrav <sub>gran/sort/mod</sub>	Quantification done during Gravel granulometry. Part of the GMS method (granulometry, morphometry and situmetry)	The data are on display as sorting coefficient and modality both of which translate into an environment analysis of the depositional coarse-grained landform series
QuantGrav <sub>morp/roun/cycl</sub>	Quantification done during Gravel morphometry. Part of the GMS method (granulometry, morphometry and situmetry)	The most efficient diagnostic parameters for the grain analysis are roundness and circularity
QuantGrav <sub>situ/dire/shar</sub>	Quantification done during Gravel situmetry (vertical arrangement, e.g., shingle-like, and horizontal orientation of elongated gravel-sized fragments.	The 2D/3D position of gravel-sized fragments is measured by the direction (360°). The results are displayed by rose diagrams where the intensity of individual flows is determined by the sharpness of their maxima

(b) Synoptical numerical and verbal overview of the three morphotectonic units vs. geomorphology, topography, and mineralogy/lithology and landscape-forming indices in the current reference paper used to introduce these landscape-forming indices.

Indices and Parameters	Geomorphological Reference Plains		
	Foreland Plains	Step-Fault Plain	Paleoplain
<b>Topography</b> (lowest and highest level a.m.s.l = above mean sea level)	Schorgast flood plain in an asymmetric rift valley min. 320 m. Top fault escarpment of FLFZ max. 510 m.	Top fault scarp of FLFZ min. 510 m crest slope/shoulder max. 590 m.	Mountain max. height Weissenstein 668 m, planed uplands 620 m, min. crest slope/shoulder 550 to 500 m.
<b>Morphodynamic units and their tectonic contacts</b>	Deep-seated lineamentary fault zone (several 100 km) striking NW-SE.	Sets of internal shear zones (several 10 km) striking NW-SE.	Fault and warp zones. Anticline plunging towards the NE (several 10 km).
<b>Geological age of bedrocks</b>	Cenozoic, Late Triassic, and Late Permian.	Cambrian to Lower Carboniferous.	Neoproterozoic to Ordovician.
<b>Lithology of bedrocks</b> (Numbers in brackets for reference see Figure 2a,b)	Sandstones and claystones, gravel, sand, and clay (18,19–21).	Slate, metabasalt, chert, tuffaceous slate (15–17), epidote amphibolite, phyllite, talc schist (12–14), and amphibolite (11).	Layered amphibolitic gneiss, eclogite amphibolite, garnet amphibolite, eclogite, meta-ultramafic rocks (serpentinite), pegmatoid (5–10), augengneiss, meta-granodiorite, meta-gabbro, paragneiss/meta hornfels, muscovite-biotite gneiss alternating with tourmaline-garnet-plagioclase gneiss, and muscovite-biotite gneiss (1–6).

Table 1. Cont.

Indices and Parameters	Geomorphological Reference Plains		
	Foreland Plains	Step-Fault Plain	Paleoplain
<p style="writing-mode: vertical-rl; transform: rotate(180deg);">Erosional landform series —landscape roughness indices—</p> <p><b>Regional scale</b> Vertical sinuosity—valley (VeSi<sub>val</sub>) of landform series</p>	<p>Relief generation 4: 1.094 ⇒ 1.079 pediments dissected by fluvial and mass wasting processes</p>	<p>Relief generation 2 relic: 1.132 ⇒ 1.149 moderately bosselated and dissected pediment-cuesta Relief generation 3: 1.232 ⇒ 1.115 bosselated to rugged</p>	<p>Relief generation 0 (outside working area Frankenwald): 1.1400 ⇒ 1.129 bosselated landscape—mountain summit Relief generation 1: 1.150 ⇒ 1.123 bosselated landscape Relief generation 2: 1.416 ⇒ 1.224 strongly rugged 1.186 ⇒ 1.134) moderately bosselated/rolling hill landscape. 1.113 ⇒ 1.038 slightly bosselated to flat</p>
	<p><b>Local scale</b> Variation in slope angle altitude (VaSlAn<sub>alti</sub>) index (in brackets slope angle in degree)</p>	<p>Relief generation 4: 450–350 m Plateau gently sloping crest shoulder escarpment (2–7) Escarpment face (18–19) V-shaped wide angle valley+ Erosional terraces (13–17) Hogback-resistant hill (11–13)</p>	<p>Relief generation 2 relic: 550–450 m Large and shallow valley (2–4) V-shaped valley wide angle /2 generations (8–17) Relief generation 3: 450–350 m V-shaped valley acute angle (22–23) Erosional fluvial terrace (0–2) Floodplain (0–1) V-shaped valley wide to acute telescoped into each other (16–32) Resistant hill (16–18) Gently sloping plateau—crest shoulder escarpment (5–8) Staircase-like terraces slip bank (5–11) Escarpment face-cut bank (24–26)</p>

Table 1. Cont.

Indices and Parameters		Geomorphological Reference Plains		
		Foreland Plains	Step-Fault Plain	Paleoplain
Erosional landforms —material properties of bedrock	<b>Rock strength</b> Vertical sinuosity—lithology of landform (VeSi <sub>lith</sub> )	Sandstones with intercalated Max: 582, mean: 216	Phyllite Max: 479, mean: 177 Slate Max: 197, mean: 159 Chert alternating with thin interbeds of slates and tuffaceous layers Max: 320, mean: 156 Talc schists 421 Amphibolite-epidote amphibolite Max: 329, mean: 160 Epidote amphibolite (“prasinite”, “meta diabase”) Max: 309, mean: 127 Meta-basalt (“diabase”) Max: 685, mean: 248	Muscovite-biotite gneiss Max: 663, mean: 266 Muscovite-biotite gneiss alternating with tourmaline-garnet-plagioclase gneiss (composite lithology) Max: 271, mean: 184 Paragneiss—meta-hornfels Max: 1197, mean: 402 Augengneiss (meta-granite) Max: 855, mean: 446 Meta-gabbro plus meta-granodiorite Max: 687, mean: 301 Meta-ultramafite Max: 989, mean: 778 Eclogite Max: 1292, mean: 572 Eclogite amphibolite—garnet amphibolite Max: 1292, mean: 572 Layered amphibolitic gneisses in eclogite and amphibolite facies Max: 563, mean: 256 Muscovite-biotite gneiss Max: 6.970, mean: 2.868 Muscovite-biotite gneiss alternating with tourmaline-garnet-plagioclase gneiss (composite lithology) Max: 2.983, mean: 2.237 Paragneiss—meta-hornfels Max: 6.094, mean: 2.470 Augengneiss (meta-granite) Max: 6.923, mean: 3.177 Meta-gabbro plus meta-granodiorite Max: 3.765, mean: 2.181 Meta-ultramafite Max: 3.181, mean: 2.512 Eclogite Max: 1.817, mean: 1.638 Eclogite amphibolite-garnet amphibolite Max: 1.817, mean: 1.638 Layered amphibolitic gneisses in eclogite and amphibolite facies Max: 2.777, mean: 1.937
	<b>Bedrock anisotropy</b> Variation in normalized slope angle of landform (VaSlAn <sub>norm</sub> )	Sandstones with intercalated Max: 3.173, mean: 1.458	Phyllite Max: 4.986, mean: 2.488 Slate Max: 3.381, mean: 1.818 Chert alternating with thin interbeds of slates and tuffaceous layers Max: 3.628, mean: 2.422 Talc schists 2.375 Amphibolite-epidote amphibolite Max: 4.649, mean: 2.787 Epidote amphibolite (“prasinite”, “meta diabase”) Max: 5.460, mean: 3.138 Meta-basalt (“diabase”) Max: 5.400, mean: 2.734	Muscovite-biotite gneiss alternating with tourmaline-garnet-plagioclase gneiss (composite lithology) Max: 6.094, mean: 2.470 Augengneiss (meta-granite) Max: 6.923, mean: 3.177 Meta-gabbro plus meta-granodiorite Max: 3.765, mean: 2.181 Meta-ultramafite Max: 3.181, mean: 2.512 Eclogite Max: 1.817, mean: 1.638 Eclogite amphibolite-garnet amphibolite Max: 1.817, mean: 1.638 Layered amphibolitic gneisses in eclogite and amphibolite facies Max: 2.777, mean: 1.937
Erosional landforms —vertical and horizontal hydrography	<b>Vertical</b> Inclination of the talweg—lithology plus gradient (IncTal <sub>lith/grad</sub> ) + knickpoints	Relief generation 4: Knickpoint: 0 Min: 0.388, mean: 1.583, max: 4.542	Relief generation 2 relic: Knickpoint: 2 Min: 0.605, mean: 1.469, max: 2.471 Relief generation 3: Knickpoint: 7 Min: 0.236, mean: 2.043, max: 5.521	Relief generation 1: Knickpoint: 3 Min: 0.199, mean: 1.842, max: 6.996 Relief generation 2: Knickpoint: 7 Min: 0.381, mean: 1.514, max: 4.243
	<b>Horizontal</b> Horizontal sinuosity—lithology plus gradient (HoSi <sub>lith/grad</sub> ):	Relief generation 4: Min: 1.080, max: 1.314	Relief generation 2 relic 2: Min: 1.075, max: 1.203 Relief generation 3: Min: 1.102, max: 1.322	Relief generation 1: Min: 1.088, max: 1.312 Relief generation 2: Min: 1.257, max: 1.513

Table 1. Cont.

Indices and Parameters	Geomorphological Reference Plains			
	Foreland Plains	Step-Fault Plain	Paleoplain	
Depositional landforms —grain size and composition	Quantification of fluvial–mass wasting deposits (Quant <sub>flu/mas</sub> ) MWD = mass wasting deposit FDD = fluvial drainage deposit MTD = fluvial–mass wasting mixed-type deposit	MWD: min. 0.02, max. 3.13% km <sup>2</sup> FDD: min: 0.03, max. 2.80% km <sup>2</sup> MTD: min. 0.0, max. 3.44% km <sup>2</sup> <u>M/F ratio = 1.12</u>	MWD: min. 0.06, max. 0.60% km <sup>2</sup> FDD: min: 0.13, max. 0.89% km <sup>2</sup> <u>M/F ratio = 0.67</u>	MWD: min. 0.77, max. 2.30% km <sup>2</sup> FDD: min: 0.13, max. 0.89% km <sup>2</sup> <u>M/F ratio = 2.58</u>
	Quantification of clay-silt-sized fraction (Quant <sub>Clasil</sub> )	Muscovite > illite > chlorite (only relative abundance)	Muscovite > illite > chlorite > talc (only relative abundance)	Muscovite > illite > kaolinite chlorite > vermiculite > talc > serpentine (lizardite) (only relative abundance)
	Quantification of sand-sized light minerals fraction (Quant <sub>San/lig</sub> )	Na feldspar, quartz, K feldspar (for numerical data, see Figure 11a)	Quartz, Na feldspar, plagioclase, K feldspar (for numerical data, see Figure 11a)	Quartz, K feldspar, Na feldspar, plagioclase (for numerical data, see Figure 11a)
	Quantification of sand-sized heavy minerals (Quant <sub>San/heav</sub> )	Amphibole > garnet > zoisite > pyroxene > epidote > “limonite” > rutile > apatite > anatase > titanite > zircon (only relative abundance)	Amphibole (pargasite, hastingsite) “limonite”, garnet, omphacite, zoisite, epidote, rutile, anatase, titanite apatite, zircon (for numerical data, see Figure 11b)	“Limonite”, magnetite, amphibole (grunerite), garnet, epidote, omphacite, diopside, zoisite, rutile, anatase, titanite (for numerical data, see Figure 11b)
	Quantification of gravel-sized lithologies (Quant <sub>Grav/lith</sub> )	Ferricretes > chert > conglomerate > graywacke > metabasalt (only relative abundance)	Meta-basalt (“diabase”), slate, greywacke, mica gneiss, meta-trachyte (“keratophyre”), chert, quartz-conglomerate, phyllite, amphibolite, meta-hornfels, quartz-aggregate, prasinite, pyrite ore, carbonate aggregate, Fe slags, ferricretes (for numerical data, see Figure 11c)	Amphibolite, mica gneiss, quartz-aggregate, granitoid, meta-hornfels, ferricretes, augengneiss, meta-granodiorite (for numerical data, see Figure 11c)
	Quantification of gravel granulometry Quant <sub>Grav<sup>gran/sort/mod</sup></sub> - Sorting - Modality	Quant <sub>Grav<sup>gran/sort</sup></sub> Min: 1.581, max: 1.788 Quant <sub>Grav<sup>gran/mod</sup></sub> Unimodal (for locality, see Figure 13a,b)	Quant <sub>Grav<sup>gran/sort</sup></sub> Min: 1.699, max: 3.576 Quant <sub>Grav<sup>gran/mod</sup></sub> Uni-, bi-, and trimodal (for locality, see Figure 13a,b)	Quant <sub>Grav<sup>gran/sort</sup></sub> Min: 1.454, max: 1.946 Quant <sub>Grav<sup>gran/mod</sup></sub> Unimodal (for locality, see Figure 13a,b)
Quantification of gravel morphometry Quant <sub>Grav<sup>morp/roun/cycl</sup></sub> - Roundness - Circularity	Quant <sub>Grav<sup>morp/roun</sup></sub> Min: 0.427, max: 0.958 Quant <sub>Grav<sup>morp/cycl</sup></sub> Min: 0.629, max: 0.878	Quant <sub>Grav<sup>morp/roun</sup></sub> Min: 0.479, max: 0.932 Quant <sub>Grav<sup>morp/cycl</sup></sub> Min: 0.665, max: 0.856	Quant <sub>Grav<sup>morp/roun</sup></sub> Min: 0.380, max: 0.943 Quant <sub>Grav<sup>morp/cycl</sup></sub> Min: 0.595, max: 0.830	
Depositional landforms —Sedimentology of gravel and hydrodynamics	Quantification Gravel situmetry Quant <sub>Grav<sup>situ/dire/shar</sup></sub> - Direction (360°) - Sharpness of maxima (in brackets) Flow direction of river	Quant <sub>Grav<sup>situ/dire/shar</sup></sub> (for locality and orientation of clasts, see Figure 13c) Trends/mean Max 1: 259° (35) <u>Flow direction: 245°</u> Max 2: 244° (21) Max 3: 223° (15)	Quant <sub>Grav<sup>situ/dire/shar</sup></sub> (for locality and orientation of clasts, see Figure 13c) Trends/mean Max 1: 198° (63) <u>Flow direction: 231°</u> Max 2: 249° (33) Max 1: 330° (49) <u>Flow direction: 280°</u> Max 2: 285° (28)	
			Quant <sub>Grav<sup>situ/dire/shar</sup></sub> (for locality and orientation of clasts, see Figure 13c) Trends/mean Max 1: 319° (53) Flow direction: 285° Max 2: 281° (37)	

The grey compartment denotes the basic data of the study area and the tripartite colored subdivision marks the subdivision into erosional and depositional land-forming indices.

Table 1a is an introduction into the key topic of the current study, providing an overview of the terminology, definitions, and applications of these landscape-forming indices while Table 1b is a presentation of the numerical range of the 14 landscape-forming

indices in relation to the landforms and landform series under consideration. Moreover, the reader is made familiar with the topographic and lithological basics of the study area.

## 2. Geological and Geomorphological Setting

### 2.1. Overview of the Foreland–Basement Region

The area under study along a deep-seated lineamentary fault zone, called the Franconian Lineamentary Fault Zone (FLFZ), offers outcrops from unmetamorphosed sediments in the foreland through all stages of regional metamorphism (very low-grade to high-grade metamorphic rocks). Apart from that, metamorphic felsic mobilisates/pegmatoids rife with feldspar and quartz as well as tectonized talc schist and stratabound Cu-Zn deposits occur [25]. This catena exists within a range of 30 km spanning the interval from the Neogene to the Quaternary [23] (Figures 1 and 2). Figure 1 provides an overview of the geological setting from the Mesozoic Foreland to the high-grade regionally metamorphosed rocks of the Münchberg Gneiss Complex both of which are separated from each other by the deep-seated lineamentary fault zone of the “Fränkische Linie”. A close-up view of the lithology exposed in this foreland–basement transition zone is displayed together with sampling sites in Figure 2.

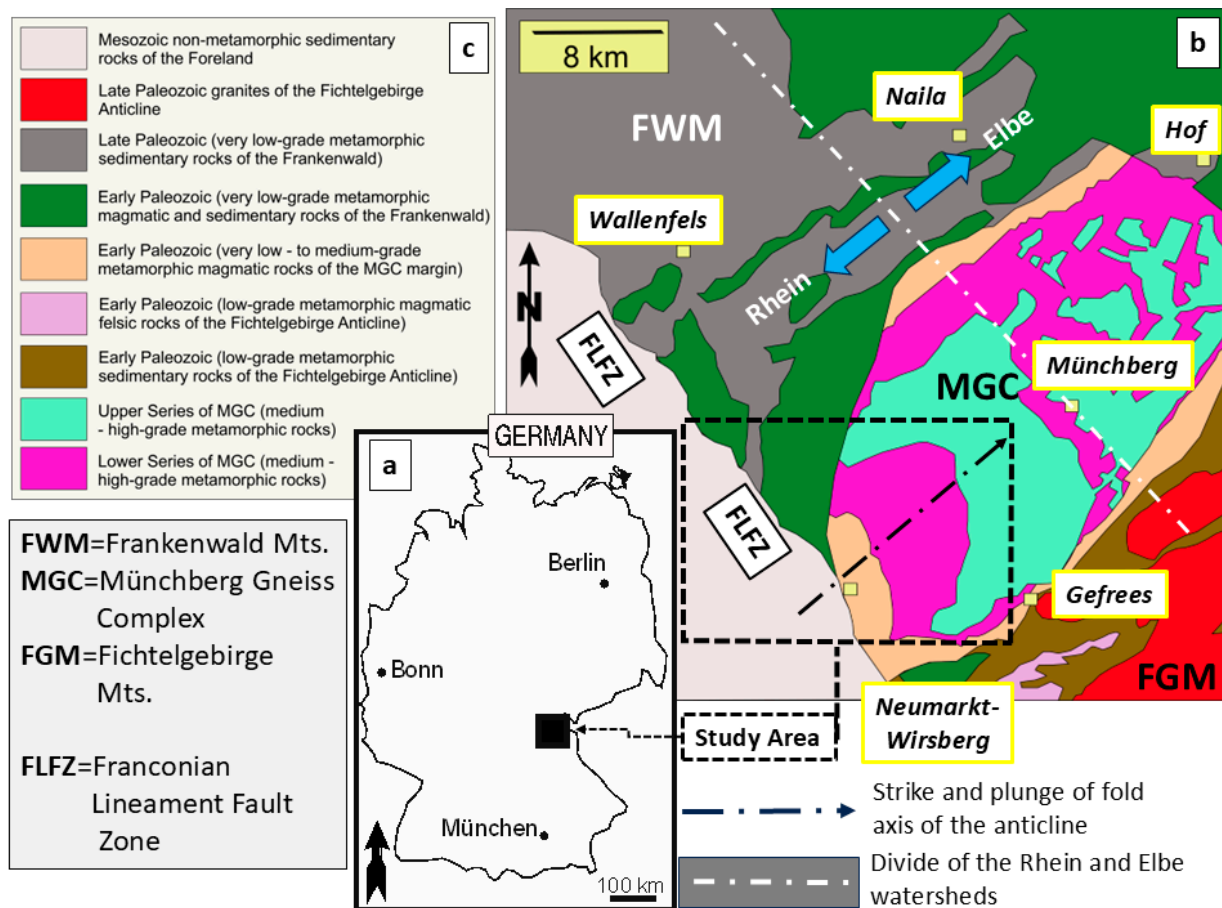


**Figure 1.** Geodynamic overview of the NE Bavarian basement and the study area at the western edge of the Münchberg Gneiss Complex, SE Germany. (a) The position of the study area in Germany. (b) The geological setting of the study area in SE Germany and its neighboring geodynamic units of the Frankenwald and Fichtelgebirge Mts. (modified from Emmert et al. [26]). (c) Legend for the map in Figure 1b. The area with the dashed line denotes the close-up view of the geological setting in Figure 2.

The current study addresses a novelty harnessing the various “roughness indices” from the large-scale “bedform roughness of drainage channels” to the small-/regional-scale “washboard landscapes” (Figure 3a, Table 1). The so-called “washboard landscapes” are represented by the South German Scarpland and have been studied by different geoscientists [27–34]. They are a series of homoclinal strata made of limestones, sandstone, and claystones moderately dipping towards the basement while turning stepwise into a series of hogbacks as they are approaching the deep-seated lineamentary fault zone of the “Fränkische Linie”. Lithologically, the different vulnerabilities to weathering and erosion, and hydrographically, the strike streams, are the main reasons for this typical landscape to come into existence in the basement–foreland border zone.

## 2.2. Lithology and Geology of the Münchberg Gneiss Complex

The Münchberg Gneiss Complex (MGC) makes up the North Bavarian Basement together with another two geodynamic complexes, the Frankenwald Mts. (FWM) found towards the NW and the Fichtelgebirge Mts. (FGM) along its SE boundary (Figure 1). All three geodynamic complexes pertain to the Central European Variscides. The FWM consists of a succession of Paleozoic sedimentary and magmatic rocks undergoing very low-grade regional metamorphism, whereas the FGM forms a series of Carboniferous–Permian felsic intrusive rocks surrounded by Early Paleozoic sedimentary and magmatic wall rocks which were subjected to low-grade regional metamorphism [26,35,36]. Onto these autochthonous Paleozoic rocks, the low-grade to high-grade metamorphic rocks of the MGC nappe were overthrust from the SE together with its Early Paleozoic very low- to medium-grade wall rocks [37–40] (Figure 1). The MGC forms a NE plunging anticline that offers in its SW part a full-blown catena of bedrocks at the outcrop, from high-grade metamorphic basement rocks to non-metamorphosed siliciclastic sediments, all of which are sculpted by mass wasting and fluvial land-forming processes and hence allow for a direct compositional–geomorphological correlation (Figures 1 and 2, Table 1).

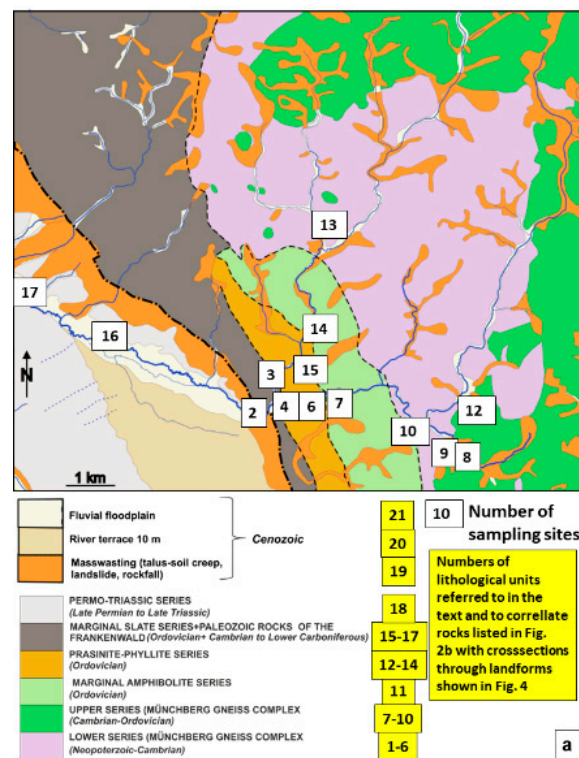
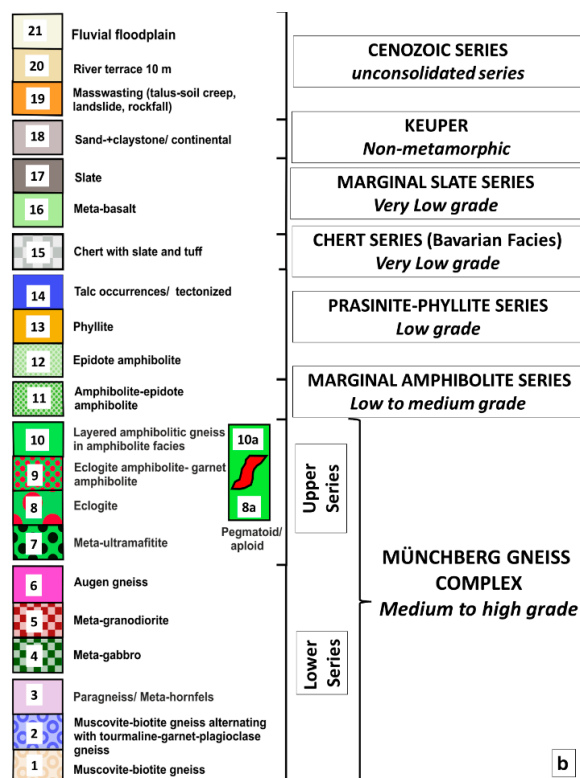


Figure 2. Cont.



**Figure 2.** Geological overview and the bedrock lithologies of the landform series under consideration. (a) The geological map of the study area with the Cenozoic overburden and the fluvial drainage network and sampling sites. The geological basis is the geological maps published by Emmert and Weinelt [36], Emmert et al. [35], Stettner [39] and Stettner [40] which, in places, have been updated during the current investigation. (b) Lithological units shown in Figure 2a and symbols used in the cross-sections through the landforms (see Figure 4).

*The Lower- and the Upper Series of the MGC:* The allochthonous synform is subjected to a dual subdivision into the Lower Series and the Upper Series (Figure 2a,b—1 to 10). The Lower Series is Neoproterozoic to Cambrian in age and composed of meta-pelites and meta-greywackes, intercalated with orthogneisses/augengneisses and lenses of metagabbro and metagranodiorites. The orthogneiss yielded a Rb/Sr whole rock age of  $499 \pm 20$  Ma [41]. U/Pb age dating using zircon and monazite from metagabbros and metagranites gave an age of intrusion around 500 Ma for both intrusive rocks [42]. In the Upper Series, basic metamorphic rocks prevail. The eclogites are of MORB affinity and the original basalts were vented at 525 Ma [42] (Figure 2a,b—7 to 10). The basic volcanic rocks underwent a pressure regime of 13 kb. The meta-basic rocks of the Cambrian to Ordovician Upper Series also gave host to the albite-bearing pegmatoids and aploids (Figure 2b—8a to 10a).

*The tripartite wall rock series of the MGC:* These wall rocks consist of the Marginal Amphibolite Series (Figure 2a,b—11) and the Phyllite-Prasinite Series (Figure 2a,b—12 to 14) alternating with metapelites. Along NW-SE fault zones, tectonized talc schists can be found. The Marginal Slate Series, rife with metabasalts alternating with slates, is similar in age to the aforementioned lithological units but of lower metamorphic grade (Figure 2a,b—16 to 17). The very low-grade Chert Series is located outside the Marginal Slate Series and forms part of the Bavarian Facies (Figure 2b—15). It is studied geomorphologically for comparison with the hornfels lithologies within the MGC (Figure 2b—3).

*The foreland sediments:* The N Bavarian Basement is a tilted basement block uplifted along a deep-seated lineamentary fault zone, called the “Franconian Line” (FLFZ), that at its SW edge is displaced by as much as 1000 m of cumulative movement against the Mesozoic and Cenozoic sediments in the study area (Figure 1). During the Late Triassic Keuper, a playa-like

environment grading into a terminal alluvial plain came into existence covering some patches of Permian age [27,43] (Figure 2b—18). Fluvial and mass wasting deposits are found all across the study area, whereas the mixed-type fluvial–mass wasting deposits are confined to the River Schorgast’s outburst into the foreland along the FLFZ where they form a large terrace at about 10 m above the modern talweg (Figure 2a,b—19 to 21).

2.3. Landforms and Landform Series of the Münchberg Gneiss Complex

It was not until the Late Paleogene when continental sediments evolved again on the dryland and paleosurfaces which truncated the uplifted Variscan basement and the Mesozoic sediments of the foreland alike [44,45]. Thauer [44] used the erosional landforms which he called wide valleys and V-shaped valley incised into the first mentioned ones for his age classification of the landscape. Studies centered around the Quaternary and Pre-Quaternary geomorphological evolution of the Central European Variscides, in general, and the N Bavarian basement, in particular, are scarce and were mostly eclipsed by geological and petrological studies which need to be addressed in the current study for compositional reasons when discussing the geomorphology of the MGC [46–53]. The MGC is not only an erratic allochthonous geodynamic unit—see Section 3.1—but also erratic in terms of its topography, forming a wide morphological depression between the FGM and the FWN (Figure 1). It forms the northeastern-most part of a washboard landscape covered by two presumed paleosurfaces as they were dealt with by different authors [52,54,55] (Figure 3a). Number I is gently dipping off the FLFZ as a planar architectural element covering the Franconian Scarpland while number II is a curved presumed surface consisting of three discrete plains: 1. a (sub) horizontal paleoplain, 2. a moderately steeply dipping step-fault plain, and 3. steeply dipping foreland plains (Figure 3a–c).

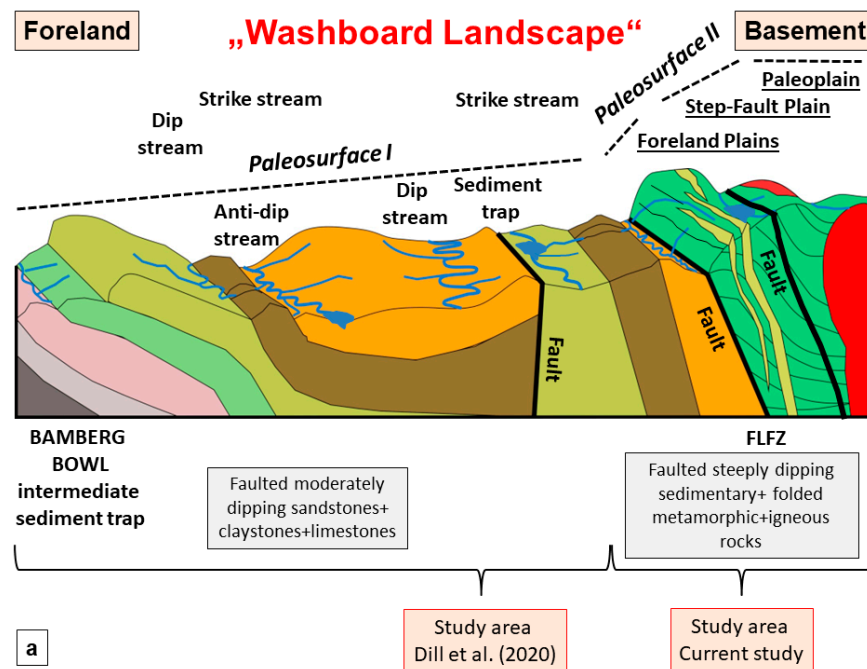


Figure 3. Cont.

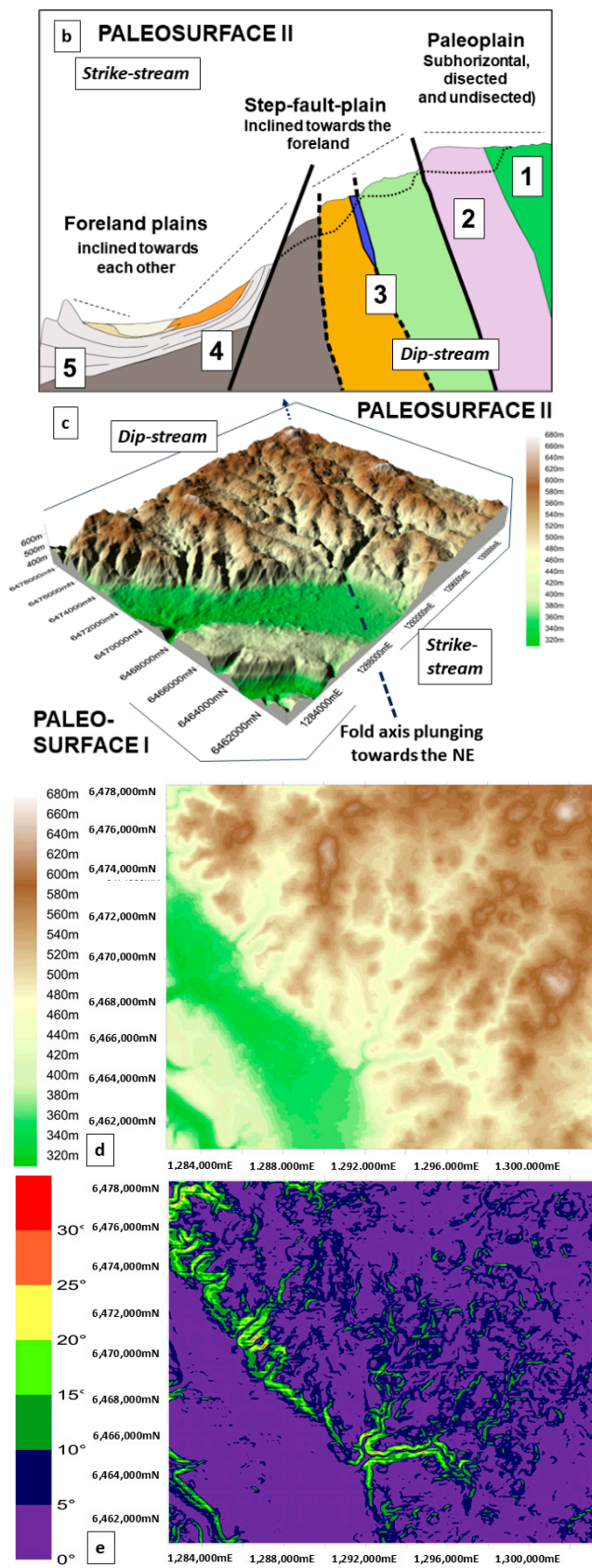
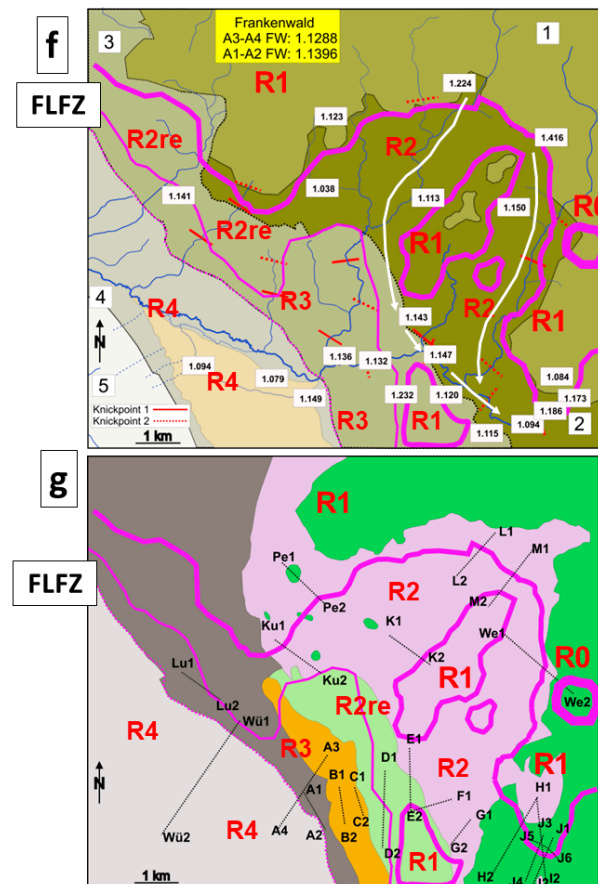


Figure 3. Cont.



**Figure 3.** Geomorphological overview of the washboard landscape and the study areas defined by the two paleosurfaces, I and II. (a) Cartoon showing two paleosurfaces. Paleosurface I is gently dipping off the FLFZ (Franconian Line Fault Zone) as a presumed architectural planar element covering the Franconian Scarpland. Paleosurface II is a presumed surface covering the basement and the immediate foreland affected by the FLFZ. It is a tripartite curved surface covering three plains [29] (b) Cartoon providing an idealized cross-section of the tripartite paleosurface II. For geology, see key of Figure 2a. Dotted line marks the modern-day surface and longitudinal profile of the talweg with its knickpoints. (c) Digital terrain model of the study area showing the controlling linear tectonic elements of the main anticline of the MGC. (d) Topographic map showing the altitude of the study area in meters a.m.s.l. (e) Thematic map showing the slope angle values of the various land forms under consideration in degrees. (f) Geomorphological index map showing the morphotectonic units currently on display: 1 = paleoplain undissected, 2 = paleoplain dissected, 3 = step-fault plain inclined, 4 = foreland plain inclined off the basement, and 5 = foreland plain towards the basement (Figure 3b). The position of the reference cross-sections (Figure 4) and the maximum aerial extension of relief generations R1 to R4 (Rre = R2 landforms are patchily preserved as relics on R3) determined based upon the vertical sinuosity—valley (VeSi<sub>val</sub>) index are displayed by red full, stippled, and dashed-stippled lines. (g) Geological index map (for legend, see Figure 2a). The position of the reference cross-sections (Figure 3g) and the maximum aerial extension of relief generations R1 to R4 (Rre = R2 landforms are patchily preserved as relics on R3) determined based upon the vertical sinuosity—valley (VeSi<sub>val</sub>) index are displayed by red full, stippled, and dashed-stippled line.

### 3. Methodology

#### 3.1. Mineralogy and Petrology

Mineralogy and petrology are the major disciplines for obtaining insight into the parent and wall rocks of the positive and negative landforms, respectively. The sampling sites for the compositional analysis are given in Figure 2 and the indices which these miner-

alogical methods use are shown in Table 1, e.g., QuantClaSil, QuantSan<sub>/ligh</sub>, QuantSan<sub>heav</sub>, QuantGrav<sub>lith</sub>, etc.

*Petrographic microscopy:* Routine thin section analysis was performed together the optical microscopy of heavy and light minerals counting between 200 and 300 grains counted per sample. The HM separation was conducted for each sample to the grain size fractions richest in HMs (the 63 to 360  $\mu\text{m}$  fraction) using sodium polytungstate of a density of 2.9  $\text{g}/\text{cm}^3$ .

*Raman spectroscopy:* The Raman spectra were acquired by using the Horiba Jobin-Yvon RPA-HE 532 Raman Spectrograph (Kyoto, Japan) with a multichannel air-cooled CCD detector ( $-70\text{ }^\circ\text{C}$ ) and NdYag laser at 532 nm with a nominal power of 100 mW. The spectral range was between 210 and 3400  $\text{cm}^{-1}$  with a spectral resolution of 3  $\text{cm}^{-1}$ . The Raman system includes a “Superhead” fiber optic Raman probe for non-contact measurements, with a 50 $\times$  LWD Olympus visible objective. The spectra were acquired using an exposure time of 1–5 s, 10–20 acquisitions, and a laser power less than 60%, in order to improve the signal-to-noise ratio and to avoid any possible damage of the samples caused by the laser radiation. The interpretation of the micro-Raman spectra was conducted using the LabSpec software version 5.25.15 by means of baseline correction and peak-fitting. It is the most advanced level and used for the fine-tuning of the mineralogical results.

*X-ray analysis:* X-ray diffraction (XRD) patterns are a supplement to the aforementioned method and were recorded using a Philips X’Pert PW3710  $\Theta$ – $2\Theta$  diffractometer (Cu-K $\alpha$  radiation generated at 40 kV and 40 mA—Almelo, The Netherlands), equipped with a 1 $^\circ$  divergence slit, a secondary monochromator, a point detector and a sample changer (sample diameter 28 mm). The samples were investigated from 2 $^\circ$  to 80 $^\circ$   $2\Theta$  with a step size of 0.02 $^\circ$   $2\Theta$  and a measuring time of 3 sec per step. For specimen preparation, the top loading technique was used.

### 3.2. Geochemistry

Major and trace elements were analyzed by X-ray fluorescence spectrometry (XRF). Powdered samples were analyzed using a PANalytical Axios and a PW2400 spectrometer (Almelo, The Netherlands). Samples are prepared by mixing with a flux material and melting into glass beads. The beads are analyzed by wavelength dispersive X-ray fluorescence spectrometry (WD-XRF). To determine loss on ignition (LOI), 1000 mg of sample material is heated to 1030  $^\circ\text{C}$  for 10 min. After mixing the residue with 5.0 g lithium metaborate and 25 mg lithium bromide, it is fused at 1200  $^\circ\text{C}$  for 20 min. The calibrations are validated by an analysis of reference materials. “Monitor” samples and 130 certified reference materials (CRM) are used for the correction procedures.

### 3.3. Terrain Analysis *Sensu Stricto*

The centerpiece of the current study pursues a strategy of the “golden harmony” between a pure landform description and a pure collection of numerical data, creating thematic maps showing the altitude and the slope angle in degrees. Based upon the satellite images, a fine-tuning of the slope angle and the inclination of the talweg was calculated. The latter datasets form the basis for the cross-sectional and longitudinal profiles discussed in the current study in combination with the compositional studies (Sections 3.1 and 3.2).

*Sinuosity determination:* Sinuosity measurements are applied to the indices  $\text{VeSi}_{\text{val}}$ ,  $\text{VeSi}_{\text{lith}}$ , and  $\text{HoSi}_{\text{lith/grad}}$  (Table 1). The river (horizontal) sinuosity was obtained using ArcGIS software 10.2.2. The rivers were digitized as polylines and sinuosity value was calculated using Sinuosity toolbox that measures the deviation of a line from the shortest path by the following formula: total length/shortest distance. A straight line will show a sinuosity index of 1. In this study, the reciprocal values of this index were used. Vertical

sinuosity was measured with the same toolbox in ArcGIS applied on a digitized polyline of the elevation line of the topographic profile. All of the topographic profiles were normalized at the same  $x$  and  $y$ -axis. Sinuosity index was measured for the entire profile as well as for various sections.

*Slopes and slope angle:* Slope angle measurements are used for the indices  $VaSIAn_{alti}$  and  $VaSIAn_{norm}$  (Table 1). Cross-sectional topographic profiles were created using Google Earth Pro software—version 7.3.6.10201. The sections of interest were drawn as a path line and the profiles were obtained using the “Elevation profile” option. The software shows the overall maximum and mean slope of the profile, as well as the slope values for smaller sections within the profile based on the specific selection.

*Inclination of drainage systems:* Longitudinal topographic profiles along the river valleys were obtained by calculating the inclination of the talweg ( $IncTal_{lith/grad} + knickpoints$ ) (Table 1). This is performed by extracting the maximum and minimum altitudes (“rise”) and the length of the profile (“run”)—slope = rise/run. This procedure was applied on the entire profile and on specific sectors within the profile.

*Quantification of mass wasting and fluvial deposits:* Adobe Photoshop software was used to obtain the index  $Quant_{flu/mas}$  by setting a measurement scale and quantifying the pixels of different types of deposits.

### 3.4. Composite Hydraulic–Petrographic Measurements

The granulometry, morphometry, and sitometry of the gravel size class, with emphasis placed on the cobbles, small boulders, and coarse pebbles [56], is abbreviated to the GMS method, which uses a combination of field and laboratory work to calculate the  $QuantGrav_{gran/sort/mod}$ ,  $QuantGrav_{morp/roun/cycl}$ , and the  $QuantGrav_{situ/dire/shar}$  (Table 1). During fieldwork, a horizontal or vertical reference square measuring  $1 \times 1$  m was outlined on the exposed clastic sediments. Between 50 and 150 measurements were performed. This is the only way to measure the clast orientation in the field using the strike or dip of the longest axis of the gravel-sized fragments at outcrop.

## 4. Results

### 4.1. The Mineralogical Composition of the Bedrocks and the “Landscape-Forming Indices” (LFIs)

To shed some light on the origin of the landscape and its landforms, three compositional groups, very much different from each other regarding their mode of formation, need to be investigated. The autochthonous one is synonymous with the bedrock of the landforms and the allochthonous one resulted from the deposition of mass wasting and fluvial processes. The (semi- to un-) consolidated (par) autochthonous material takes an intermediate position and has been immediately derived from the natural weathering of the bedrock (Table 1). The latter sediments are dealt with together with the allochthonous debris [57–65].

#### 4.1.1. Autochthonous Mineralogical–Petrographic and Roughness Indices of Landform Series in Cross-Sectional Profiles

*Mineralogy and petrography of bedrocks:* In Table 2, the bedrock lithologies are correlated with the pertinent landform types found on the three different reference plains. Considering those landforms on a higher hierarchical level create landform series of a characteristic landscape as demonstrated by different geomorphologists [60,66–69]. The platforms for these landforms and landform series are provided by topographic and thematic maps showing the slope angle (Figure 3d,e). A series of reference cross-sections form the link between the compositional and numerical geomorphology (Figure 3f,g and Figure 4).

**Table 2.** Lithological categories, rocks, minerals, and landforms underlain by these bedrock lithologies vs. landscape-forming indices (LFIs).

Lithological Categories	Rocks	Figure 2b	Minerals	Figure 3b,f,g	Landforms Underlain by the Bedrock Lithologies	Landscape-Forming Index			
						VaSiAn <sub>norm</sub>	VeSi <sub>lith</sub>	QuantSed <sub>morp/roun</sub>	QuantSed <sub>morp/cycl</sub>
(Meta) psammo-pelites	Muscovite-biotite gneiss	1	K feldspar, quartz, muscovite, biotite, chlorite, plagioclase, garnet, zoisite, epidote, apatite, zircon, ore minerals	1, 2	Monadnock summit Erosional fluvial terrace Large and shallow valley (relics) Bosselated paleoplain V-shaped valley wide angle V-shaped valley acute angle with telescoping Ridge-resistant hill Hillock Hump Truncated canyon–gully	Max 6.970 Mean 2.868	Max 663 Mean 266	Max 0.971 Mean 0.655	Max 0.0873 Mean 0.753
(Meta) psammo-pelites	Muscovite-biotite gneiss alternating with tourmaline-garnet-plagioclase gneiss (composite lithology)	2	Quartz, plagioclase, K feldspar, muscovite, biotite, garnet, chlorite, tourmaline, zoisite, apatite, zircon, rutile, ore minerals	1, 2	Monadnock-summit Large and shallow valleys Bosselated paleoplain V-shaped valley wide angle V-shaped valley acute angle V-shaped (wide angle) with telescoping Hump	Max 2.983 Mean 2.237	Max 271 Mean 184		
(Meta) psammo-pelites	Paragneiss—meta-hornfels	3	Quartz, biotite, muscovite, K feldspar, garnet, sillimanite, plagioclase, zoisite	1, 2	Large and shallow valleys Bosselated paleoplain V-shaped valley (wide angle) Ridges, resistant hill, ledges protruding from the mid-slope	Max 6.094 Mean 2.470	Max 1197 Mean 402	Max 0.867 Mean 0.698	Max 0.833 Mean 0.765
(Meta) psammo-pelites	Phyllite	13	Chlorite-sericite-quartz intergrowth, muscovite, albite, Ti magnetite, magnetite, tourmaline, zircon, apatite	3	Erosional fluvial terrace V-shaped valleys V-shaped valley with telescoping Flat uplands Ridges and ledges protruding from the top-slope Gently sloping plateau crest shoulder escarpment Escarpment face	Max 4.986 Mean 2.488	Max 479 Mean 177	Max 0.966 Mean 0.631	Max 0.876 Mean 0.761
(Meta) psammo-pelites	Slate	17	Muscovite-sericite, chlorite, quartz, albite, heavy minerals	3	Floodplain + fluvial erosional terrace V-shaped valleys Gently sloping plateau crest shoulder escarpment Fluvial staircase terraces/slip bank Escarpment face dissected/cut bank	Max 3.381 Mean 1.818	Max 197 Mean 159	Max 0.910 Mean 0.772	Max 0.865 Mean 0.811

Table 2. Cont.

Lithological Categories	Rocks	Figure 2b	Minerals	Figure 3b,f,g	Landforms Underlain by the Bedrock Lithologies	Landscape-Forming Index			
						VaSIAn <sub>norm</sub>	VeSi <sub>lith</sub>	QuantSed <sub>morp/roun</sub>	QuantSed <sub>morp/cycl</sub>
(Meta) psammo-pelites	Chert alternating with thin interbeds of slates and tuffaceous layers	15	Quartz, sericite, albite, chlorite	3	Mountain summit Fluvial erosional terrace Large and shallow valley Bosselated paleoplain V-shaped valley wide angle V-Shape valley acute angle	Max 3.628 Mean 2.422	Max 320 Mean 156		
(Meta) psammo-pelites	Sandstones with intercalated claystones	18	Quartz, K feldspar, muscovite, diff. heavy minerals	4, 5	Escarpment face Relic pediments Colluvial midslope/ top perched pediment (relic) Talus cone and alluvial fan Mixed-type fluvial-mass wasting hillwash plain High scarp footslope/ fluvial cutbank high scarp of strike stream drainage systems	Max 3.173 Mean 1.458	Max 582 Mean 216		
Metamorphic intrusive rocks	Augengneiss (meta-granite)	6	Quartz, K feldspar, plagioclase, muscovite, garnet, chlorite, zoisite, apatite, rutile, zircon, ore minerals	2	Large and shallow valleys V-shaped valley wide angle V-shaped valley acute angle V-shaped valley wide to acute with telescoping Ledges protruding from the mid-slope Resistant hill Ridge	Max 6.923 Mean 3.177	Max 855 Mean 446		
Metamorphic intrusive rocks	Meta-gabbro	4	Amphibole, plagioclase, quartz, biotite, titanite, garnet, rutile, zoisite, epidote, chlorite, ore minerals, pyroxene	2	Truncated canyon fill Bosselated paleoplain Hillocks	Max 3.765 Mean 2.181	Max 687 Mean 301		
Metamorphic intrusive rocks	Meta-granodiorite	5	Quartz, plagioclase, K feldspar, muscovite, biotite, garnet, apatite, rutile, zircon, ore minerals	2	Truncated canyon fill Bosselated paleoplain Hillocks	Max 3.765 Max 2.181	Max 687 Mean 301		
Metamorphic volcanic rocks/ tectonized	Talc schists	14	Talc, tremolite	3	Erosional terraces	2.375	421		
Metamorphic volcanic rocks	Meta-ultramafite	7	Olivine, bronzite-enstatite, tremolitic hornblende, zoisite, chlorite, vermiculite, serpentine (lizardite), magnetite, chromium mica	1, 2	Monadnock summit Erosional terraces with small Rills ( <i>silicate karst</i> ) Mud flows (debris flow) Talus and soil creep Solifluction lobes	Max 3.181 Mean 2.512	Max 989 Mean 778		

Table 2. Cont.

Lithological Categories	Rocks	Figure 2b	Minerals	Figure 3b,f,g	Landforms Underlain by the Bedrock Lithologies	Landscape-Forming Index			
						VaSIAn <sub>norm</sub>	VeSi <sub>liith</sub>	QuantSed <sub>morp/roun</sub>	QuantSed <sub>morp/cycl</sub>
Metamorphic volcanic rocks	Eclogite	8	Omphacite, garnet, zoisite, quartz, rutile, titanite, cyanite, amphibole, clinozoisite, zoisite	1	Monadnock summit boulder strewn (Blockmeer) Bosselated paleoplain Truncated V-shaped valley	Max 1.817 Mean 1.638	Max 1292 Mean 572		
Metamorphic volcanic rocks	Eclogite amphibolite-garnet amphibolite	9	Garnet, amphibole, plagioclase, zoisite, quartz, rutile, titanite, clinozoisite, zoisite, ore minerals	1, 2	Monadnock palisades boulder strewn (Blockmeer) Erosional terrace Large and shallow valleys Hillocks Resistant hills	Max 1.817 Mean 1.638	Max 1292 Mean 572		
Metamorphic volcanic rocks	Layered amphibolitic gneisses in eclogite and amphibolite facies	10	Amphibole, garnet, plagioclase, garnet, zoisite, clinozoisite, quartz, muscovite, chlorite, rutile, titanite, apatite, zircon, ore minerals	1, 2	Erosional fluvial terraces Large and shallow valleys Bosselated paleoplain V-shaped valley wide angle (embryonic) V-shaped valley acute angle with telescoping Hump Truncate canyon Hillocks	Max 2.777 Mean 1.937	Max 563 Mean 265	Max 0.958 Mean 0.707	Max 0.865 Mean 0.795
Metamorphic volcanic rocks	Amphibolite-epidote amphibolite	11	Amphibole, plagioclase, epidote, clinozoisite, chlorite, titanite, “leucoxene”, quartz, apatite, carbonate, ore minerals, garnet	3	Large and shallow valleys with regolith Bosselated paleoplain V-shaped valley (wide angle) V-shaped valley (acute angle) gorge Hogbacks Ridges	Max 4.649 Mean 2.787	Max 329 Mean 160		
Metamorphic volcanic rocks	Epidote amphibolite (“prasinite”, “meta diabase”)	12	Plagioclase, amphibole, chlorite, epidote, zoisite, titanite, ore minerals	3	V-shaped valleys V-shaped valley with telescoping Gently sloping Plateau crest shoulder escarpment	Max 5.460 Mean 3.138	Max 309 Mean 127		
Metamorphic volcanic rocks	Meta-basalt (“diabase”)	16	Plagioclase, pyroxene, chlorite, ore minerals, “leucoxene”, quartz, amphibole, epidote, apatite, calcite	3	Erosional fluvial terrace V-shaped valley Relic pediments Gently sloping plateau crest shoulder escarpment Resistant hill	Max 5.400 Mean 2.734	Max 685 Mean 248		
Metamorphic mobilisates	Pegmatoid-aploid	8a—10a	Quartz, albite, muscovite, zoisite	1, 2	Monadnock summit Large and shallow valleys Hillocks Flank deposits (never on top)				

Blank = not determined.

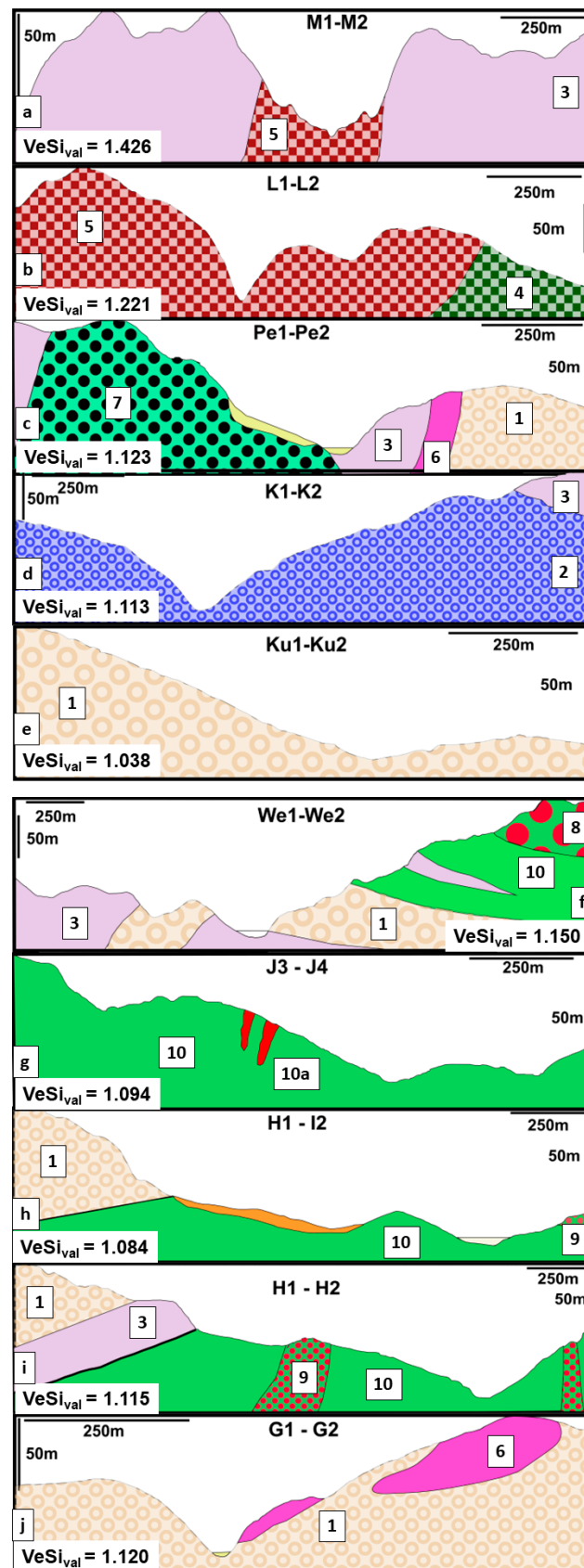


Figure 4. Cont.

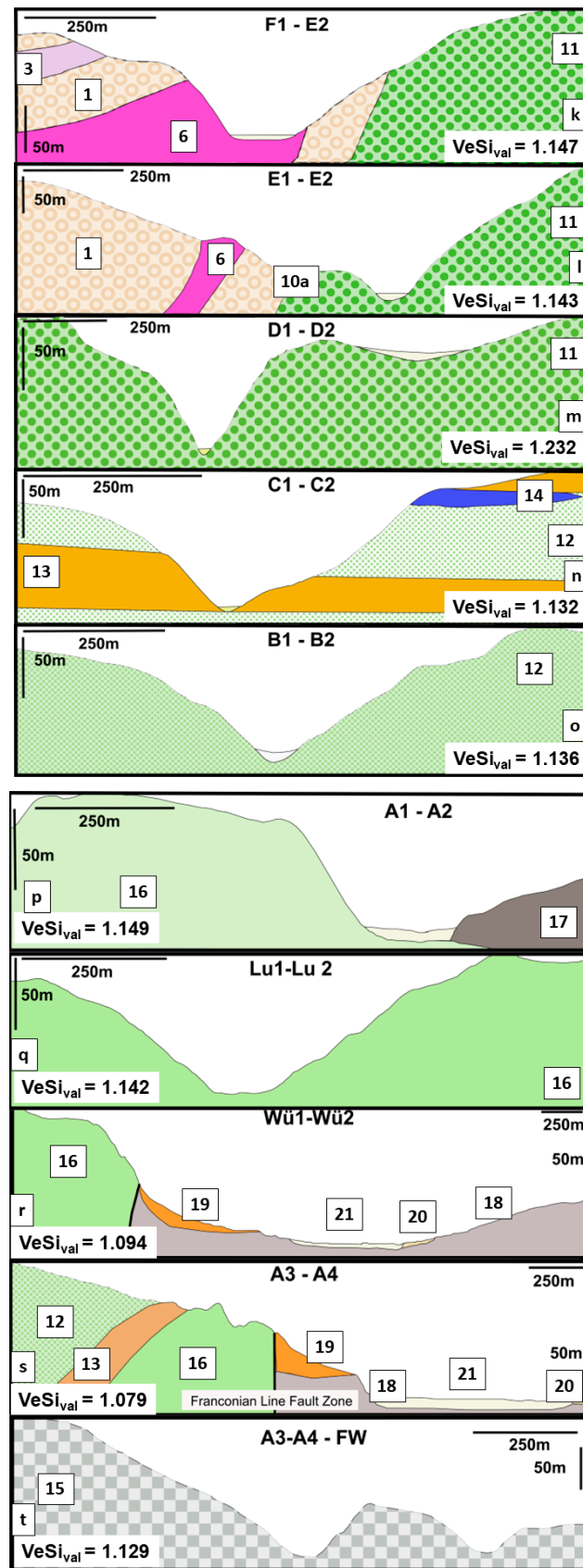
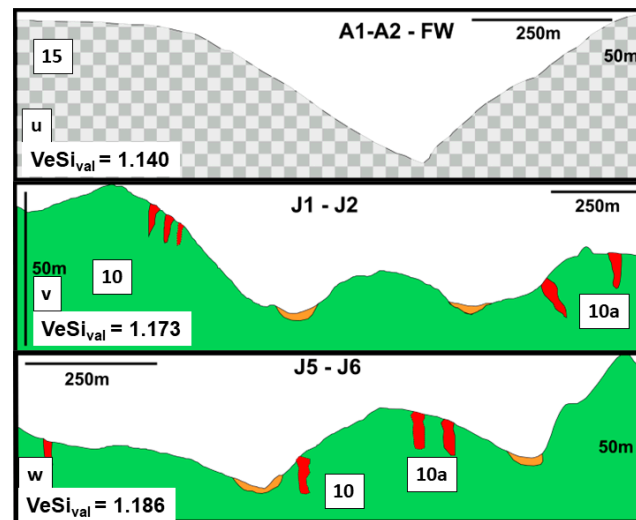


Figure 4. Cont.



**Figure 4.** The reference cross-sections provide the link between the landscape and the lithological composition. For lithology, see key of Figure 2b, and for their position, see Figure 3d. In the rectangles, the vertical sinuosity—valley ( $VeSi_{val}$ ) index of the landform series portrayed by the reference cross-section is given. It is the landscape roughness index of regional scale (for more information see text). (a) M1-M2, (b) L1-L2, (c) Pe1-Pe2, (d) K1-K2, (e) Ku1-Ku2, (f) We1-We, (g) J3-J4, (h) H1-I2, (i) H1-H2, (j) G1-G2, (k) F1-E2, (l) E1-E2, (m) D1-D2, (n) C1-C2, (o) B1-B2, (p) A1-A2, (q) Lu1-Lu2, (r) Wü1-Wü2, (s) A3-A4, (t) A3-A4 FW, (u) A1-A2 FW, (v) J1-J2, and (w) J5-J6.

The four bedrock lithologies ((meta)-psammopelites, metamorphic intrusive rocks, metamorphic volcanic rocks, and metamorphic mobilisates/pegmatoid) are categorized according to the BGS (British Geological Survey) recommendation and based upon the mineral assemblages arranged in order of decreasing amounts [70] (Table 2). The most varied mineral assemblages are encountered among the metamorphic volcanic rocks casting these bedrocks in the role of the primary provenance markers—see allochthonous lithology (Tables 1 and 2). They are equivalent to the Upper Series exposed in the morphotectonic units of the undissected paleoplain and volcanic lithologies in the inclined step-fault plain (Figures 2a,b and 3f). By contrast, a rather monotonous mineral association is observed among the pegmatoids which lack any potential as a provenance marker but which are of utmost importance for the applied geomorphology and economic geology part of the current study (Table 2) [17].

The meta-psammopelitic bedrocks are made of predominantly quartz, muscovite-sericite, K feldspar, and chlorite with some heavy minerals, and the metamorphic intrusive rocks with prevailing quartz and feldspar form the bedrock of landforms in the dissected paleoplain and to some extent in the Prasinite—Phyllite Series, the Marginal Slate Series, and the Chert Series (Figure 2a,b). Amphibole is the only mafic mineral to stand out among the silicates of the meta-basic igneous rocks. These landform series are numerically-compositionally subdivided and genetically interpreted based upon two regional LFIs, the vertical sinuosity—valley ( $VeSi_{val}$ ) index and the variation in slope angle altitude ( $VaSlAn_{alti}$ ) index of landform series.

*Vertical sinuosity—valley ( $VeSi_{val}$ ) index:* The  $VeSi_{val}$  index is a mirror image of the roughness of the landscape measured along a profile running perpendicularly to the main channel between the two highest elevations located at closest distance. It is a measure of the difference in height of all of the positive and negative erosional landforms that is unbiased by the height of outstanding elevations within the landform series under consideration.

The reference cross-sections of Figure 4 are used for the subdivision of the landscape. With the aid of the  $VeSi_{val}$  index, five relief generations sensu Bremer [71] have been singled

out (Figure 3f,g). The reference cross-sections of R1 are on display in Figure 4: Pe1-Pe2, We1-We2, J1-2, J-5-6 (Figure 4c,f,v,w), R2: L1-L2, M1-M2, J3-J4, K1-K2, H1-I2, Ku1-Ku2 (Figure 4a,b,d,e,g,h), R2re: H1-H2, G1-G2, F1-E2, E1-E2, D1-D2 (Figure 4i-m), R3: C1-C2, B1-B2, A1-A2, Lu1-Lu2 (Figure 4n-q), and R4: A3-A4, Wü1-Wü2 (Figure 4r,s). Relief generation 1 encompasses the oldest erosional landform series which are restricted to the horseshoe-like limbs of the NE plunging anticline made of lithologies of the Upper Series (Figure 3g). The cross-sections with the highest mountains in the study area have a moderate  $VeSi_{val}$  index of 1.150 and 1.123, attaining their maximum in section J5-6 in the SE of the study area in what might be called a rolling hill landscape paleoplain with only a few single monadnocks (Figure 4c,f). These relief generations do not show any zonation or any downstream trend within the drainage system. The  $VeSi_{val}$  index attains its maximum value (1.426) in the NE of the study area where the plunge of the fold axis reaches its deepest level and where a strongly rugged relief characterizes the landscape of relief generation 2 underlain by the Lower Series (Figure 4a,b). It passes through a rolling hill landscape (K1-K2,  $VeSi_{val}$  index: 1.113) into a rather flat paleoplain (J3-J4: 1.094, H1-I2: 1.084, Ku1-Ku2: 1.038). The index shows a downstream decreasing trend towards the edge of the paleoplain at H1-I2 (Figure 4h). Further downstream, another drainage system evolves with moderate values increasing from 1.115 continuously up to 1.232 encountered eventually in section D1-D2. It is accompanied by the build-up of a rolling hill landscape passing into a rugged one which is characterized by gorges incised into a pattern of multiple valley types telescoped into each other and denominated as R2re/relict (Figure 4m). The  $VeSi_{val}$  index is not only a tool for the numerical landscape classification from a rugged landscape (1.416–1.221), through a rolling hill landscape (1.186–1.113) into a flat landscape (1.094–1.038) but also cast as a measure for the detection of multiple-generation erosional processes marked by a downstream increasing trend (Figure 4i-m). The succeeding downstream increasing cycle of relief generation R3 has  $VeSi_{val}$  indices from 1.132 to 1.149 approaching the river's outlet where it debouches into the alluvial-fluvial plain of the foreland (Figure 4n-q). Relief generation R3 shows no remnants of ancient paleoplains and its valleys are surrounded by a hilly to rolling hill landscape which becomes the prevailing landscape of the step-and-fault plain near the FLFZ (Figure 3f,g). The landscape following downstream is no longer controlled by any trend related to the basement drainage system. The fluvial pattern converts from a dip stream into a strike stream drainage system that is exclusively governed by the movement along the FLFZ and its correlative landforms and sediments giving rise to a typical scarpland landscape on the foreland plains displaying  $VeSi_{val}$  indices between 1.094 and 1.079 (Figure 4r,s).

*Variation in Slope Angle altitude ( $VaSlAn_{alti}$ ) index:* The aforementioned regional-scale landscape index should always be run in combination with the  $VaSlAn_{alti}$  because the data are obtained from the same source. This enables us to conduct a numerical fine-tuning of landform series way beyond what is feasible with the  $VeSi_{val}$  during geomorphological mapping. The identification of individual landforms is based upon the mean slope angle values plotted versus the maximum altitude of the station point in a X-Y plots (Figure 5). The correlation coefficient R2 of the trend line of the data arrays is an independent support of the landform series classification whereas the data clusters are the landform or facies markers, proper (Figure 5). By means of Table 2 they can be supplemented with compositional data of the bedrock lithology. The classification scheme is an approximation to Hargitai and Kereszturi [72] but with emphasis placed on geometry and numerical parameters rather than genetical process issues which are dealt with in Section 5 Discussion in context with all remaining features: large and shallow valleys, bosselated paleoplain, wide angle V-shaped valley, acute angle V-shaped valley, uplift flats/plateau, gently sloping plateau and crest shoulders of escarpment, escarpment face, erosional terraces, high

scarp/cutbank-low scarp/slip bank, monadnock-summit, mixed-type hillwash plain, pediment, erosional terrace, set of staircase terraces, humps, hillocks, hogbacks, truncated canyon/gully, resistant hill, and palisade ridge. Most landforms are explained in regional overviews and textbooks or they are self-explanatory in terms of their outward appearance [60,66–69]. Only the term bosselated paleoplain needs some more detailed description because it is not well entrenched in geomorphology. It is an irregularly shaped surface with small hillocks, stumps, and depressions which neither match any of the common fluvial drainage patterns from trellis to dendritic nor can they be attributed to any stagnant waterbody known from the lacustrine or transitional wetland environments such as the Okavango Inland Delta.

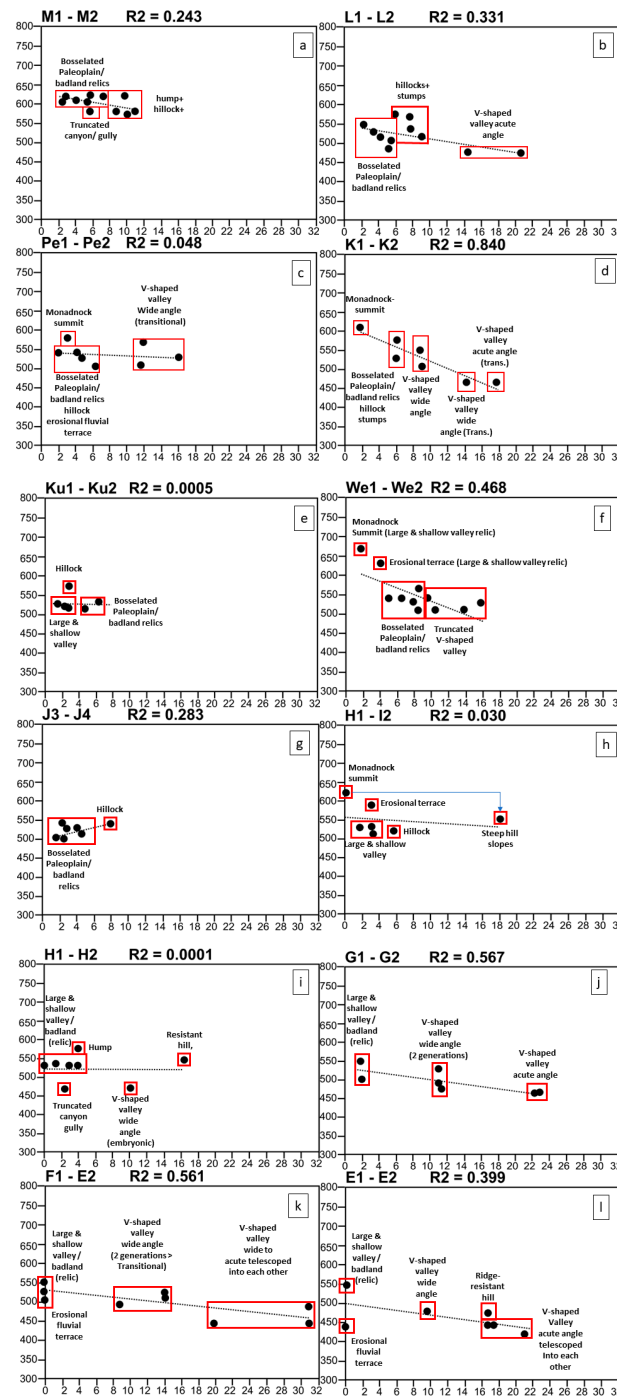
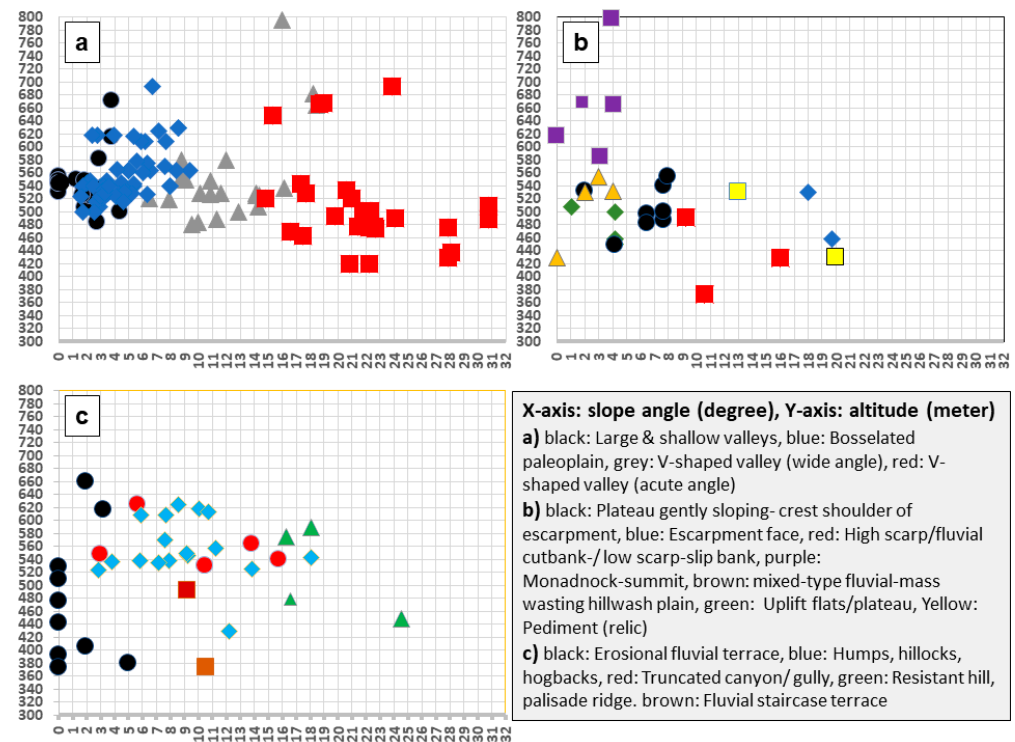


Figure 5. Cont.



and the lowest  $R^2$  value = 0.0001, at H1-H2, is attained (Figure 5g,I,v,w). It is the only area where pegmatoids occur in the study area, delineating a region of particular interest for the applied section of geomorphology and the turning of the  $VeSi_{val}$  indices (Figure 4g,v,w and Figure 5g,v,w). The same holds true when the foreland landform series are considered. Both basement and foreland parts of the profiles significantly differ from each other in term of inclination and provide bilateral symmetrical patterns with the parallel to the X-axis acting as a mirror axis (Figure 5r,s). Both trend lines intersect each other where the escarpment face meets the top part of the relic pediment.



**Figure 6.** Overview of the variation in slope angle altitude ( $VaSlAn_{alti}$ ) index as facies marker.

#### 4.1.2. Autochthonous Mineralogical Composition and Petrophysical Indices of Landform Series in Cross-Sectional Profiles

The two indices, vertical sinuosity—lithology of the landform ( $VeSi_{lith}$ ) and variation in the normalized slope angle of the landform ( $VaSlAn_{norm}$ ), are of local scale and have a focus placed on bedrocks and their landforms at outcrop (Table 2, Figures 7 and 8). To show the difference between the two, a cartoon provides an insight into the approach and its calculation method. It is a combined geomorphological approach taken to determine the rock strength and impact of the anisotropy of bedrocks on landforms mainly related to mass wasting processes. Measuring strength characteristics of geo-materials is a very complex endeavor running the gamut from material sciences dealing with artifacts to mineral sciences covering rocks and minerals while mainly using indentation techniques such as the measurement of the Vickers Hardnes Number (VHN) [73–77]. In geomorphology, there is only one method, used mainly for chrono-stratigraphy, which applies the rebound values of the Schmidt Hammer device and was originally designed for artificial products as well as siliceous calcareous raw materials for construction purposes [78–81]. This rebound method is a 1D measurement for on-site application only whereas the current method is a 2D measurement of the roughness along a slope profile accompanied by a second method measuring the variation in the slope angle ( $VaSlAn_{norm}$ ) (Figure 7). The first one ( $VeSi_{lith}$ ) provides the hardness or rock strength of the lithology exposed along the slope and the second  $VaSlAn_{norm}$  index is a mirror of the bedrock anisotropy expressed in the field by

ledges and benches which, when decreasing, shows up as boulder strewn areas littered with disintegrated bedrocks of random orientation. The ultimate states for the highest and the lowest values are known from tors and blockmeers, respectively. It has to be noted that in comparing both parameters, the maximum values should be taken. The difference between the maximum and mean value is a relative measure of the impact exerted by the supergene alteration on the lithological unit. It should not be confused with rock strength of single rock slap. For example, the paragneiss/metahornfels series is a rather homogeneous rock and forms, together with the eclogite, the top scorer in the list of rock strength, whereas the reference rocks forming the chert unit have only a moderate value because of the tiny tuffaceous interbeds (Figure 8c,f,p). It goes without saying that for the build-up of landform it is the rock strength of the rock unit (2D) that counts, not the hand specimen (1D). Tors made of mica gneisses are characterized by subhorizontal jointing and found on top of a hillock surrounded by elongated and platy boulders strewn across the slopes when undergoing creep and solifluction (Figure 8a,b). This conspicuous lithological anisotropy is the reason for the very high  $VaSlAn_{norm}$  values (Table 2). This also holds true for phyllites and slates, in which the anisotropy of the foliation and slaty cleavage is responsible for blocks and rock slaps of tightly folded phyllites covering the mid-slope of V-shaped valleys (Figure 8d,e). This is due to the rather high  $VaSlAn_{norm}$  values while featuring very low  $VeSi_{lith}$  values. Their maximum values and mean values do not differ significantly from each (phyllite 479 to 177, and slate 197 to 159) attesting to having been left almost unaffected by chemical weathering along with pervasive disintegration into rock slaps and flakey gravel scattered along the footslope of V-shaped valleys (Figure 8g,h). Metamorphic intrusive rocks such as augengneiss are almost identical to the paragneisses which they closely resemble regarding their mineralogical association (Figure 8i).

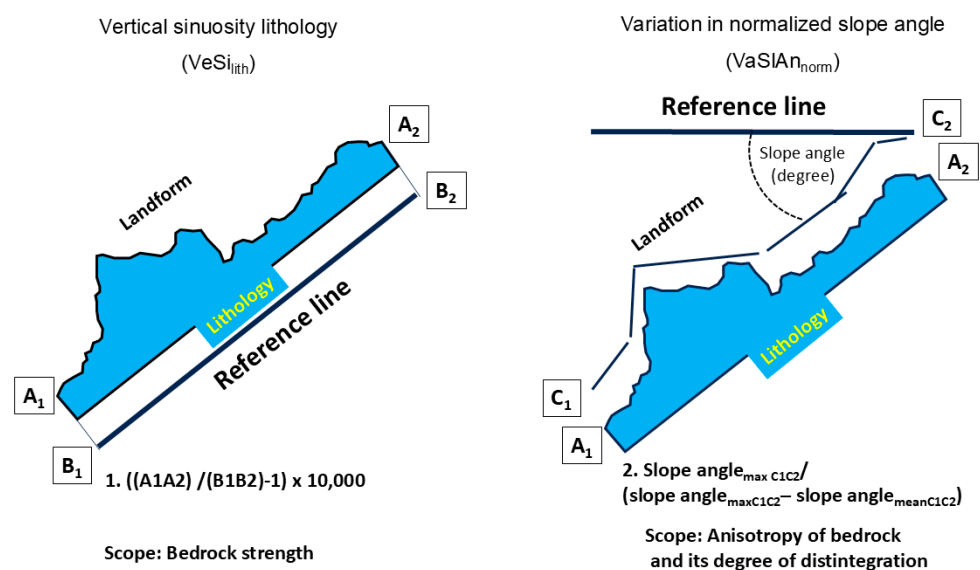


**Figure 7.** Overview of the petrophysical–geomorphological parameters vertical sinuosity–lithology ( $VeSi_{lith}$ ) of the landform and variation in normalized slope angle ( $VaSlAn_{norm}$ ) of the landform.

Their maximum and mean  $VeSi_{lith}$  values are higher than those of meta-argillaceous rocks, pointing to a greater rock strength, whereas the overall difference is more pronounced and accountable for a higher vulnerability to weathering. Meta-granites and granodiorites show a massive texture devoid of any strong foliation because they preserved the original texture of the parent material well (Figure 8j). The prograde metamorphic alteration from meta-basalt into foliated epidote amphibolite (prasinite) has no repercussions on the  $VaSlAn_{norm}$  values but the difference between their  $VaSlAn_{norm}$  and  $VeSi_{lith}$  values increases with increasing

regional metamorphism on account of higher resistance to weathering (Figure 8k,l, Table 2). Pyroxene and plagioclase in the metabasalts convert into epidote-clinozoisite s.s.s. and albite in the prasinite which both are less vulnerable to weathering. The transition from low-grade epidote to medium- to high-grade metamorphic amphibolite made predominantly of amphibole and plagioclase is not marked by any significant changes in  $VaSlAn_{norm}$  and  $VeSi_{lith}$  values (Figure 8m,o). The “jump” in passing from the metabasic rocks into meta-ultrabasic magmatic rocks is striking (Table 2). A monadnock of bronzite-serpentinite displays typical rillen features of “silica karst” being subrounded by angular boulders (Figure 8n). The chemical and mineralogical composition of metamorphic volcanic rock strongly influences the roughness parameters  $VaSlAn_{norm}$  and  $VeSi_{lith}$  of the landscape which they underlay.

#### 4.1.3. Autochthonous Mineralogical Composition and Petrophysical Indices of Landform Series in Longitudinal Sections of the Drainage System

*Inclination of the talweg—lithology plus gradient ( $IncTal_{lith/grad}$ ):* All drainage systems mapped in the study area display a wealth of characteristic features along the talweg regarding their inclination, in places, with stepwise changes in height named knickpoints. They are commonly interpreted from the petrophysical point of view but are also essential to the discussion of the evolution of the entire landscape [82,83]. They are most appropriately described by the inclination of the talweg ( $IncTal_{lith/grad}$ ). Some knickpoints, called knickpoint type 1, highlight concave riverbed sectors where a sudden change from a flat to a rather steep inclination of the talweg is encountered. The second type shows the reverse order of inclination data marked by a change from a steep to a conspicuously flat sector and named knickpoint type 2 (Figure 9a,c). The index is controlled by the wall rock and bedrock lithology exposed in the river banks and the river bed, respectively. The reference profile X15-X16 provides an insight into the Devonian and Silurian chert units which are composed predominantly of siliceous chemical sediments, metabasic tuffaceous volcanic rocks, and minor slates, black shales, and phosphorites. That accounts for the oscillating inclination of the talweg (Figure 9a,b). There also occurs an Ordovician arenaceous unit, and downstream an Early Carboniferous (Mississippian) slate unit. The images of Figure 9a,b give an overview of the landscape roughness index ( $IncTal_{lith/grad}$ ) at the largest scale possible of an individual landform of a river drainage system exposed in an acute-angle single-channel non-alluvial V-shaped valley cutting into the Devonian chert unit (slope angle  $30^\circ \Rightarrow 35^\circ$ , talweg angle  $2.7^\circ \Rightarrow 0.7^\circ$ ) with steps and pools, bars and cataracts typical of the onset of wandering channels [84]. On a yardstick of “roughness” landforms, the aforementioned outcrop is representative of the largest scale possible, whereas the  $VeSi_{val}$  index characterizes the “roughness” landform series of Figures 4t and 5t. This LFI lies at the opposite end of the scale while standing for the regional or small-scale representatives of landform indices. It has to be noted that a full-scale numerical–compositional environment analysis with longitudinal and cross-sectional profiles intersecting each other can be achieved based on capturing data from satellite images (Figures 4–6 and 9). The correlation coefficient  $R2$  of the  $IncTal_{lith/grad}$  index demarcates the paleogradient along which the inclination is assessed. It is comparable to the  $R2$  coefficients mentioned previously for the cross-sectional profiles and their indices ( $VaSlAn_{alti}$  and  $VeSi_{val}$ ). The highest  $R2$  coefficient  $IncTal_{lith/grad}$  index of  $R2 = 0.5113$  was obtained for the profile X1-X2, which is representative of a full-blown longitudinal section from relief generations R1 through R4 (Figures 3f,g and 5c,e). The lowest value was determined for profile X3-X4, which measures almost the same length as X1-X2 but is confined to relief generation R2 while touching by the river’s headwaters in relief generation R1. The landscape the river X3-X4 passes through is identical, with the subhorizontal dissected and undissected paleoplain (Figure 3b,f,g). The majority of the knickpoints of the study area are found in a triangle delineated by the aforementioned longitudinal section X1-X2 and X3-X4 with its vertex in the confluence of the two drainage systems.

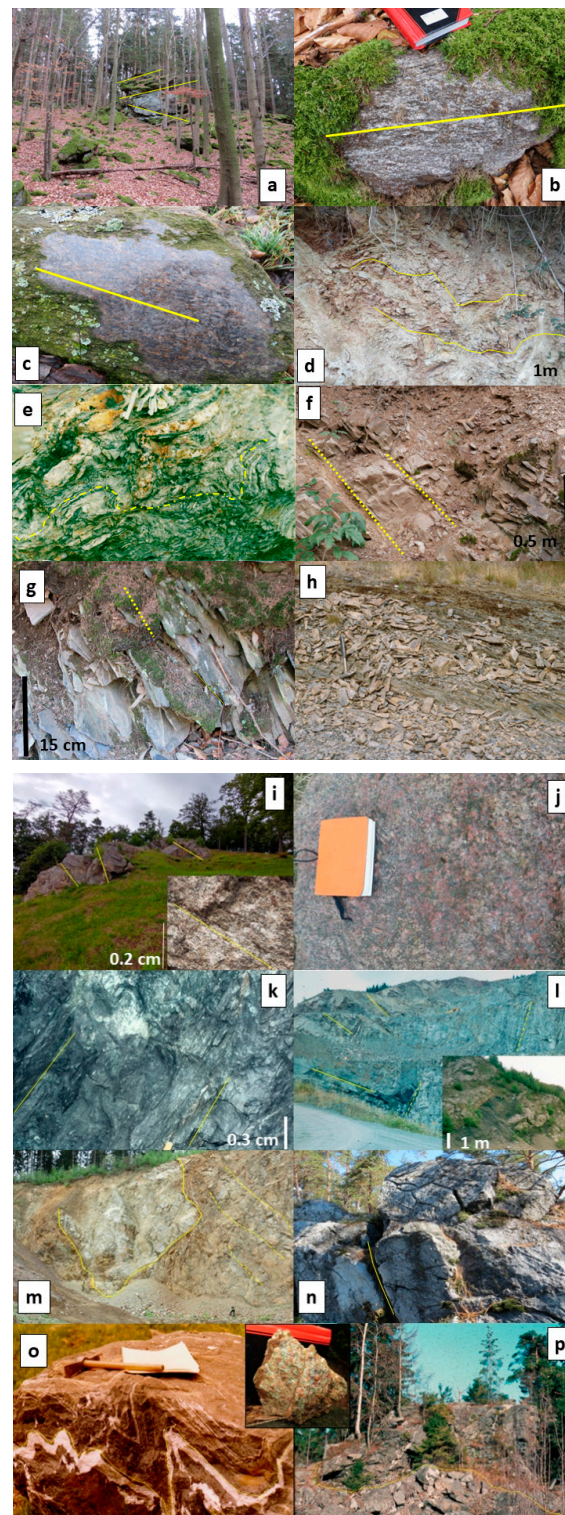


**Figure 8.** Meta-sedimentary, meta-intrusive, and meta-volcanic magmatic rocks and their landforms featuring different values of  $VaSlAn_{norm}$  and  $VeSi_{lith}$ . For numerical, compositional, topographic, and more detailed geomorphological data, see Table 2. (a) Mica gneiss with subhorizontal jointing on top of a hillock of a large and shallow valley. The top slope is strewn with boulders undergoing creep and solifluction. (b) Close-up view of one of the boulders which displays a lens-shaped and strong foliation. (c) A well-rounded paragneiss-hornfels boulder similar in outward appearance and internal texture but of rock strength twice as much as the mica gneiss. (d) Layered phyllite exposed on the mid-slope of a V-shaped valley. (e) Tightly foliated and folded phyllite as an allochthonous block. See ignition key for scale. Dashed line highlights wrinkled folding. (f) Alternating beds of chert, forming ledges and slates with the beginning of disintegration into debris of flakes at the footslope of a V-shaped valley. (g) Plates

of (roof)slate in the D horizon of the pedosphere. The argillaceous rocks are transformed into individual slaps of slate preserving the original siting of the rocks with the slaty cleavage. (h) Completely disintegrated pencil slates randomly scattered along the footslope of a V-shaped valley while forming a talus apron of flakey gravel. See hammer for scale. (i) Augengneiss ledges protruding out of the top slope of a V-shaped valley. The inset displays the tight arrangement of layers composed of quartz, K feldspar, and plagioclase with dark micaceous layers. (j) Meta-granite-to granodiorite showing a massive texture devoid of any strong foliation. (k) Steeply-dipping layers of tightly foliated epidote amphibolite (prasinite). (l) Layers of meta-basalt with narrowly-spaced joints near the escarpment of the inclined step-and-fault plain which is identical to the highland-boundary fault FLFZ (see Figure 3b,c). The inset shows the disintegration of the meta-basalt (diabase) as a consequence of weathering. (m) Amphibolite with a vaguely expressed layering which is intruded by an alkaline feldspar pegmatoid rimmed by a stippled line. It constitutes the edge of a V-shaped valley (wide angle) passing into a large and shallow valley. See geologists for scale. (n) Monadnock with subrounded exposures of bronzite-serpentinite displaying typical rillen features of “silica karst”. (o) Disharmonic tight folding of alkaline feldspar—quartz mobilisates in massive layered amphibolite gneiss. (p) A monadnock made of massive eclogite and eclogite amphibolite surrounded by a blockmeer of the same lithology. Inset shows a slightly weathered massive eclogite with red Fe-Al-Mn garnet and green omphacitic pyroxene.

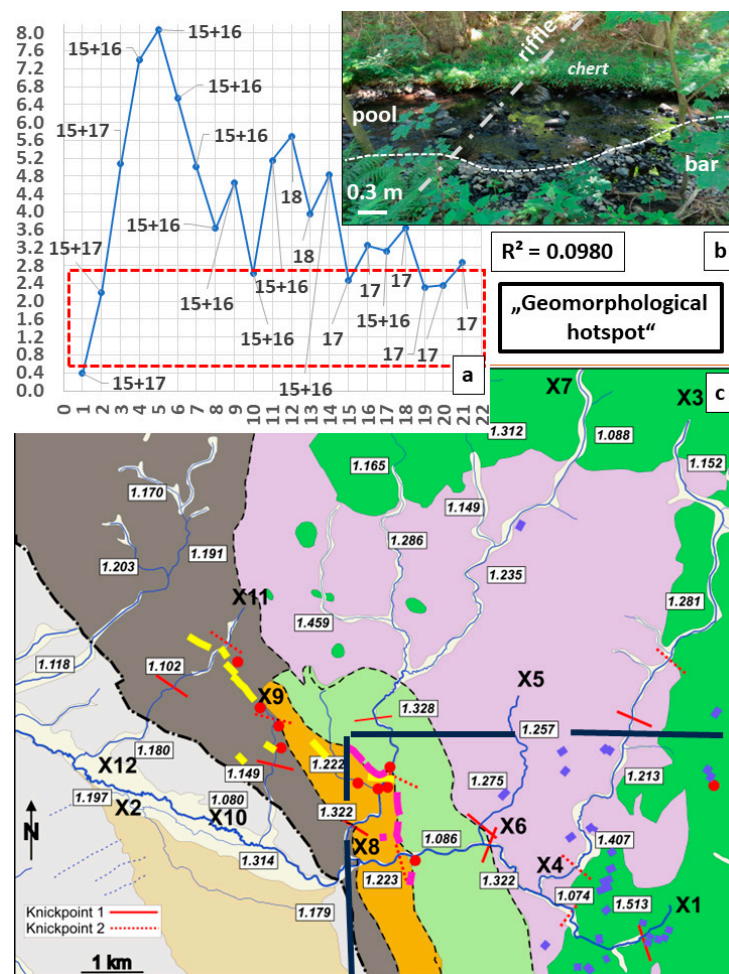
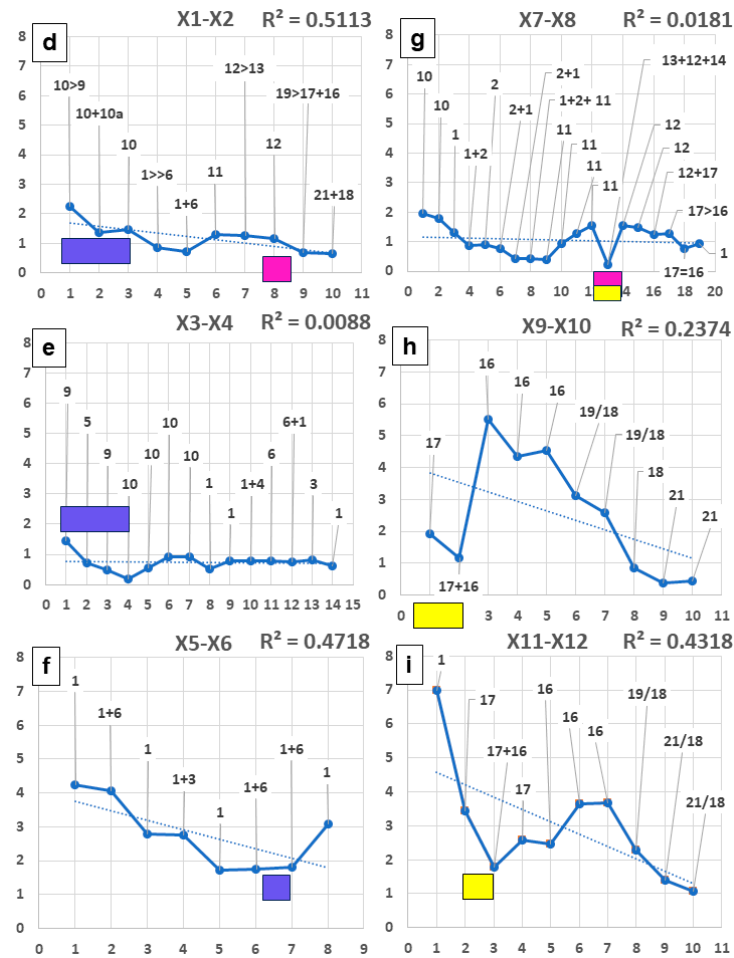


Figure 9. Cont.



**Figure 9.** Longitudinal sections along the talweg of drainage systems. The X-axis denotes the station points, and the Y-axis denotes the dip angle of the talweg in degree. The station points are characterized by Arabic numerals. The third variable is the wall rock or bedrock lithology of the host rocks exposed in the river banks and the river bed which, when different from each other on the left- and right-hand bank, are given by more than one numeral which refers to the notation in Figure 2b, e.g., profile X7-X9 13 + 12 + 14 = phyllite > epidote amphibolite > talc schist (for lithology, see Figure 2b). The correlation coefficient  $R^2$  between the two data sets is given in the upper right-hand corner of the diagram. (a) X–Y plot showing the inclination of the talweg ( $IncTal_{lith/grad}$  index) in degrees. Y-axis versus the station point downstream of longitudinal profile X15–X16 FW. The knickpoints intensity can be directly assessed by the length of the various intervals of the graph and the type of knickpoint (see text) by its upward and downward directions. At station point 11, the longitudinal section is intersected by the cross-section A3–A4 FW (Figure 5t). The red rectangle marks the  $IncTal_{lith/grad}$  index fluvial facies in the close-up view of Figure 9b. (b) Incision of an acute-angle single-channel non-alluvial V-shaped valley into the Devonian chert unit (slope angle  $30^\circ \Rightarrow 35^\circ$ , talweg angle  $2.7^\circ \Rightarrow 0.7^\circ$ ). See reference profile with steps and pools in (stippled white line = strike of bedding). (c) Geological index map (for more detail and key, see Figure 2a) with horizontal sinuosity—lithology plus gradient index ( $HoSi_{lith/grad}$ ) given in the white boxes; the knickpoint types 1 and 2 and the start and end points of longitudinal sections are displayed in Figure 9d–i by X–Y diagrams plotting the station points and inclinations data. The red dots mark mines of talc—(purple), pegmatoid—(dark blue), and Cu-(Au) deposits (yellow). (d) X1–X2, (e) X2–X3, (f) X5–X6, (g) X7–X8, (h) X9–X10, and (i) X11–X12 (for color symbols, see Figure 9c).

The X–Y plots reflect an intimate relationship between the wall- and bedrock lithology, morpho-tectonic elements, and the numerical and typological variation in the  $IncTal_{lith/grad}$  index, particularly in those cases where strange lithologies such as ore mineral deposits (copper) and industrial mineral deposits (feldspar pegmatoids and tectonized talc deposits) are intercalated in the common rock-forming mineralizations of the country

rocks (Figure 9a,d–i) [25,85]. The feldspar pegmatoids, when considered in longitudinal sections, crop out in the upstream parts of a type 1 knickpoint, excluding section X1–X2 where a complex mixed type of knickpoints 1 and 2 marks the position of the largest pegmatoid field in the study area (Figure 9c–f). Talc deposits are lined up like pearls on a string along the fault zone between the Prasinite-Phyllite Series and the Marginal Amphibolite and geomorphologically characterized by knickpoint 2 anomalies (Figure 9c,d). A rather complex situation can be recognized in the longitudinal section of profile X7–X8 where several Cu deposits and talc deposits different in their knickpoint types share the same mining district (Figure 9c,g). The northwesternmost Cu deposits, when crossed by channel systems of the longitudinal sections X9–X10 and X11–X12, reveal a pronounced knickpoint 1 anomaly with the ore bodies always being located in their upstream parts (Figure 9c,h,i).

*Horizontal sinuosity—lithology plus gradient ( $HoSi_{lith/grad}$ ):* Similar to the  $VaSi_{alt}$  and the  $VeSi_{val}$ , the  $IncTal_{lith/grad}$  should also be run in combination with another index, reaping the benefits by capturing data from the same landform but viewed from different angles. The  $HoSi_{lith/grad}$  unravels the evolution of a drainage system on a (sub)horizontal level perpendicular to the linear erosion expressed by the talweg and thereby enhances the genetic discussion of the entire fluvial landform under consideration (Figure 9c). The sinuosity of drainage systems is the most common parameter dealt with in textbooks on fluvial dynamics [2,86,87]. The foundation stone for a more detailed study of river sinuosity has been laid by Schumm [88] based upon which several follow-up studies have been conducted, putting forward some equations and providing numerical parameters to describe the sinuosity of a fluvial channel system [89–93]. We elaborated a numerical parameter for the horizontal sinuosity index that is different from the vertical sinuosity lithology ( $VeSi_{lith}$ ) only by the orientation of the plane of reference (Figure 7a). It is applied in accordance with the classification scheme of the sinuosity of fluvial landforms in a foreland–basement transition of the paleosurface 1 to the landscape of paleosurface 2 under study in the current paper so as to allow for a direct comparison of the various sinuosity degrees from the headwaters to the Bamberg Bowl [29] (Figure 3a). An ideal straight channel yields a sinuosity degree of  $S = 1.0$ . The continuous increase in channel sinuosity is categorized as follows: straight:  $<1.1$ ; low-sinuosity: 1.1 to 1.3; high-sinuosity: 1.3 to 1.5; moderately meandering: 1.5 to 2.0; strongly meandering: 2 to 5; and very strongly meandering with sedimentary trap sites as an outlet  $> 5$  [29]. In the study area, the sinuosity values range from “straight” to “moderately meandering” (Figure 9c).

There are two downstream increasing sinuosity trends visible, with the first one confined to the relief generations R1 and R2 (Figures 3f,g and 9c). The highest values are recognized in a zone oriented NW–SE parallel to the boundary between the paleoplain and the step-fault plain (maximum values 1.459 and 1.513). The second trend is controlled by the transition from the basement into the foreland where values of 1.314 and 1.322 are achieved. This common trend observed in foreland areas is a function of gradient and grain size.

## 4.2. Parautochthonous and Allochthonous Mineralogical–Petrological Composition and Landforms

### 4.2.1. The Landform Index and Compositional Changes

The landforms and their indices dealt with in Section 4.1 refer, in the majority of cases, to erosional landforms. The landforms, indices, and rocks dealt with in the current Section 4.2 refer exclusively to depositional landforms and their pertinent sediments to correlate them by means of petrological and mineralogical rock fragments (Table 1). The unconsolidated rocks scattered across the basement and the proximal foreland average 57% clay plus silt, 12% sand, 15% pebble and 16% cobble plus boulders. They are the result of fluvial deposition, mass wasting, and a mixture of both of them. The quantity of these

terrigenous sediments considerably differs when passing from the paleoplain, through the step-and-fault plain, and into the foreland plains (Figure 10). It is numerically constrained and recorded by the quantification of fluvial–mass wasting index.

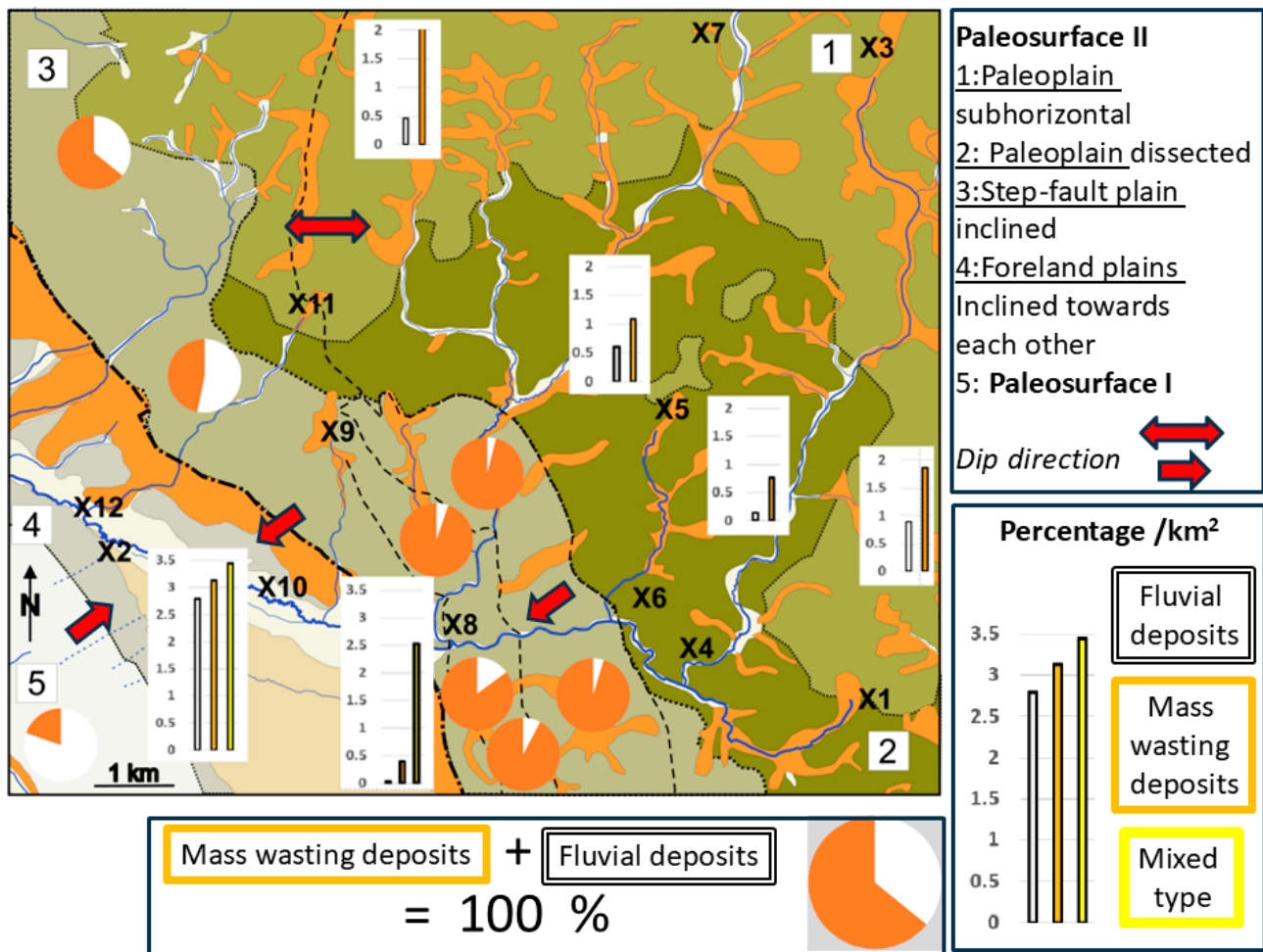


**Figure 10.** Quantification of fluvial and mass wasting deposits as well as their ratios (quantification of fluvial–mass wasting index ( $Quant_{flu/mas}$ )). For geomorphological background, see Figure 3f. 1 + 2: Mass wasting deposits: 2.302 to 0.768 per km<sup>2</sup>, fluvial deposits: 0.888 to 0.135 per km<sup>2</sup>. 3: Mass wasting deposits: 0.457 to 0.061 per km<sup>2</sup>, fluvial deposits: 0.335 to 0.017 per km<sup>2</sup>. 4: Mixed type (mass wasting and fluvial): 3.443 to 0.393 per km<sup>2</sup>, mass wasting deposits 3.132 to 0.393 per km<sup>2</sup>, fluvial deposits: 2.798 to 0.028 per km<sup>2</sup>. 5: Mass wasting deposits 0.019 per km<sup>2</sup>, fluvial deposits: 0.076 per km<sup>2</sup>. In the case of very small quantities of the landform-related mass wasting and fluvial deposits, only the ratio of the deposits is presented as a sector diagram. In the case of very high quantities of these unconsolidated deposits, columnar diagram are used instead.

*Quantification of fluvial–mass wasting index ( $Quant_{flu/mas}$ ):* Quantities of fluvial and mass wasting deposits of the various reference plains are extremely different. Therefore, it is necessary to display the variation in  $Quant_{flu/mas}$  in histograms and sector diagrams for the three principal zones 1 + 2, 3, and 4 + 5 defined in Figure 3b and singled out in Figure 10. Mass wasting products mainly originated from creep, solifluction, minor rock sliding, and rockfall (Table 1, Figure 8a,c,g,h,l,n,p). The fluvial dynamic can be deduced from Figure 4 and has been categorized based upon the  $HoSi_{grad/lith}$  and the  $IncTal_{lith/grad}$  (Figure 9).

Within compartment 1 of Figure 10, mass wasting prevails with a maximum value of 2.30% km<sup>2</sup> over fluvial floodplain deposits. The quantity of the process-related results is given by the percentage value per square kilometer. There is a conspicuous difference between the dissected and undissected paleoplains which points to a mixture of mass

wasting products and parautochthonous regolith that is the transitional zone between soil, sedimentary overburden, landforms, and bedrock sensu Ollier and Payne [94], Taylor and Eggleton [63] and Scott and Payne [95]. In the dissected paleoplain compartment 2, the overall  $Quant_{flu/mas}$  index remarkably changes in favor of fluvial deposits in the northern part, which is indicative of a stronger denudation and fluvial flushing out in the drainage system X7-X8 than in the drainage system X3-X4, draining the area more towards the southeast (Figure 10)

In the SW dipping step-and-fault plain—compartment 3—the overall quantity of unconsolidated fluvial and mass wasting sediments markedly decreases to quantities well below  $1\% \text{ km}^2$  so that pie-chart diagrams reflect the  $Quant_{flu/mas}$  index more conveniently than histograms. This tremendous decrease is due to the fact that it forms the fluvial track and transport zone with a widespread occurrence of V-shaped valleys of acute angles (Figures 4, 5 and 9c). Although there is only a thin veneer of unconsolidated sediments, a marked difference between the NW and SE branch of the step-and-fault plain can be recognized. In the NW branch, northwestward of X9-X10, the fluvial sediments are significantly higher than in the southern one which indicates an overall stronger erosion and flushing out of debris already known from the dissected paleoplain (Figure 10). In the SW branch (SW of X9-X10), relic regolith patches have been preserved on the R1 and R2 relief generations (Figures 3f,g and 10). The mass wasting and fluvial products encountered in the step-and-fault plain are mainly coarse-grained in size originating from rockfall, creep, and flow along the steep slope and bluffs as far as the gravity driven processes are concerned.

Heading further downstream into the foreland, the absolute maximum of deposition increases again, similar to compartment 1 (mixed-type mass wasting–fluvial deposits: max.  $3.44\% \text{ km}^2$ , mass wasting deposits: max.  $3.13\% \text{ km}^2$ , fluvial deposits: max.  $2.80\% \text{ km}^2$ ). The foreland landforms are made of floodplain deposits, paired terraces, a large hillwash depositional plain, and relic pediments. The mixed-type fluvially reworked sediments predominate (Figure 10).

#### 4.2.2. Mineralogy and Petrography of Parautochthonous and Allochthonous Rocks

The unconsolidated sediments show a bimodal distribution with a first-order maximum among the fine-grained sediments and a second-order one among the coarse-grained part of the clastic sediments (see above Section 4.2.1). The marker minerals and rocks are split into clay minerals, light minerals, heavy minerals, and rock fragment suites (Table 1). The basis for that categorization is the classical particle grain-size scale put forward by Udden [96] and Wentworth [97] and published in Friedman et al. [56]: (1) gravel (>20 mm, pebble, cobble plus boulder), (2) sand (63 to 2000  $\mu\text{m}$ , very fine- to very coarse-grained sand), and (3) clay and silt < 63  $\mu\text{m}$ .

*Clay-silt-sized fraction* ( $Quant_{cla/sil}$ ): The finest fraction is very homogeneous in the foreland and step-and-fault plains and characterized by the tripartite group of mica, illite, and chlorite. In the step-and-fault plain, talc appears and in the paleoplain, kaolinite, vermiculite, and serpentine (lizardite) increase among the suite of phyllosilicates. It has to be noted that, without any doubt, the tripartite phyllosilicate group is of allochthonous origin, whereas talc is of hypogene origin and kaolinite, vermiculite, and serpentine are predominantly of supergene derivation [98]. This index has only been handled qualitatively for technical reasons (Table 1). Only the Rietveld refinement applied during XRD can provide reliable results in this case for the fine-grained sediment fraction [99]. This method has been sporadically used only for the foreland sediments, obtaining the results as follows: muscovite + illite (3.56–19.11%), chlorite (1.31–6.06%).

*Sand-sized light and heavy mineral fraction (QuantSan):* The light mineral fraction in the study area ( $Quant_{san/light}$ ) is characterized by a rather monotonous mineral assemblage in the three basic plains (Figure 11a). Nevertheless, its genetic value is rather high for the land-forming processes owing to the minerals' different resistance to weathering and attrition. This idea is corroborated by the sharp breaks in the quantity of the various light minerals [100–103] (Figure 11a, Table 1). A sharp break lies between sampling sites 4 and 6 where downstream orthoclase is out. By contrast, the heavy mineral assemblage is very variegated but with little change along the talweg (Figure 11b) ( $Quant_{san/heav}$ ). It has an edge over light minerals regarding the provenance of sand-sized rock fragments and also for chemical weathering [18,49,104–107]. Significant qualitative changes only occur along the FLFZ as the rivers debouch their debris into the foreland plain (Table 1, Figures 2a and 4p,r,s). During their flow down the basement, moderate quantitative changes can be observed, yet they are a significant expression as to the provenance (Figure 11b).

*Pebble–cobble–boulder fraction (Quant<sub>grav</sub>):* The gravel fraction plays a significant role as a temporary host of the light and heavy minerals on gravity- or fluvially-driven transport from the source rock to their intermediate sediment traps and it is a measure of the transport capacity of the drainage and the gravity-driven land-forming processes [108–112]. The most variegated gravel suite is found in the step-fault plain (Table 1, Figure 11c). The gravel assemblage shows some typical breaks between sampling points 4 and 6 where gneisses show a sharp decrease but did not completely disappear from the gravel fraction. The tributary characterized by sampling points 13, 14, and 15 is a reasonable explanation for the gneiss's reappearance at sampling point 3 downstream of the confluence. Another marker for the changing hydrodynamic regime is the meta-basic magmatic rocks. Similar to many of the remaining indices treated earlier in this paper, the gravel and sand fraction should always be analyzed together to assess the decomposition of coarse-grained sediments  $Quant_{Grav_{lit}}$  and the release of heavy  $Quant_{san}$  and light minerals  $Quant_{San}$  into the depositional systems which facilitates the study of material properties of coarse-grained sediments and the vulnerability of the heavy and light minerals (Figure 11a,c).

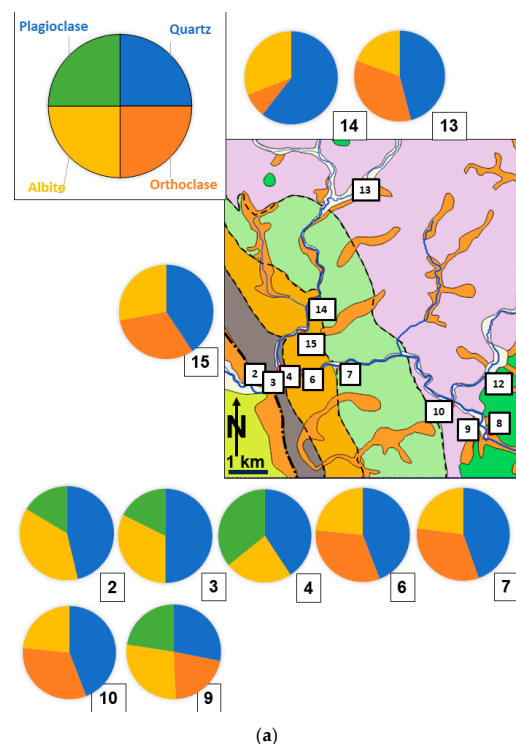
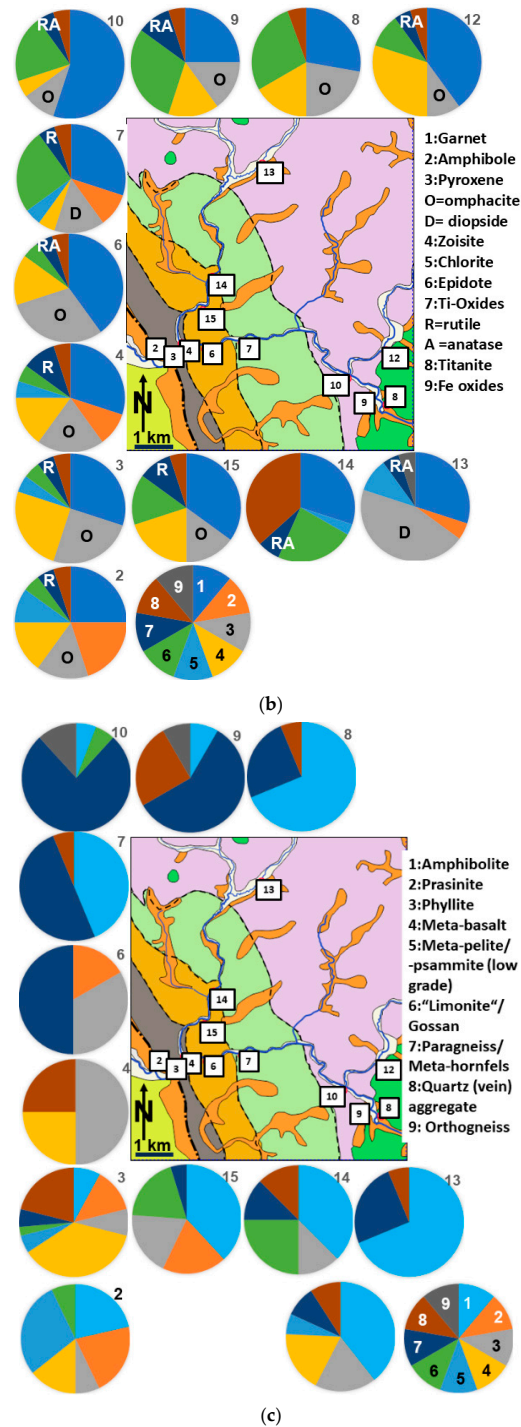


Figure 11. Cont.



**Figure 11.** Composition of siliciclastic deposits of the study area. For geology of the sampling sites, see Figure 2a. The mineralogical and petrological composition is given by sector diagrams (100%). (a) Abundance of sand-sized light minerals (Quant<sub>san/lig</sub>). (b) Abundance of sand-sized heavy minerals (Quant<sub>san/heav</sub>). (c) Abundance of gravel-sized debris (Quant<sub>grav/lith</sub>).

### 4.3. Mineralogical–Petrological Composition and Landforms of Gravel-Sized Allochthonous Rocks

#### 4.3.1. The Gravel-Bearing Landforms and the Hydrodynamic GMS Indices

Gravel deposits are common to a wealth of landforms predominantly in the base-ment resulting from fluvial and mass wasting processes (Figure 8a–c,e,h,l,o,p). The feature landforms prone to the accumulation of gravel-sized siliciclasts are the different types of valleys from the top slope to the fluvial bedforms (Figures 4 and 12). The most striking hydrodynamic landforms favorable for gravel accumulation are lo-

cated along the tectonic contact between two different tectonic series of the step-fault peneplain (Figure 2a,b—units 11 and 12) where gravel beds with anomalously high GMS indices came to rest (Figure 12a,b). There exists a conspicuous short-distance change in the small floodplains of non-alluvial and alluvial channel systems which, in places, are choked with gravel-sized clasts in side- and mid-channel longitudinal bars (Figure 12a,b). A widening of the drainage systems in a V-shaped valley with a small raised side bar on the slip bank is observed just before crossing the boundary from the step-and-fault plain towards the foreland plains (Figure 12c). The contrast could hardly be more striking than between the V-shaped and the wide-angle valleys shown in Figure 12d,e. Wide angle valleys show a considerable floodplain with gallery forests lined up along the meander belts on the paleo-plain Figure 12d. Two valleys are found to be telescoped into each other at the transition from the paleo-plain to the step-and-fault plain, giving rise to a rolling hill landscape.

A tripartite approach has previously been taken to study gravel-sized rock fragments from various environments to support the geomorphological terrain analysis in certain landform series. The acronym GMS method has been coined to pinpoint the focus of each of these applications: (1) the granulometry of gravel-sized clasts, (2) the morphology of gravel-sized clasts, and (3) the situmetry of gravel-sized clasts. While the technical terms of methods 1 and 2 are self-explanatory, situmetry needs a more detailed explanation as this term is not yet well entrenched in the fieldwork of geomorphologists and not ubiquitous in the resultant publications. This method has been used as a stand-alone method in colluvial, fluvial, and glacial deposits [6,113–116].

Textural measurements on a microscopic scale are common in structural geology and petrology since the universal revolving table has been designed and used for oriented thin sections under the petrographic microscope. This method cannot deliver reliable results for the depositional landforms under consideration. The current method applied to coarse-grained gravel, however, is a supportive measure to geomorphological mapping in the field. The key element of this technique is the measurement of the orientation of the elongated axes of gravelly clasts.

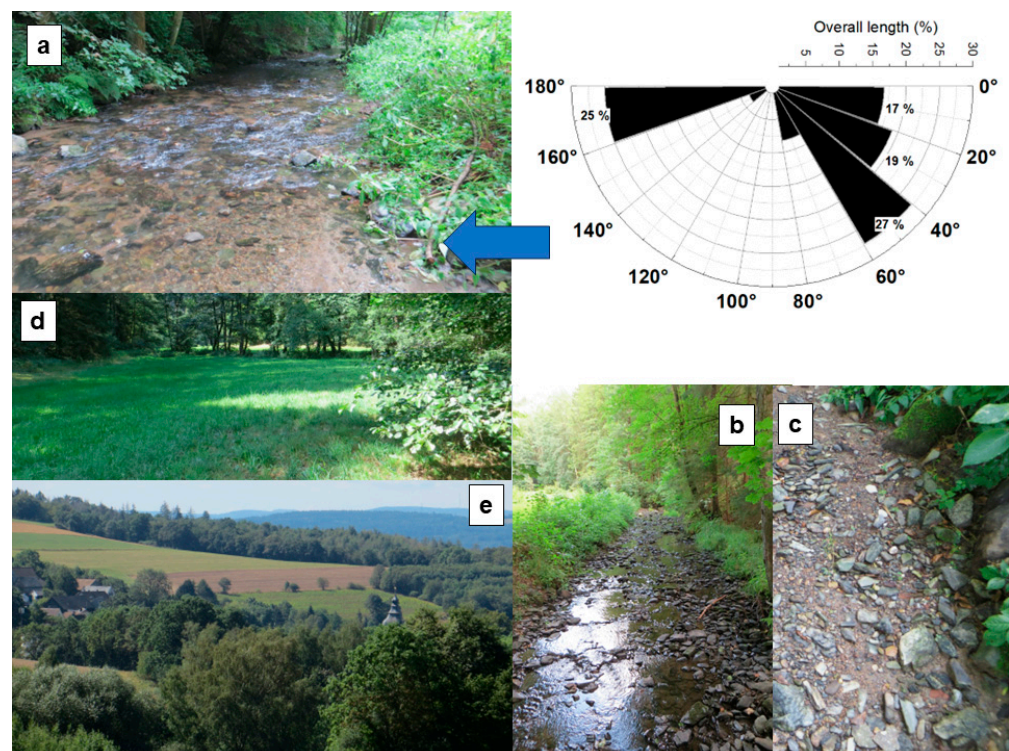
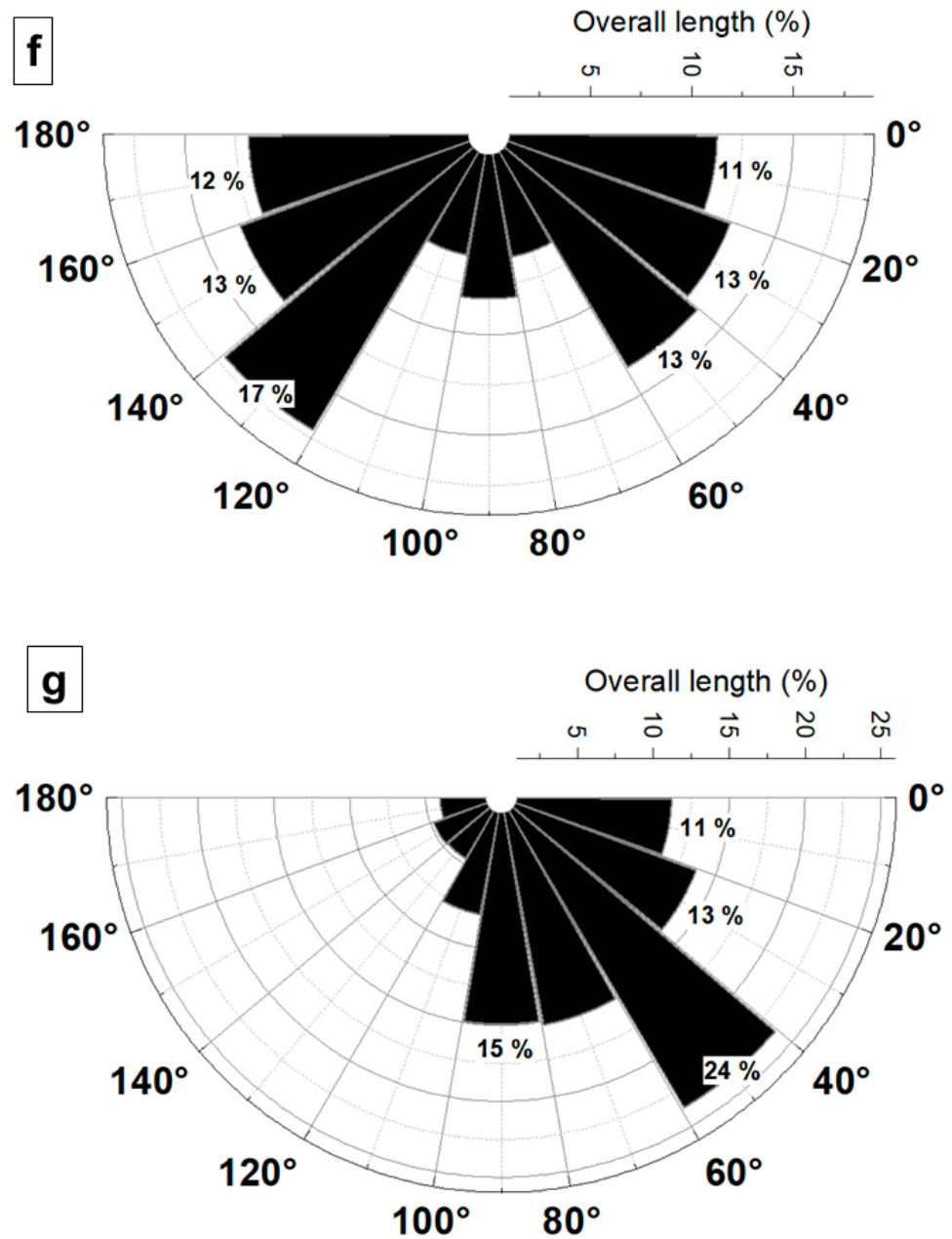


Figure 12. Cont.



**Figure 12.** Landforms hosting gravel-sized debris accumulations subjected to GMS analyses (granulometry–morphometry–sitometry). For sampling sites, see the geological setting presented in Figure 11 and the legend on display in Figure 2a,b. (a) A V-shaped valley (acute angle 22 to 25°) with a small floodplain narrowing upstream towards a gorge (alluvial to non-alluvial). The inset sitogram shows a bimodal clast orientation. Sampling site 7. (b) Non-alluvial V-shaped valley (acute angle 25 to 30°) choked with gravel-sized clast and concentrated in side- and mid-channel longitudinal bars. Sampling site 15. (c) V-shaped valley with a small raised side bar on the slip bank (wide angle 5 to 11°) Sampling site 2. (d) Wide valley (angle 5 to 15°) showing a floodplain with gallery forests lined up along the meander belts,  $S = 1.407$ . Sampling site 12. (e) Two valleys telescoped into each other. The large and shallow valley (angle  $\ll 10^\circ$ ) is cut by an acute V-shaped valley near the FLFZ. Sampling site 13 photography facing towards the W with the scarpland on the horizon. (f) A polymodal clast orientation representative of different landscape-forming processes superimposed on each other. Sitogram of sampling site 15. (g) Unimodal clast orientation preserved on the raised sidebar of a slip bank. Sitogram of sampling site 2.

### 4.3.2. Granulometry of Gravel-Sized Debris (QuantGrav<sub>gran/sort</sub> QuantGrav<sub>gran/moda</sub>)

The granulometry of clastic sediments in laboratories is a routine analysis, particularly when conducted as sieve or CAMSIZER analyses for medium- to fine-grained clastic sediments. This classification method looks back on a long history during which different parameters and indices such as the C/N index have been elaborated [117–120]. By contrast, measurements of coarse-grained unconsolidated clastic sediments are a bit eclipsed and normally fieldwork of this sort is only performed by a few sedimentologists or geomorphologists [121–123]. During the present investigations, the common indices used in sedimentology have been tested, but only two of them warrant application side-by-side with the aforementioned land-forming indices during the current geomorphological investigations. One is the grain size distribution for the classification of the sediments (coarse to very coarse gravel) and for fine-tuning the sorting index QuantSed<sub>gran/sort</sub> which has been calculated as  $QuantSed_{gran/sort} = SQR(Q3/Q1)$  (SQR: square root, Q3: 75% quartile, Q1: 25% quartile). The QuantSed<sub>gran/sort</sub> shows high values in the downstream part of X1-X2 before the river debouches its debris into the foreland.

Where the inclination of the talweg attains values of as much as 30°, e.g., in drainage systems X7-X8 and X1-X2, similarly high values are recognized for QuantSed<sub>gran/sort</sub> where knickpoints of type 2 occur and are indicative of intermediate sediment traps (Figure 13a). In the foreland proximal to the basement, the QuantSed<sub>gran/sort</sub> does not exceed 1.581. Another index directly linked to the QuantSed<sub>gran/sort</sub> is the modality of the graph of the grain-size distribution QuantSed<sub>gran/moda</sub>, which more frequently is unimodal than bimodal. Only in one site with the highest score ever measured in the sediments, a QuantSed<sub>gran/sort</sub> of 3.576, is a trimodal grain-size distribution identified (Figure 13).

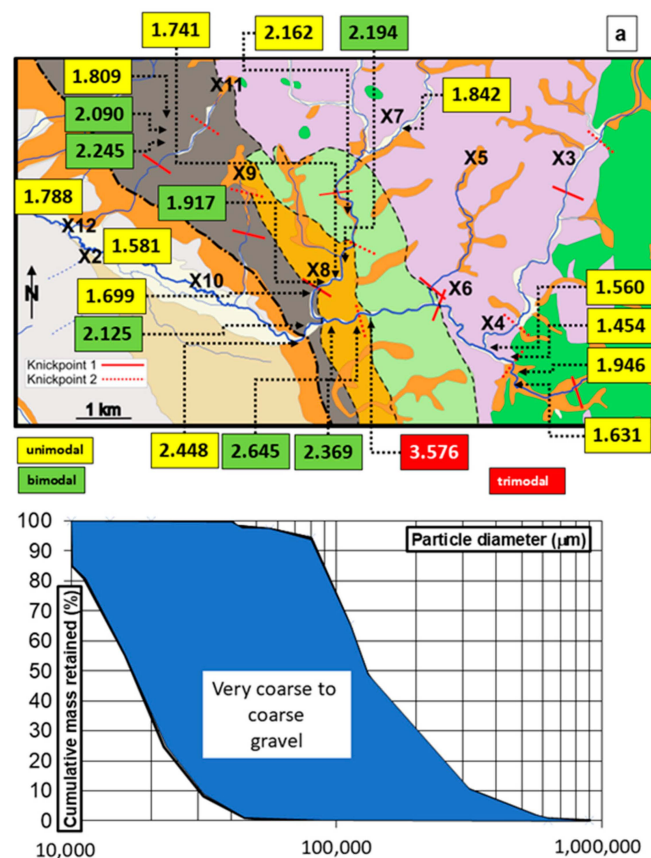
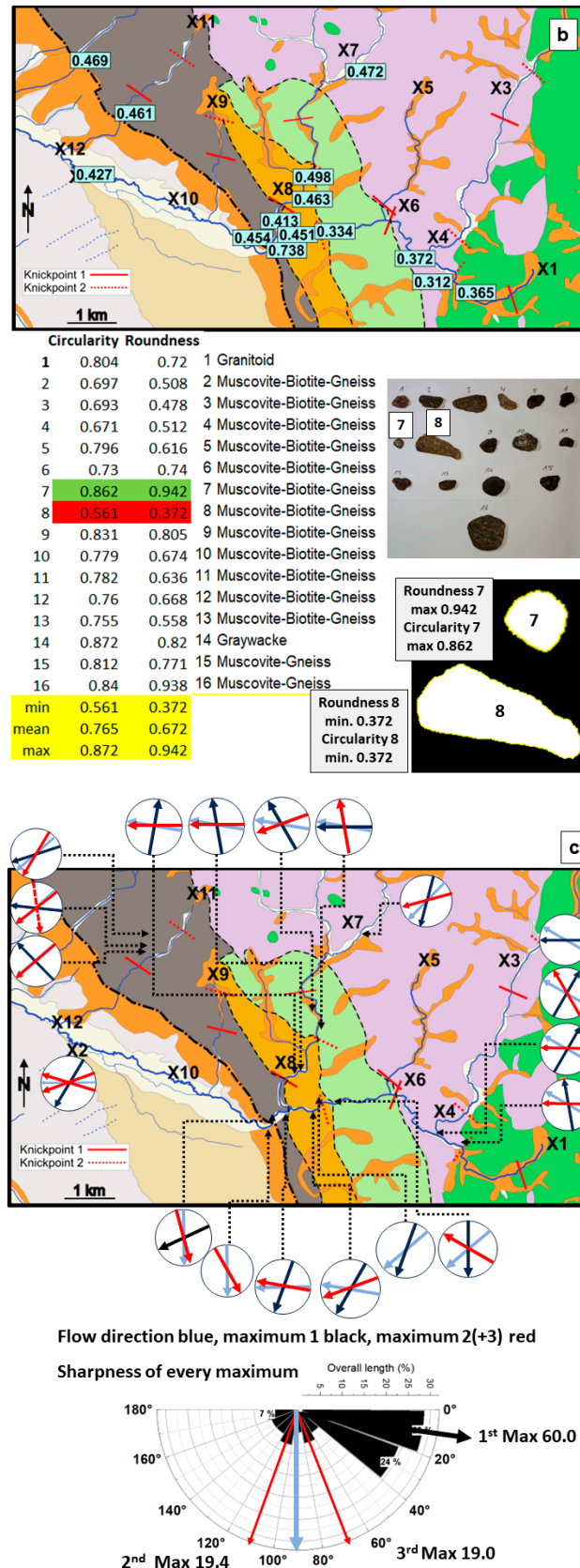


Figure 13. Cont.



**Figure 13.** GIS indices (granulometry–morphology–sitometry) and their fluvial networks of the X1–X2 drainage system and its tributaries X3–X4 and X7–X8. For more details on the numerical parameters of the drainage systems, see Figure 9, and for geology, Figure 2. (a) Granulometry of gravel-sized debris illustrated by the numerical index  $QuantSed_{gran/sort}$  with a cumulative frequency grain-size distribution of all samples from the study area above represented by the blue shaded area.

(b) The regional variation in the minimum values of the  $\text{QuantSed}_{\text{morp}/\text{roun}}$  of gravel-sized debris (map above) and a reference site showing the  $\text{QuantSed}_{\text{morp}/\text{roun}}$  compared with the  $\text{QuantSed}_{\text{morp}/\text{cycl}}$  numerically and visually for the most widespread lithology of the study area, the muscovite-biotite gneisses. (c) Situmetry of gravel-sized debris illustrated by  $360^\circ$  circle diagrams showing the true orientation of the river course and of various maxima of the longest axis of gravel clasts (**above**). The reference samples show a topographically non-oriented semi-circle rose diagram with a trimodal arrangement of gravel clasts with a sharpness of maximum as follows: first maximum 60.0, second maximum 19.4, and third maximum 19.0.

#### 4.3.3. Morphometry of Gravel-Sized Debris ( $\text{QuantGrav}_{\text{morp}/\text{roun}}$ $\text{QuantGrav}_{\text{morp}/\text{cycl}}$ )

The most successful way to give an insight into the environment of formation is based on the grain shape of the siliciclastic sediments which is normally expressed by the roundness and the sphericity of clasts [108,124–126]. These grain shapes can be determined based on visual inspection as compared to reference charts or by calculating various indices as performed in the present study where two well-defined LFIs, the quantification of roundness ( $\text{QuantSed}_{\text{morp}/\text{roun}}$ ) and the quantification of the cyclicity ( $\text{QuantSed}_{\text{morp}/\text{cycl}}$ ) are computed by means of image analysis on PC. Both procedures can be performed simultaneously for each individual grain as tested by Matsumoto et al. [127]. The statistical treatment resembles the suggestions put forward by Owczarek [128].

*Circularity* is defined as  $4 \pi \cdot A/P^2$ , where A is the area, and P is the perimeter of the grain. Values close to 1.0 are close to a perfect circle. As the value approaches 0.0, it indicates a grain with an increasingly elongated shape.

*Roundness* is defined as  $4 \cdot A/(\pi \cdot x^2)$ , where A denotes the area and x the major axis. For a more detailed interpretation of the downstream variation, the difference between the mean and minimum values is calculated.

Both LFIs positively correlate with each other (mean values:  $R = 0.76$ , maximum values: 0.90) (Tables 2 and 3). During routine geomorphological mapping in the field without any need for lithological fine-tuning, the use of the  $\text{QuantSed}_{\text{morp}/\text{roun}}$  and the  $\text{QuantGrav}_{\text{morp}/\text{cycl}}$  indices have been proven to deliver reliable and satisfying results (Table 3). The morphological parameters of the tripartite GMS analytical set used for hydrodynamic aspects and depositional landforms are the only ones which reveal a highly positive correlation between  $\text{QuantSed}_{\text{morp}/\text{roun}}$  and  $\text{QuantSed}_{\text{morp}/\text{cycl}}$  on the part of depositional landforms and  $\text{VaSlAn}_{\text{norm}}$  and the  $\text{VeSi}_{\text{lith}}$  on the part of erosional landforms because both pairs are governed by the interaction of land-forming processes and rock-mechanical/petrophysical properties of bedrock and their pertinent sediments. It is the rock strength, anisotropy, and cleavage which have implications on the attrition during any aquatic and/or gravitative transport and in situ supergene alteration.

The LFIs significantly differ from each other by their scale of application. The first-mentioned pair considers the size of a well-defined outcrop along a slope hundreds of meters in length; the second pair is applied to hand specimens. The good correlation and anti-correlation for the study area are given in Table 3a and color-coded as follows: one hundred to seventy green, seventy to forty yellow, thirty to zero brown, and negative correlation red. At first glance, the regional variation in the  $\text{QuantSed}_{\text{morp}/\text{roun}}$  does not seem very pronounced, but there is one section where the LFI conspicuously diminishes along the boundary of the paleoplain to the step-and-fault plain and another within the latter one where the  $\text{QuantSed}_{\text{morp}/\text{roun}}$  rises tremendously along a fault zone.

**Table 3.** Indices showing the material properties of rocks on a different scale.

(a) Correlation of QuantSed<sub>morp/roun</sub> and QuantSed<sub>situ/dyna</sub> versus VaSIAn<sub>norm</sub> and VeSi<sub>lith</sub>.

	QuantGrav <sub>morp/cycl</sub> Min	QuantGrav <sub>morp/cycl</sub> Mean	QuantGrav <sub>morp/cycl</sub> Max	QuantGrav <sub>morp/roun</sub> Min	QuantGrav <sub>morp/roun</sub> Mean	QuantGrav <sub>morp/roun</sub> Max	VeSi <sub>lith</sub> Mean	VeSi <sub>lith</sub> Max	VaSIAn <sub>norm</sub> Mean
QuantGrav <sub>morp/cycl</sub> min	1.00								
QuantGrav <sub>morp/cycl</sub> mean	0.57	1.00							
QuantGrav <sub>morp/cycl</sub> max	-0.09	0.76	1.00						
QuantGrav <sub>morp/roun</sub> min	0.95	0.35	-0.34	1.00					
QuantGrav <sub>morp/roun</sub> mean	0.52	0.76	0.48	0.32	1.00				
QuantGrav <sub>morp/roun</sub> max	-0.49	0.43	0.90	-0.69	0.29	1.00			
VeSi <sub>lith</sub> mean	0.59	0.67	0.25	0.50	0.82	0.04	1.00		
VeSi <sub>lith</sub> max	0.69	0.69	0.21	0.63	0.73	-0.06	0.97	1.00	
VaSIAn <sub>norm</sub> mean	0.57	0.05	-0.30	0.66	-0.05	-0.57	-0.08	0.10	1.00

(b) The major rocks from the study area and their QuantSed<sub>morp/roun</sub> and QuantSed<sub>situ/dyna</sub> minimum, mean, and maximum values.

Rock	Circularity (Min)	Circularity (Mean)	Circularity (Max)	Roundness (Min)	Roundness (Mean)	Roundness (Max)
Amphibolite	0.613	0.759	0.865	0.365	0.707	0.958
Amphibolite (mixed type with hornblende and epidote), marginal amphibolite	0.531	0.722	0.811	0.334	0.617	0.899
Metabasalt	0.631	0.764	0.873	0.413	0.692	0.947
Prasinite (Ep-amphibolite)	0.640	0.736	0.813	0.448	0.612	0.845
Mica gneiss (endif.)	0.553	0.753	0.873	0.312	0.655	0.971
Phyllite (including quartz phyllite)	0.595	0.761	0.876	0.370	0.631	0.966
Metahornfels	0.715	0.765	0.833	0.540	0.698	0.867
Slate	0.766	0.811	0.865	0.586	0.772	0.910

4.3.4. Situmetry of Gravel-Sized Debris (QuantGrav<sub>situ/dire</sub> QuantGrav<sub>situ/shar</sub>)

The determination of the orientation of clasts in aquatic systems is the third tool for the classification and interpretation of unconsolidated coarse-grained sediments under various hydrodynamic conditions (Figure 13c). During the first step, the orientation of the elongated axis of the clasts is measured relative to a base line perpendicular to the channel axis and plotted into semi-circle rose diagrams as shown in Figures 12a,f,g and 13c. In a follow-up re-orientation, the true directions of the various maxima (unimodal, bimodal, and trimodal) are recalculated and plotted into a full 360° diagram and positioned in a geological map (Figure 13c). This topographic orientation of maxima is coupled with the intensity of the different maxima and called fan sharpness. The fan sharpness is representative of the percentage of the maximum and the intensity of each of its neighboring sectors on the left and right-hand side. The diagrams can reveal a unimodal, bimodal, and trimodal distribution as attested to by the triplet of gravel maxima composed of a very strong first maximum of 60.0, second maximum of 19.4, and third maximum of 19.0 of almost the same size, and a bilaterally symmetrical arrangement of maxima, the projections of which intersect each other at an acute angle of 40° (Figure 13c). The majority of the situgrams are bimodal and symmetrically orientated relative to the orientation of the river run with various angles of intersection of their maxima. There are patterns of orientation where the river run no longer forms the bisecting line of the acute angle of intersection but is still being placed within the sector of the acute angle, while in a few sites the river run intersects the obtuse angle. Unimodal circular patterns always show an acute angle between the direction of the river run and the maximum, whereas trimodal patterns used to consist of a bilaterally symmetrical arrangement of maxima with different angles of intersection and a third maximum with an orientation strongly depending on the type of drainage system as exemplified by the coarse-grained meandering stream drainage system typical of the strike streams of the foreland plains and recorded by some authors [129–131] (Figures 3b and 13c).

### 5. Discussion

#### 5.1. A Numerical and Compositional Subdivision of a Terrain for Genetic and Applied Geomorphology

Different approaches are taken by geoscientists when it comes to a terrain analysis, driven first and foremost by the study groups’ orientation towards application and/or genetic scopes, and secondly, by which discipline the scientists come from in terms of methods and focal discipline [13,132–136]. The scientists may come from different working disciplines running the gamut from pure geosciences to computer sciences and they cater to different end users and peer groups such as those from earth sciences, environmental sciences, ecology, civil engineering, and even as an auxiliary subject in military operations, and therefore, the pros and cons for different approaches are viewed from different perspectives. The current point of view is based on the “E & E issue” (extractive/economic geology in accordance with environmental geology), in which the senior author has been engaged for the past 48 years, making material sciences, compositional changes, and the role of pathfinders to mineral deposits the centerpiece and missing link between descriptive and numerical geomorphology and, thus, providing a platform for geomorphometry and economic geology [17,19,24] (Figure 14).

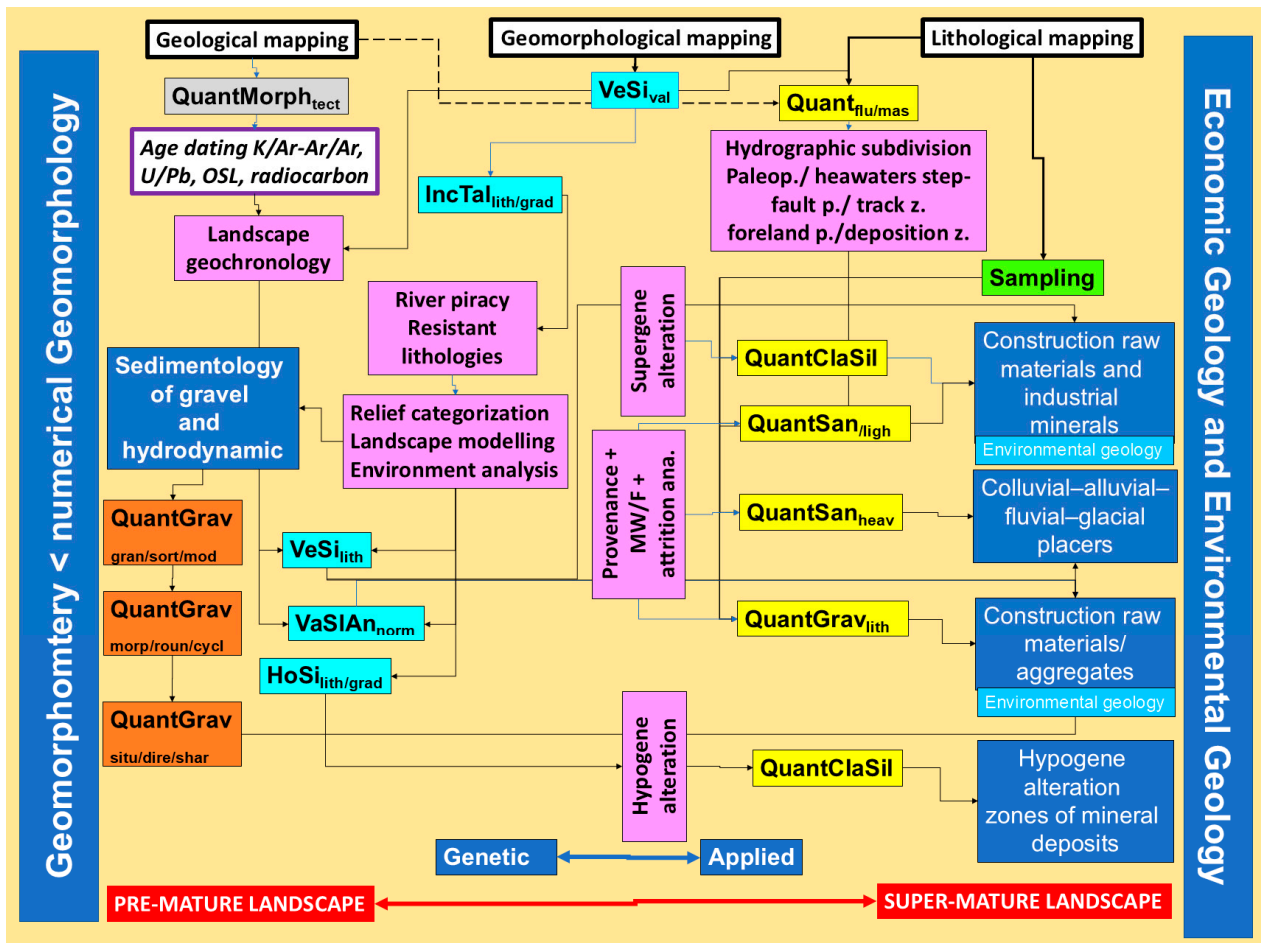


**Figure 14.** The manual from fieldwork (geological, geomorphological, and lithological mapping) to numerical geomorphology > geomorphometry (genetic geosciences) and economic and environmental geology (applied geosciences). The landform indices are the missing links. See also Table 1.

In Figure 14, the interconnectedness of fieldwork and the scope of numerical geosciences is depicted in a flowsheet. The various landform indices (LFIs) act as the link between the methods and the scope targeted during this study.

Unsurprisingly,  $VeSi_{val}$  and  $Quant_{flu/mas}$  are the key indices to start this terrain analysis, acting as a leverage for the tripartite subdivision of the study area in what might be called a geomorphological exploration which caters to the genetic and applied sub-disciplines of economic geology and geomorphology alike (Table 1, Figures 3b and 10). The tripartite geodynamic-geological subdivision corresponds to the tripartite subdivision into the (1) paleoplain (2.58), (2) step-fault plain (0.67), and (3) foreland plains (1.12). It is numerically backed by the M/F ratio—mass wasting vs. fluvial deposits—shown in rounded brackets beside each reference plain (Figure 3b, Table 1). The ratio is computed from  $Quant_{flu/mas}$ , excluding the 10 m terrace sediments, a mixture of fluvial and mass wasting deposits in a wedge-shaped hillwash plain (Figure 2a).

The  $VeSi_{val}$  index is representative of the relief of the erosional landform series whereas the  $Quant_{flu/mas}$  index is elaborated for the depositional landform series. It is thus the second string in the bow in subdividing a terrain made of both depositional and erosional landform series (Table 1, Figure 4). The tripartite subdivision is compatible with the common hydrographic downstream compartmentalization of fluvial drainage systems that evolves from the (1) headwater zone, through the (2) track/transport zone, and into the (3) depositional zone. The numerical values of the  $Quant_{flu/mas}$  index are correlated with the sediment load of the various zones. The flushed out track zone No. 2 is the zone most depleted in unconsolidated sediments, whereas the depositional zone No. 3 is most strongly enriched in unconsolidated debris (Table 1, Figure 10). The  $Quant_{flu/mas}$  index is associated with the grain size-related indices ( $Quant_{ClaSil}$ ,  $Quant_{San}_{/ligh}$ ,  $Quant_{San}_{heav}$ , and  $Quant_{Grav}_{lith}$ ), forming together the pathway into economic geology mainly composed of the syngenetic accumulation of heavy minerals in colluvial, alluvial, and fluvial placer deposits. The concentration of fine-grained raw construction materials by supergene alteration as well as the formation of hypogene industrial mineral deposits surrounded by specific alteration zones are different in their origin but to be handled by the same index,  $Quant_{ClaSil}$ , since they do not differ from each other in outward appearance [24,25,98] (Figures 9c and 14).

### 5.2. The Paleoplain and Its Dissection—The Headwater Zone

The paleoplain is characterized by subhorizontal bosselated morphological planar elements depicted as planed uplands with some monadnocks rising to a height of as much as 668 m (Figure 3b). Such landscapes, made of gently undulating plains with no pronounced features of relief, excluding some isolated monadnocks and escarpments at the margin, have been investigated by several researchers using various mechanisms to develop these landform series such as peneplanation, pediplanation, pedimentation, etchplanation, and mixed types described as staircase peneplain-pediment-types [58,137–146]. To decipher the different relief generations and their corresponding  $VeSi_{val}$  and  $VaSlAn_{alti}$  indices, a profile from the highest mountain, the Döbraberg summit, situated outside the study area in the FWM proper, to the transition into the step-fault plain has been plotted as a true-to-scale line drawing for comparison (Figures 1b and 15).

The relief generation R0 characterizes the uppermost peneplain which developed around 17 Ma based upon the age of the formation of unconformity-related supergene Fe-Mn (K/Ar—dating) in the study area and the neighboring Frankenwald and Fichtelgebirge Mts (Figures 3f,g, 4f,t,u and 15a). A couple of K-Mn-bearing ferricretes containing cryptomelane formed as a consequence of paleo-hydraulic changes such as oscillating water tables. These Mn minerals yield excellent tools for dating land-forming processes, and were used in this case to chronologically constrain peneplanation or etchplanation processes in the study area [147–151].

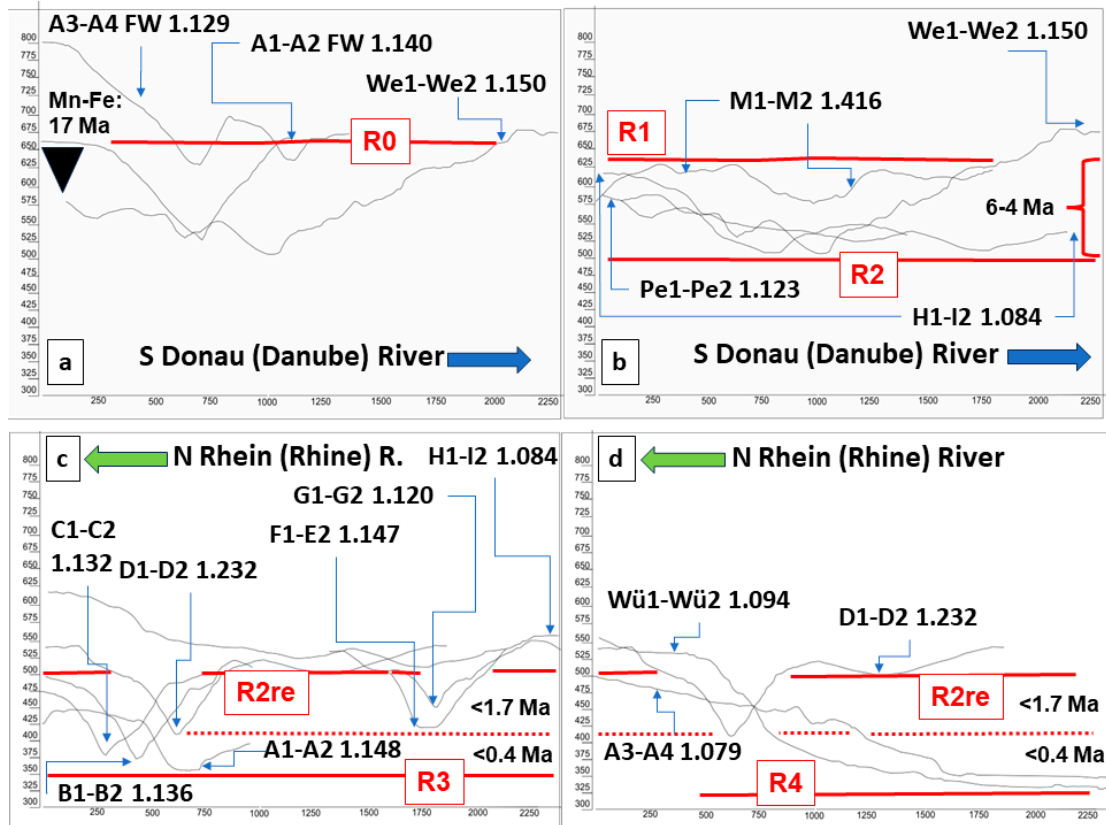


**Figure 15.** The evolution of landscape and re-orientation of the drainage system from the ancient Donau River to the modern Rhein River systems on display as a series of landscape contours true to scale as a function of altitude and distance based upon the  $VeSi_{val}$ ,  $VaSIAn_{alti}$ ,  $IncTal_{lith/grad}$ , and geochronological data (for reference, see text). Periods correspond to the relief generations shown in plan view in Figure 3f,g. For the geology and landforms of each cross-section, see Figures 4 and 5. (a) Stage of peneplanation at full swing (R0). (b) Stage of peneplanation (R1) transitioning into pediplanation (R2) (fossiliferous badlands). (c) Stage of the re-orientation of the paleogradient accompanied by river piracy (R2e) and linear erosion (R3). (d) Stage of the re-direction of the fluvial regime from dip to strike stream and perched pedimentation (R4).

The highest mountain in Frankenwald is an inselberg called Döbraberg Mt, and not only forms the highest planar elevation in the study area proper, but is also a relic of the R0 peneplain which can be traced back to the so-called large-and-shallow valley (Figures 5f,t and 15a). Relief generation R1 is another lower paleosurface of the same type as R0 and is accountable for the erosional terraces which are carved out of the Weißenstein Mt. mid-slope (Figures 5f and 15b).

The morphoclimatic adjustment in the aftermath is conducive to the V-shaped valleys and the bosselated paleoplains that are numerically almost identically expressed by the  $VaSIAn_{alti}$  R2 values of 0.470 and 0.468, respectively. This is a composite marker for the gradient and “roughness” of the landscape and also corroborates its index  $VeSi_{val}$ , which oscillates within a narrow range of 1.150 and 1.123 (Figure 15b). The landform setting and numerical portfolio tremendously changes passing into the younger R2 relief generation that developed between 6 and 4 Ma (Figure 15b). The R2 landforms are chronologically constrained by U/Pb radiometric dating recorded by Carl and Dill [152] and another dating conducted with a laser-ablation-inductive-coupled mass spectrometry (LA-ICP-MS) [153]. The targeted minerals belong to the uranyl phosphates and hydrosilicates which formed in the same way as their K-Mn counterpart minerals at the same time but on different bedrocks dependent upon the availability of U, K, and Mn. The  $VeSi_{val}$  shows a downslope

downhill decreasing trend, starting off with a strong erosional dissection of the aforementioned paleosurfaces R0 and R1 with a value of 1.416 and waning with a value approximating 1.084 (Figures 4a,c,h, 5a,c,h and 15b). The trend of indices denotes the paleocurrent during the interval 6–4 Ma, which shows a general direction of N–SSE splitting up into a NW and SE branch (Figure 3f). It also contributes to the categorization of R2 into an unaltered R2 part showing a coherent paleotrend of index values and an altered part called R2e where the  $VeSi_{val}$  is locally increased owing to the younger fluvial linear erosion of R3 in an area where R landform relics are only patchily distributed (Figures 3f,g and 15c).

Unlike the R0–R1 trend caused by peneplanation, the R2 trend attests to a pediplanation caused by a retreat of the mountain front and resulting in a “badland landscape” carved out of a metamorphic terrain. Some papers have been published on the classical badland landscapes in sedimentary basins, but they have not yet covered this type of badlands sculpted out of a metamorphic terrain [154–159]. The plateau is underlain by the Upper Series exposed in the horseshoe-like cuesta controlled by the NE plunging central anticline and shaped by the pre-existing R0–R1 peneplanation. The mesas in the center, surrounded by the gully and wadi zones, form the pediplain and aggradational plains while being underlain by the Lower Series. These landforms are under constant retreat by the R2 land-forming processes and after undergoing some periglacial overprinting and fluvial dissection end up here as a bosselated landscape where all of the badlands’ landforms such as mesas, buttes, gullies, and canons are truncated and their edges beveled so that a picturesque “Monument Valley” can hardly be expected (Figure 4a–i). The paleoplain was gently tilted towards the S and its drainage systems directed to the ancient Donau River (“Urdonau”) (Figures 3b,c and 15a,b).

### 5.3. The Step-Fault Plain and the Fluvial Piracy—The Track Zone

The step-fault plain is inclined towards the SW and homoclinal with the drainage system of the modern track zone, which is connected to the headwaters of the paleoplain (Figures 14 and 15c). The critical hydrographic sites of the drainage system in the track zone are called the “elbow” that marks a conspicuous re-orientation in the river run. It was created by the stepwise river piracy through headward erosion of a younger drainage system tributary to the Rhein River into an older paleodrainage system tributary to the ancestral Donau River (Figure 15a,c).

This fluvial capturing is characterized by a sharp change in the river run of the R3 drainage system from the SE–NW towards the WSW direction. The valley sections also see a change in the  $VeSi_{val}$  from almost constant values between 1.147 and 1.143 along the SE–NW section to a significant downstream increase to as much as 1.232 at D1–D2 (Figures 3f and 4i,k–m). All reference sections, as shown by their  $VaSlAn_{alti}$  index data, are indicative of relict large-and-shallow valleys of the wadi zone typical of the R2re-badland paleodrainage system (Figure 5i–m). The longitudinal sections numerically treated by means of the  $IncTal_{lith/grad}$  reveal a lot of type 1 and 2 knickpoints (Figures 3f and 9). These knickpoints are essential to assessing the recession rate of widespread occurrence between section D1–D2 and H1–H2 cross-sections (Figure 3f,g) [82,160,161]. That is where the paleoplain R2 drainage system had its center of subsidence, and during the deepening of the thalweg R2 drainage system, it was tapped into by the headward R3 erosion (Figures 3 and 15c). The fluvial piracy marks a reversal of the R2 paleo drainage system making its river system tributary to the River Rhein watershed (Figure 4i,k). These mobile knickpoints in the SE propagated upstream leading to a drainage capture whereas the remaining ones in the NW of the step-fault plain are stable knickpoints controlled either by resistant lithologies or fault displacement (Figure 3f). These processes are constrained numerically by the LFI and chronologically by U/Pb radiometric age dating (Figure 15). These LFI data are of utmost importance for

economic geology (see also Section 5.6), whereas mobile ones triggered by relative base-level fall are of relevance for the evolution of the drainage system which evolved in the period of time < 1.7 Ma [23] (Figure 15c). West of D1-D4, another downstream increasing trend is recognized reaching a value of 1.148 at A1-A2 before debouching the sediments into the foreland. The river piracy and connecting of the headwaters and transport/track zone were accomplished in two different periods, <1.7 Ma and <0.4 Ma (U/Pb dating).

The track zone featuring drainage systems rife with unconsolidated gravelly sediments offers a wealth of sites where sorting, or  $\text{QuantGrav}_{\text{gran}/\text{sort}}$ , is a useful tool as an environment marker (Section 4.3.2). GMS-based sorting values rise where the vertical sorting goes up such as in cross-sections D1-D2 and A1-A2 (Figures 4m,p and 13a). Sorting values suddenly increase where type 2 knickpoints occur and intermediate sedimentary traps develop near gorges.

The sister index  $\text{QuantGrav}_{\text{gran}/\text{moda}}$  mirrors similar changes in the land-forming processes. Increasing modalities and sorting bear witness to an increasing admixture of mass wasting material from the footslope of the valleys. Bimodality is accompanied by a slowing down of the paleogradient. The co-occurrence of these hydrodynamic LFIs are also morphotectonic markers for shear zones and last-but-not-least for shear-zone-hosted talc deposits (Figures 9c and 13a).

#### 5.4. The Foreland Plains and the Fault-Bound Escarpments—The Deposition Zone

The indices  $\text{VeSi}_{\text{val}}$ ,  $\text{VaSlAn}_{\text{alti}}$ , and  $\text{IncTal}_{\text{lith}/\text{grad}}$  plus knickpoints demonstrate that the landforms series of the foreland plains are the result of a consequent continuation of the morphotectonic evolution shown in Figure 15c from D1-D2 towards the foreland (Figures 4n-p,r,s and 5n-p,r,s). There is a numerical jump in the indices leading to the lowest values ever calculated for  $\text{VeSi}_{\text{val}}$  and a series of depositional/sedimentary landforms side-by-side with the pre-existing erosional landforms as well as significant knickpoint types 1 and 2 in the drainage systems X1-X2 and X7-X8 (Figures 5r,s, 9c and 15c,d). The planar land-forming processes from R0 towards R2re have completely grinded to a halt and were replaced by the linear ones leading to uplands, an uplifted plateau with a gently sloping crest shoulder on top of the escarpment, a hillwash plain, talus cones, and alluvial fans pointing to a series of perched pediments along the FLFZ (Figures 4r,s, 5r,s and 15d) [137,162]. The morphotectonic relict perched pediments in front of the escarpment face markedly differ from morphoclimatic equivalents of R2 relief generation (Figure 15b,d). The perched pediments underwent a marked fluvial overprinting when dip stream rivers draining out of the basement converted into strike stream ones provoked by stepwise uplifts during the period < 1.7 Ma.

#### 5.5. Erosional Landforms and Material Properties—Lithology and Satellite-Based Terrain Analysis

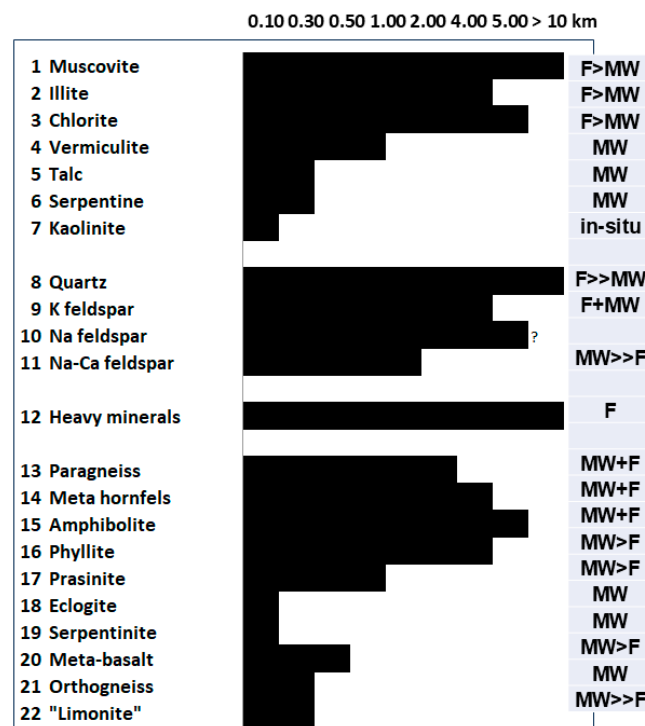
Section 5.5 addresses the bedrock material properties and paves the way from numerical geomorphology/geomorphometry to economic geology and its applied component, geomorphology (Figure 14).

$\text{VeSi}_{\text{lith}}$  which stands for the rock strength and  $\text{VaSlAn}_{\text{norm}}$  which stands for the bedrock anisotropy have a technical and genetic connotation, alike (Figure 7). They play a major part during the satellite-based (or air-borne) mapping which forms the platform of the terrain analysis. They also form a significant step during the in situ supergene and hypogene alteration, both of which leave their imprints on the surface of erosional landforms, thereby becoming relevant for dating geomorphological processes [163–170]. Another index in this study of erosional landforms is the  $\text{HoSi}_{\text{lith}/\text{grad}}$  index, describing how the horizontal sinuosity is driven by the paleo-gradient as well as the substrate that used to increase this index as the

grain size of the bedrock decreases (Figure 14). This is the case when argillaceous supergene or hypogene alteration zones blanket the fresh hard rock [19] (Figure 9c).

5.6. The Depositional Landforms vs. Provenance Analysis and Supergene Alteration

Erosional landforms and depositional landforms are linked to each other as a consequence of mass balance. Over a timespan of roughly 20 million years it can only be approximated using the  $Quant_{flu/mas}$  index (Figure 10). Provenance analysis considering the mineralogical and lithological composition as a function of particle size suffers from mechanical and chemical weathering as well as attrition and can be numerically addressed using  $Quant_{ClaSil}$ ,  $Quant_{San_{ligh}}$ ,  $Quant_{San_{heav}}$ , and  $Quant_{Grav_{lith}}$  (Figures 10 and 11a–c). The fine-grained clay and silt matter frequently attain a maximum in marine sediments of the final sediment trap and thus play only a minor part in this continental environment [171–173]. The vulnerability of the various particles to transport is illustrated by the diagram in Figure 16.



MW = Mass wasting transport  
 F = Fluvial transport  
 In situ = supergene alteration  
 ? = uncertain range of transport

Figure 16. Clay minerals ( $Quant_{ClaSil}$ ), sand-sized light minerals ( $Quant_{San_{ligh}}$ ), heavy minerals ( $Quant_{San_{heav}}$ ), and gravel ( $Quant_{Grav_{lith}}$ ) of different lithologies represented by the range of dispersal off their source rocks.

*Clay minerals ( $Quant_{ClaSil}$ ):* Therefore, the  $Quant_{ClaSil}$  index is used to show the relative abundance that becomes more monotonous further away from the source rock (Table 1). The variegated clay mineral assemblages such as talc and serpentine are only encountered in the immediate surroundings of the talc schists and the ultrabasic rocks of the fault-step plain and on the paleoplain, respectively (Figure 4c,n). Micaceous and chlorite increase downstream and can be assigned to a great variety of metamorphic basic magmatic rocks and para- as well as orthogneiss. Kaolinite, which only occurs in the uppermost level of the study area, is a very rare constituent of the clay mineral assemblage and has been derived from chemical weathering. Using the Koppen–Geiger Climate Chart, such low-kaolinite zonal clay mineral

assemblages only occur in soil and regolith formed under Bs (dry semiarid steppe) and Bw climates (dry arid desert) [174–176]. The presence of labile phyllosilicates such as talc and serpentine accompanied by a scarcity of kaolinite corroborates the idea that semiarid to mildly arid climates occurred during relief generation R2 and R2re.

*Light minerals (QuantSan<sub>ligh</sub>):* This quadripartite light mineral association is only composed of quartz, Na feldspar (albite), K feldspar (orthoclase), and Ca-Na feldspar (plagioclase) minerals which differ from each other in their resistance to weathering. Plagioclase is the most labile member among these silicates and quartz stands out as the least vulnerable one (Figures 2a, 4 and 11a, Table 1). Orthoclase has prevalently been derived from the ortho- and paragneisses of the Lower Series where it is identified in the light mineral association down to site 6 and laid down in the riverbeds on basic and felsic magmatic rocks. Only the latter bedrock is in favor of an input of K feldspar by mass wasting processes (Figure 4j–n). Bedforms filled with K feldspar but carved out of basic rock bear witness to a purely fluvial detrital origin. The feldspar can be tracked over a length of as much as 5 km. Plagioclase is only found from sites 2 to 4 where it has been derived from metabasalt (“diabase”) washed in from the footslope. In the epidote amphibolite, the metamorphic low-grade alteration product of this meta-basalt plagioclase is no longer stable and albite formed instead. Plagioclase has only been found at sites 2, 3, and 4 and site 9, where it has been derived from the on-site or nearby decomposition of metabasalt and layered amphibolitic gneisses in eclogite and amphibolite facies, respectively (Figure 4i,p,s and Figure 11a). Plagioclase is, without any doubt, delivered to the channel by mass wasting, mainly talus creep and flowing or sliding gravel-sized fragments from which it has been released on transport during attrition (Figure 16).

*Heavy minerals (QuantSan<sub>heav</sub>):* The QuantSan<sub>heav</sub> index displays a very variegated heavy mineral suite with its main constituents attaining an amount of up to 40% (garnet). The relative amounts of the heavy minerals do not differ very much from each other so that fluvial transport is held to be the major method of transport (Figure 11c). The presence of pyroxene-group minerals with mainly omphacite s.s.s., the feature mineral of eclogite, was washed in by the X3-X4 drainage system. This drainage system either runs through the Upper Series or within the Lower Series close to it, scavenging the detrital minerals of the high-grade metabasic rocks such as eclogite amphibolite or eclogites proper.

*Gravel-sized lithologies (QuantGrav<sub>lith</sub>):* Four rock types scattering across the drainage system are being tracked over a distance of as much as 10 kms. These are paragneiss, meta-hornfels, amphibolite, and phyllite. On the opposite end of the scale of the transport range, eclogite and serpentinite are positioned. They occur in elevations with blockmeers in proximal positions and boulders strewn at mid-slope and at the top of slopes (Figure 16). Both magmatic rock types decompose very early near their source rock as a consequence of rock fall and sliding blocks and thereby contribute to the variegated heavy mineral spectrum with omphacite and garnet.

The Quant<sub>flu/mas</sub> index, and the in-depth approach taken by QuantClaSil, QuantSan<sub>ligh</sub>, heavy minerals QuantSan<sub>heav</sub>, and gravel QuantGrav<sub>lith</sub> allow for a tripartite morphodynamic (Figures 3b and 10) and hydrographic subdivision (Sections 5.2–5.4) and for the identification of the provenance of clasts, enabling us to constrain the mass wasting and fluvial transport processes leading to the depositional landforms. Moreover, a determination of the range of transport is another step to discriminate between supergene alteration and transport, or in other words, physical–chemical alteration vs. attrition on transport (Figures 14 and 16).

### 5.7. From Economic Geology to Economic Geomorphology

In the majority of cases, mineral deposits crop out at the present-day landscape in a way like that depicted in Figure 9. Their near-surface zone at the interface of the lithosphere–pedosphere–atmosphere, is called gossan, and subjects them to pervasive chemical weathering which results in a wealth of secondary minerals [63,177–182]. There are also so-called hidden mineral deposits devoid of such an outcrop at the present-day surface and as a consequence, this causes mineral exploration fraught with difficulties even if various geophysical and geochemical methods are applied in the target area and combined with geotectonic models [183–188]. In geological settings where supergene or hypogene alteration is identified in the present-day landscape or hidden mineral deposits might be expected, relief categorization, landscape modelling, environment analysis, and landscape chronology can be of aid. (Figures 9c and 14). To find and delineate mineral deposits, a well-structured approach has to be taken. The choice of methods (geological, geomorphological, geochemical, airborne, and ground geophysics) is a function of the size with three different categories aimed at narrowing down the exploration area to the size of an area feasible for mining activities (1.  $\geq 1000 \text{ km}^2$ , 2. 1000 to 10/100  $\text{km}^2$ , and 3. 10 to 1  $\text{km}^2$ ). From the geomorphological point of view, which has a strong say already when dealing with exploration activities in category 1, the  $\text{VeSi}_{\text{val}}$  of landform series takes a keystone position (Figure 14, Table 1), followed by the  $\text{Quant}_{\text{flu}/\text{mas}}$ . The difference between the two hierarchical levels is a matter of the maturity of the landscape, which according to Dill [17] follows a tripartite scheme subdivided into premature, mature, and supermature. The Central European highly eroded mountain belts of Paleozoic age (e.g., Hercynian/Variscan Mountain Ridges) are denominated as mature. The joint action of vertical displacements along a deep-seated lineamentary fault zone, called the FLFZ, during the Cenozoic, however, dictates the maturity level of the geodynamic units in this part of the Central European Variscides (Figures 1–3). It is categorized as premature > mature and this is reflected by the predominance of  $\text{VeSi}_{\text{val}}$  over the  $\text{Quant}_{\text{flu}/\text{mas}}$ . There are also regions of the Central European Variscides where the equation is reversed. Supermature > mature is the characteristic feature of the landscape and consequently the margin between the  $\text{VeSi}_{\text{val}}$  and the  $\text{Quant}_{\text{flu}/\text{mas}}$  is significantly narrowed down to almost nil. This is true for those regions in Central Europe where a pervasive chemical weathering during the Cenozoic and Late Cretaceous resulted in blankets of residual deposits abundant in kaolin, bentonite, supergene Fe-Mn deposits and even Ni laterites [25]. These residual mineral deposits are poorly represented in the study area only by some patchily distributed kaolin nests, attesting to the lack of such pervasive chemical weathering conditions. Older relief generations hosting Fe-Mn duricrusts of the Hunsrück Type point to more pervasive chemical weathering (Figures 14 and 15a). The landforms of all reference LFIs shown in Table 1 can be identified and studied, attesting to relics of a super-mature landscape. However, only the landforms' pre-mature landscape are associated with mineral deposits which were mined for a profit in the past (Figures 9 and 14). The pathway of compositional and numerical geomorphology leading to the discovery of profitable mineral deposits is marked by the LFI sequence  $\text{VeSi}_{\text{val}}$ ,  $\text{IncTal}_{\text{lith}/\text{grad}}$ ,  $\text{VeSi}_{\text{lith}}$ ,  $\text{VaSlAn}_{\text{norm}}$ , and  $\text{HoSi}_{\text{lith}/\text{grad}}$ , which can be fine-tuned using  $\text{QuantGrav}_{\text{situ}/\text{dire}/\text{shar}}$  and amended by  $\text{QuantSan}_{\text{heav}}$ . The area where the concentration of mineral deposits overlaps with the area decisive for shaping the landscape (e.g., river piracy and subsidence) is denominated as the “Geomorphological Hotspot” where endogenous high temperature and exogenous fluvial processes overlap each other (Figure 9c). It is the confluence area of two paleodrainage systems abundant in knickpoints delineating the oldest Neogene fluvial system. The mineral deposits are situated in a triangle controlled by the FLFZ and the SE limb of the major anticline (Figure 1b). At the point of intersection, the pegmatoid field is located (Figures 4f,v,w and 9c). This inti-

mate arrangement of lithologies of an outstanding mineralogical composition and peculiar landforms heralds that endogenous and exogenous processes are not two different entities but rather two different sides of the same coin. The processes which operated under high temperature and/or pressure at depth can result in landforms under near-ambient conditions that are categorized numerically (Figure 9, Table 1). Compositional and numerical geomorphology is used as another tool in extractive/economic geology.

### 6. Conclusions

Compositional and numerical geomorphology is a mixtum compositum to fill in the gap between geomorphology, sedimentary, and applied geology (E&E issue, economic and environmental geology). This numerical and compositional approach has been designed to allow for a comparison between landforms in the fields of genetic and applied geomorphology and provide platforms for airborne, satellite-borne, and ground follow-up geosciences. A sort of graphical conclusion has been designed to highlight what compositional terrain analysis is all about, showing the tripartite subdivision into geomorphology, sedimentology, and sediment petrography, each of which is highlighted by an example from the present reference study (Figure 17).

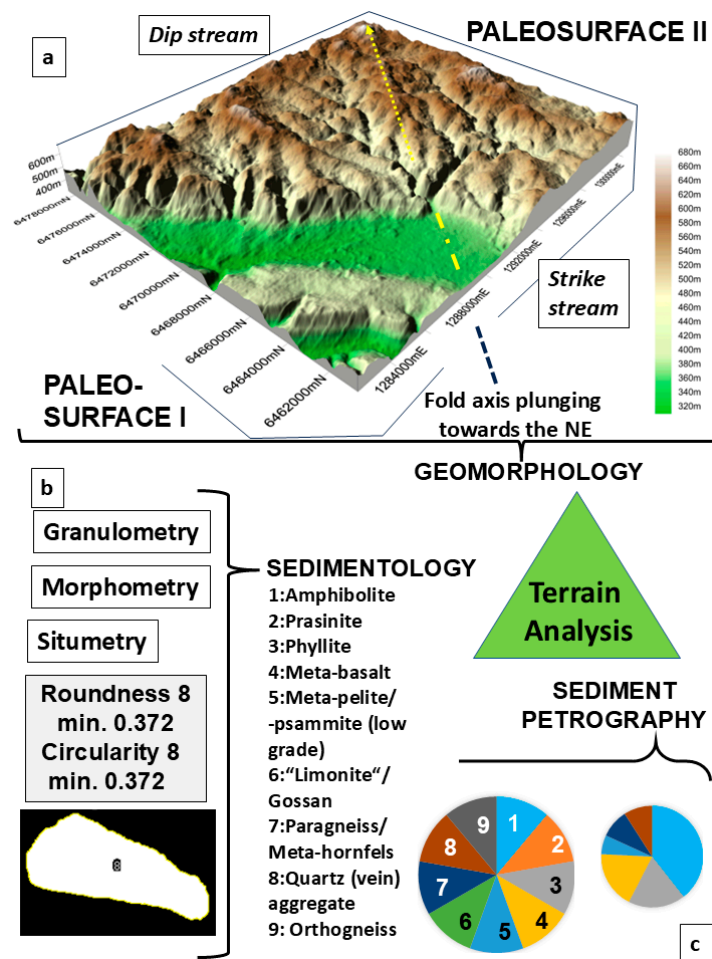


**Figure 17.** The “graphical conclusions” to underscore what the compositional terrain analysis is all about. The tripartite subdivision of the geoscientific disciplines involved: (a) A digital terrain model showing the interrelationship between morphotectonic linear architectural elements (fold axis), and hydrography (strike stream vs. dip stream). (b) The sedimentological GMS technology encompassing granulometry, morphometry, and situmetry. (c) The pie-chart diagram commonly used in sediment petrography to quantify the lithological changes during transport.

The numerical landform indices (LFIs) are coined for the first time in the current paper and the LFIs are used during the mapping of relief generations in the field for genetic purposes and in applied geomorphology. The various groups of LFIs are a function of landscape maturity (pre-mature (1), mature (2), and super-mature (3)) with a string typical of planation processes (3) and another one typical of linear erosion (1). The erosional landform series are subdivided into three categories.

The landscape roughness indices, e.g.,  $VeSi_{val}$  and the  $VaSlAn_{alti}$ , are used for a first order classification of landscapes into relief generations and as environmental markers covering the full set of regional landform series from mountain summits to moderately bosselated to rolling hill landscapes, and when subjected to fine-tuning, from large and shallow valleys to V-shaped acute-angle valleys with or without fluvial erosional terraces, all of which are denominated with numerical LFI.

A second order category of LFIs is devoted to the material properties of the landforms' bedrocks' (1) rock strength ( $VeSi_{lith}$ ) and the (2) bedrock anisotropy ( $VaSlAn_{norm}$ ).

A third group of LFIs describes the hydrography as to its vertical changes by the inclination of the talweg and the different types of knickpoints ( $IncTal_{lith/grad}$ ) and horizontal sinuosity ( $HoSi_{lith/grad}$ ).

The linguistic approach dealing with the erosional landforms is as follows:  $Ve$  = vertical,  $Va$  = Variation,  $Si$  = Sinuosity,  $Sl$  = Slope,  $An$  = angle,  $Inc$  = inclination,  $Tal$  = talweg,  $Ho$  = horizontal,  $Quant$  = quantification,  $San$  = sand, and  $Grav$  = gravel. The subscripts denote the controlling parameters and processes ( $lith$  = lithology,  $grad$  = gradient,  $norm$  = normalized,  $val$  = valley incision, and  $alti$  = altitude).

The depositional landforms are numerically defined in the same way and classified by eight LFIs, which only differ from each other by their subscripts  $Quant_{flu/mas}$ ,  $Quant_{ClaSil}$ ,  $Quant_{San_{ligh}}$ ,  $Quant_{San_{heav}}$ , and  $Quant_{Grav_{lith}}$ , ( $flu/mass$  = ratio fluvial/mass wasting,  $ClaSil$  = clay/silt ratio,  $ligh$  = light minerals sand-sized,  $heav$  = heavy minerals sand-sized, and  $Grav_{lith}$  = lithology gravel-sized). It is a mirror image of the composition of depositional landforms in relation to their grain size, whereas the remaining three numerical indices' depositional landforms are a direct measurement of the hydrodynamic and gravity-driven conditions of the fluvial and mass wasting processes using the granulometry, grain morphology, and sitometry (clast orientation).

The tripartite study area consists of three landform suites which developed during the Cenozoic and pertain to the (1) foreland plains, (2) step-fault plain, and (3) paleoplain. They encompass the entire series of landforms created by mass wasting and fluvial processes and lead to the discovery of new badland landform suites in a metamorphic terrain called a bosselated paleoplain. It developed from a peneplain (17 Ma) through pediplanation between 6 and 4 Ma and was dissected around 1.7 Ma during river piracy, ending up in a series of V-shaped valleys.

**Author Contributions:** Conceptualization, H.G.D.; methodology, A.B. and S.-I.B.; software, A.B., S.-I.B. and H.G.D.; validation, formal analysis, A.B., S.-I.B. and C.K.; investigation, H.G.D. and A.B.; data curation, H.G.D. and C.K.; writing—original draft preparation, H.G.D.; writing—review and editing, H.G.D.; visualization, S.-I.B., H.G.D. and A.B.; supervision, H.G.D. All authors have read and agreed to the published version of the manuscript.

**Funding:** This research received no external funding.

**Data Availability Statement:** Data are made available upon request.

**Acknowledgments:** We thank the two anonymous reviewers for their constructive comments and the academic editor for the handling of our paper for GEOSCIENCES.

**Conflicts of Interest:** The authors declare no conflict of interest.

## References

1. Beechie, T.J.; Liermann, M.; Pollock, M.M.; Baker, S.; Davies, J. Channel pattern and river-floodplain dynamics in forested mountain river systems. *Geomorphology* **2006**, *78*, 124–141. [\[CrossRef\]](#)
2. Charlton, R. *Fundamentals of Fluvial Geomorphology*; Routledge: Abingdon, UK, 2014; p. 214.
3. Karatson, D.; Sztano, O.; Telbisz, T. Preferred Clast Orientation in Volcaniclastic Mass-Flow Deposits: Application of a New Photo-Statistical Method. *J. Sediment. Res.* **2002**, *72*, 823–835. [\[CrossRef\]](#)
4. McKnight, T.L.; Hess, D. The Fluvial Processes. In *Physical Geography: A Landscape Appreciation*; Prentice Hall: Rutherford, NJ, USA, 2005; p. 629.
5. Miall, A.D. *The Geology of Fluvial Deposits: Sedimentary Petroleum Geology*; Springer: Berlin/Heidelberg, Germany, 1996; p. 582.
6. Mills, H.H. Three-dimensional clast orientation in glacial and mass-movement sediments: A compilation and preliminary analysis. *USGS Open-File Rep.* **1990**, *90*, 71. [\[CrossRef\]](#)
7. Nichols, G. *Sedimentology and Stratigraphy*; Blackwell Publishing: Hoboken, NJ, USA, 2009; p. 432.
8. Scheffers, A.M.; May, S.M.; Kelletat, D.H. Forms by Flowing Water (Fluvial Features). In *Landforms of the World with Google Earth*; Springer: Amsterdam, The Netherlands, 2015; pp. 183–244.
9. Andreani, L.; Stanek, K.; Gloaguen, R.; Krentz, O.; Domínguez-González, L. DEM-Based Analysis of Interactions between Tectonics and Landscapes in the Ore Mountains and Eger Rift (East Germany and NW Czech Republic). *Remote Sens.* **2014**, *6*, 7971–8001. [\[CrossRef\]](#)
10. Bonachea, J.; Bruschi, V.M.; Remondo, J.; González-Díez, A.; Salas, L.; Bertens, J.; Cendrero, A.; Otero, C.; Giusti, C.; Fabbri, A.; et al. An approach for quantifying geomorphological impacts for EIA of transportation infrastructures: A case study in northern Spain. *Geomorphology* **2005**, *66*, 95–117. [\[CrossRef\]](#)
11. Capolongo, D.; Giachetta, E.; Refice, A. Numerical framework for geomorphological experiments. *Geogr. Fis. Dinam. Quat.* **2011**, *34*, 75–80.
12. Doornkamp, J.C.; King, C.A.M. *Numerical Analysis in Geomorphology*; Hodder & Stoughton Educational: London, UK, 1971; p. 380.
13. Drăguț, L.; Blaschke, T. Automated classification of landform elements using object-based image analysis. *Geomorphology* **2006**, *81*, 330–344. [\[CrossRef\]](#)
14. Gao, L.; He, C.; Rao, G.; Yang, C.-J.; Yuan, X.; Lai, J.; Tang, P.; Wu, L. Numerical examination of the geomorphic indicators for lateral fold growth. *Geomorphology* **2023**, *432*, 108702. [\[CrossRef\]](#)
15. MacMillan, R.A.; Shary, P.A. Landforms and landform elements in geomorphometry. In *Advances in Digital Terrain Analysis*; Zhou, Q., Lees, B.G., Tang, G., Eds.; Springer: Berlin/Heidelberg, Germany, 2009.
16. Minár, J.; Evans, I.S. Elementary forms for land surface segmentation: The theoretical basis of terrain analysis and geomorphological mapping. *Geomorphology* **2008**, *95*, 236–259. [\[CrossRef\]](#)
17. Dill, H.G. An overview of the pegmatitic landscape from the pole to the equator—Applied geomorphology and ore guides. *Ore Geol. Rev.* **2017**, *91*, 795–823. [\[CrossRef\]](#)
18. Dill, H.G.; Buzatu, A.; Balaban, S.-I. Coastal morphology and heavy mineral accumulation in an upper-macrotidal environment—A geological-mineralogical approach from source to trap site in a natural placer laboratory (Channel Islands, Great Britain). *Ore Geol. Rev.* **2021**, *138*, 104311. [\[CrossRef\]](#)
19. Dill, H.G.; Buzatu, A.; Balaban, S.-I.; Rösenberg, K.A. A mineralogical-geomorphological terrain analysis of hotspot volcanic islands—The missing link between carbonatite- and pegmatite Nb-F-Zr-Li-Be-bearing REE deposits and new tools for their exploration (Canary Islands Archipelago, Spain). *Ore Geol. Rev.* **2023**, *163*, 105702. [\[CrossRef\]](#)
20. Sillitoe, R.H. Epithermal paleosurfaces. *Miner. Depos.* **2015**, *50*, 767–793. [\[CrossRef\]](#)
21. Sillitoe, R.H.; Bonham, H.F. Volcanic landforms and ore deposits. *Econ. Geol.* **1984**, *79*, 1286–1298. [\[CrossRef\]](#)
22. Sillitoe, R.H.; Hedenquist, J.W. Linkages between Volcanotectonic Settings, Ore-Fluid Compositions, and Epithermal Precious Metal Deposits. In *Volcanic, Geothermal, and Ore-Forming Fluids: Rulers and Witnesses of Processes within the Earth*; Simmons, S.F., Graham, I., Eds.; Society of Economic Geologists: Littleton, CO, USA, 2005; Volume 10, pp. 315–343.
23. Dill, H.G.; Balaban, S.-I.; Füssl, M.; Pöllmann, H.; Buzatu, A. Morphostratigraphy of landform series from the Late Cretaceous to the Quaternary: The “3 + 1” model of the quadripartite watershed system at the NW edge of the Bohemian Massif. *Geomorphology* **2022**, *419*, 108489. [\[CrossRef\]](#)
24. Dill, H.G. The “chessboard” classification scheme of mineral deposits: Mineralogy and geology from aluminum to zirconium. *Earth-Sci. Rev.* **2010**, *100*, 1–420. [\[CrossRef\]](#)
25. Dill, H.G.; Sachsenhofer, R.F.; Grecula, P.; Sasvári, T.; Palinkaš, L.; Borojević-Šošarić, S.; Strmić-Palinkaš, S.; Prochaska, W.; Garuti, G.; Zaccarini, F. Fossil fuels, ore—And industrial minerals. In *Geology of Central Europe*; McCann, T., Ed.; Geological Society Publishing House: Bath, UK, 2008; pp. 1341–1449.
26. Emmert, U.; Horstig, G.V.; Stettner, G. *Geologische Übersichtskarte 1:200000 CC 6334 Bayreuth*; BGR: Hannover, Germany, 1981.

27. Bachmann, G.H.; Geluk, M.C.; Warrington, G.; Becker-Roman, A.; Beutler, G.; Hagdorn, H.; Hounslow, M.W.; Nitsch, E.; Röhling, H.-G.; Simon, T.; et al. Triassic. In *Petroleum Geological Atlas of the Southern Permian Basin Area*; Doornenbal, J.C., Stevenson, A.G., Eds.; EAGE Publications b.v.: Houten, The Netherlands, 2010; pp. 149–173.
28. Berger, G. Die miozäne Flora und Fauna (MN 5) der historischen Fossil-Lagerstätte Georgensgmünd (Mfr.) unter Berücksichtigung der Ablagerungen des Urmaintals zwischen Roth und Treuchtlingen. *Abh. Nat. Hist. Ges. Nürnberg* **2010**, *46*, 1–191.
29. Dill, H.G.; Buzatu, A.; Balaban, S.J.; Ufer, K.; Techmer, A.; Schedlinsky, W.; Füssl, M. The transition of very coarse-grained meandering to straight fluvial drainage systems in a tectonized foreland-basement landscape during the Holocene (SE Germany)—A joint geomorphological-geological study. *Geomorphology* **2020**, *370*, 107364. [[CrossRef](#)]
30. Hüttner, R.; Schmidt-Kaler, H. *Wanderungen in der Erdgeschichte (10): Meteoritenkrater Nördlinger Ries*; Verlag Dr. Friedrich Pfeil: München, Germany, 2003; p. 144.
31. McCann, T. *The Geology of Central Europe Volume 2: Mesozoic and Cenozoic*; The Geological Society of London: London, UK, 2008; p. 700.
32. Ring, U.; Bolhar, R. Tilting, uplift, volcanism and disintegration of the South German block. *Tectonophysics* **2020**, *795*, 228611. [[CrossRef](#)]
33. Schirmer, W. Die Geschichte von Moenodanuvius und Main in Oberfranken. *Streifzüge Durch Frank* **2010**, *1*, 9–24.
34. Voigt, S.; Wagreich, M.; Surlyk, F.; Walaszczyk, I.; Uličný, D.; Čech, S.; Voigt, T.; Wiese, F.; Wilmsen, M.; Niebuhr, B. Cretaceous. In *Geology of Central Europe*; McCann, T., Ed.; Geological Society of London: London, UK, 2008; pp. 923–997.
35. Emmert, U.; von Horstig, G.; Weinelt, W. *Geologische Karte von Bayern 1:25000 Erläuterung Blatt 5835 Stadtsteinach*; Geologisches Landesamt: München, Germany, 1960; p. 279.
36. Emmert, U.; Weinelt, W. *Geologische Karte von Bayern 1:25000 Erläuterung Blatt 5935 Marktschorgast*; Geologisches Landesamt: München, Germany, 1962; p. 286.
37. Dallmeyer, R.D.; Franke, W.; Weber, K. *Pre-Permian Geology of Central and Eastern Europe*; Springer: Berlin/Heidelberg, Germany, 1995; p. 604. [[CrossRef](#)]
38. McCann, T. *The Geology of Central Europe: Volume 1: Precambrian and Palaeozoic*; The Geological Society of London: London, UK, 2008; p. 748.
39. Stettner, G. *Geologische Karte von Bayern 1:25000 Erläuterung Blatt 5836 Münchberg*; Geologisches Landesamt: München, Germany, 1960; p. 163.
40. Stettner, G. *Geologische Karte von Bayern 1:25000 Erläuterung Blatt 5936 Bad Berneck*; Geologisches Landesamt: München, Germany, 1977; p. 225.
41. Söllner, P.; Köhler, H.; Müller-Sohnius, D. Rb/Sr Altersbestimmungen an Gesteinen der Münchberger Gneismasse (M.N.); NE-Bayern; Teil 1 Gesamtgesteinsdatierungen. *Neues Jahrb. Mineral. Abh.* **1981**, *141*, 90–112.
42. Gebauer, D.; Grünenfelder, M. UPb zircon and RbSr mineral dating of eclogites and their country rocks. Example: Münchberg Gneiss Massif, Northeast Bavaria. *Earth Planet. Sci. Lett.* **1979**, *42*, 35–44. [[CrossRef](#)]
43. Hornung, J.; Aigner, T. Reservoir Architecture in a Terminal Alluvial Plain: An Outcrop Analogue Study (Upper Triassic, Southern Germany) Part 1: Sedimentology and Petrophysics. *J. Pet. Geol.* **2002**, *25*, 3–30. [[CrossRef](#)]
44. Thauer, W. Morphologische Studien im Frankenwald und im Frankenwaldvorland. *Mitteilungen Fränkischen Geogr. Ges.* **1954**, *1*, 1–232.
45. von Eynatten, H.; Kley, J.; Dunkl, I.; Hoffmann, V.-E.; Simon, A. Late Cretaceous to Paleogene exhumation in central Europe—Localized inversion vs. large-scale domal uplift. *Solid Earth* **2021**, *12*, 935–958. [[CrossRef](#)]
46. Balatka, B.; Kalvoda, J.; Steklá, T.; Štěpančíková, P. Morphostratigraphy of river terraces in the Eger valley (Czechia) focused on the Smrčiny Mountains, the Chebská pánev Basin and the Sokolovská pánev Basin. *AUC Geogr.* **2019**, *54*, 240–250. [[CrossRef](#)]
47. Borger, H. Mikromorphologie und Paläoenvironment: Die Mineralverwitterung als Zeugnis der kretazisch-tertiären Umwelt in Süddeutschland. *Relief Boden Paläoklima* **2000**, *15*, 1–243.
48. Demek, J. Etch plain, rock pediments and morphostructural analysis of the Bohemian Massif (Czech Republic). In *Czech Geography at the Dawn of the Millenium*; Drbohlav, D., Kalvoda, J., VoüenĚlek, V., Eds.; Palacky University: Olomouc, Czechia, 2004; pp. 69–81.
49. Dill, H.G.; Buzatu, A.; Balaban, S.-I. Straight to Low-Sinuosity Drainage Systems in a Variscan-Type Orogen—Constraints from Tectonics, Lithology and Climate. *Minerals* **2021**, *11*, 933. [[CrossRef](#)]
50. Grygar, T.M.; Elznicová, J.; Sipos, G.; Kiss, T. Terraces of the Ohře River in Žatec Area, Czech Republic: When Models of Holocene Fluvial Development Are Not Sufficient. *Geosciences* **2021**, *11*, 210. [[CrossRef](#)]
51. Káňšner, A.; Stanek, K.P.; Lapp, M. Post-Variscan tectonic and landscape evolution of the Elbe Fault Zone and the Lusatian Block based on apatite fission-track data and geomorphologic constraints. *Geomorphology* **2020**, *355*, 106860. [[CrossRef](#)]
52. Migoń, P. Tertiary etch surfaces in the Sudetes Mountains, SW Poland: A contribution to the pre Quaternary morphology of Central Europe. In *Palaeosurfaces: Recognition, Reconstruction and Palaeoenvironmental Interpretation*; Widdowson, M., Ed.; Geological Society: London, UK, 1997; Volume 120, pp. 187–202.

53. Dill, H.G.; Gerdes, A.; Weber, B. Age and mineralogy of supergene uranium minerals—Tools to unravel geomorphological and palaeohydrological processes in granitic terrains (Bohemian Massif, SE Germany). *Geomorphology* **2010**, *117*, 44–65. [[CrossRef](#)]
54. Bonow, J.M.; Lidmar-Bergström, K.; Japsen, P. Palaeosurfaces in central West Greenland as reference for identification of tectonic movements and estimation of erosion. *Glob. Planet. Change* **2006**, *50*, 161–183. [[CrossRef](#)]
55. Widdowson, M. The geomorphological and geological importance of palaeosurfaces. In *Palaeosurfaces: Recognition, Reconstruction and Palaeoenvironmental Interpretation*; Widdowson, M., Ed.; The Geological Society: London, UK, 1997; pp. 1–12.
56. Friedman, G.M.; Sanders, J.E.; Kopaska-Merkel, D.C. *Principles of Sedimentary Deposits*; MacMillan Publishing Company: New York, NY, USA, 1992; p. 717.
57. Anderson, S.P.; Blum, J.; Brantley, S.L.; Chadwick, O.; Chorover, J.; Derry, L.A.; Drever, J.I.; Hering, J.G.; Kirchner, J.W.; Kump, L.R.; et al. Proposed initiative would study Earth’s weathering engine. *Eos Trans. Am. Geophys. Union* **2004**, *85*, 265–269. [[CrossRef](#)]
58. Chardon, D.; Grimaud, J.-L.; Beauvais, A.; Bamba, O. West African lateritic pediments: Landform-regolith evolution processes and mineral exploration pitfalls. *Earth-Sci. Rev.* **2018**, *179*, 124–146. [[CrossRef](#)]
59. Goudie, A.S.; Viles, H. Weathering processes and forms. In *The History of the Study of Landforms or the Development of Geomorphology*; Burt, T.P., Chorley, R.J., Brunsdon, D., Cox, N.J., Goudie, A.S., Eds.; Geological Society: London, UK, 2008; pp. 129–164.
60. Migoń, P. *Geomorphological Landscapes of the World*; Springer: Dordrecht, The Netherlands, 2009; p. 387.
61. Paasche, Ø.; Strømsøe, J.R.; Dahl, S.O.; Linge, H. Weathering characteristics of arctic islands in northern Norway. *Geomorphology* **2006**, *82*, 430–452. [[CrossRef](#)]
62. Strømsøe, J.R.; Paasche, Ø. Weathering patterns in high-latitude regolith. *J. Geophys. Res.* **2011**, *116*. [[CrossRef](#)]
63. Taylor, G.; Eggleton, R.A. *Regolith Geology and Geomorphology*; John Wiley & Sons: Hoboken, NJ, USA, 2009; p. 375.
64. White, A.F.; Blum, A.E.; Schulz, M.S.; Huntington, T.G.; Peters, N.E.; Stonestrom, D.A. Chemical weathering of the Panola Granite: Solute and regolith elemental fluxes and the dissolution rate of biotite. In *Water–Rock Interaction, Ore Deposits, and Environmental Geochemistry: A Tribute to David, A. Crerar*; Hellmann, R., Wood, S.A., Eds.; The Geochemical Society: St. Louis, MO, USA, 2002; pp. 37–59.
65. Zambell, C.B.; Adams, J.M.; Goring, M.L.; Schwartzman, D.W. Effect of lichen colonization on chemical weathering of hornblende granite as estimated by aqueous elemental flux. *Chem. Geol.* **2012**, *291*, 166–174. [[CrossRef](#)]
66. Bullard, J.E. Arid geomorphology. *Prog. Phys. Geogr. Earth Environ.* **2004**, *28*, 130–144. [[CrossRef](#)]
67. Gutiérrez, F.; Gutiérrez, M. *Landforms of the Earth*; Springer: New York, NY, USA, 2016; p. 284.
68. Koster, E.A. *The Physical Geography of Western Europe (Oxford Regional Environments)*; Oxford University Press: Oxford, UK, 2005; p. 438.
69. Summerfield, M.A. *Global Geomorphology. An Introduction to the Study of Landforms*; John Wiley: New York, NY, USA, 1991; p. 537.
70. Robertson, S. *BGS Rock Classification Scheme—Classification of Metamorphic Rocks*; British geological Survey research Report RR 99-02; British Geological Survey: Lubbock, TX, USA, 1999; p. 24.
71. Bremer, H. Relief generation. In *Encyclopedia of Geomorphology*; Goudie, A.S., Ed.; Routledge: London, UK, 2004; pp. 842–843.
72. Hargitai, H.; Kereszturi, Á. *Encyclopedia of Planetary Landforms*; Springer: New York, NY, USA, 2015.
73. Fischer-Cripps, A.C. *Introduction to Contact Mechanics*; Springer: New York, NY, USA, 2007.
74. Gent, M.; Menendez, M.; Torano, J.; Torno, S. A correlation between Vickers Hardness indentation values and the Bond Work Index for the grinding of brittle minerals. *Powder Technol.* **2012**, *224*, 217–222. [[CrossRef](#)]
75. Kharchenko, V.V.; Katok, O.A.; Kravchuk, R.V.; Sereda, A.V.; Shvets, V.P. Analysis of the methods for determination of strength characteristics of NPP main equipment metal from the results of hardness and indentation measurements. *Procedia Struct. Integr.* **2022**, *36*, 59–65. [[CrossRef](#)]
76. Nix, W.D.; Gao, H. Indentation size effects in crystalline materials: A law for strain gradient plasticity. *J. Mech. Phys. Solids* **1998**, *46*, 411–425. [[CrossRef](#)]
77. Polanco, J.D.; Jacanamejoy-Jamioy, C.; Mambuscay, C.L.; Piamba, J.F.; Forero, M.G. Automatic Method for Vickers Hardness Estimation by Image Processing. *J Imaging* **2022**, *9*, 8. [[CrossRef](#)]
78. Goudie, A.S. The Schmidt Hammer and Related Devices in Geomorphological Research. In *Treatise on Geomorphology*; Shroder, J., Switzer, A.D., Kennedy, D.M., Eds.; Academic Press: San Diego, CA, USA, 2013; Volume 14, pp. 338–345.
79. Matthews, J.A.; Winkler, S. Schmidt-hammer exposure-age dating: A review of principles and practice. *Earth-Sci. Rev.* **2022**, *230*, 104038. [[CrossRef](#)]
80. Tomkins, M.D.; Dortch, J.M.; Hughes, P.D. Schmidt Hammer exposure dating (SHED): Establishment and implications for the retreat of the last British Ice Sheet. *Quat. Geochronol.* **2016**, *33*, 46–60. [[CrossRef](#)]
81. Viles, H.; Goudie, A.; Grab, S.; Lalley, J. The use of the Schmidt Hammer and Equotip for rock hardness assessment in geomorphology and heritage science: A comparative analysis. *Earth Surf. Process. Landf.* **2011**, *36*, 320–333. [[CrossRef](#)]
82. Crosby, B.T.; Whipple, K.X. Knickpoint initiation and distribution within fluvial networks: 236 waterfalls in the Waipaoa River, North Island, New Zealand. *Geomorphology* **2006**, *82*, 16–38. [[CrossRef](#)]

83. Hanks, T.C.; Webb, R.H. Effects of tributary debris on the longitudinal profile of the Colorado River in Grand Canyon. *J. Geophys. Res. Earth Surf.* **2006**, *111*. [[CrossRef](#)]
84. Church, M. Geomorphic thresholds in riverine landscapes. *Freshw. Biol.* **2002**, *47*, 541–557. [[CrossRef](#)]
85. Urban, H.; Vache, R. Die Kupfererzlagertstätten von Wirsberg (Oberfranken) im Lichte neuer Aufschlüsse. *Geol. Bavarica* **1972**, *65*, 74–106.
86. Knighton, D.A. *Fluvial Forms and Processes: New Perspective*; Arnold: London, UK, 1998; p. 400.
87. Robert, A. *River Processes: An Introduction to Fluvial Dynamics*; Routledge: Abingdon, UK, 2003; p. 238.
88. Schumm, S.A. Sinuosity of Alluvial Rivers on the Great Plains. *Geol. Soc. Am. Bull.* **1963**, *74*, 1089. [[CrossRef](#)]
89. Ahnert, F.O. *Einführung in Die Geomorphologie*; UTB GmbH: Baden-Württemberg, Germany, 2015; p. 458.
90. Ghosh, S.; Mistri, B. Hydrogeomorphic significance of sinuosity index in relation to river instability: A case study of Damodar River, West Bengal, India. *Int. J. Adv. Earth Sci.* **2012**, *1*, 49–57.
91. Horacio, J. *River Sinuosity Index: Geomorphological Characterization*; CIREF and Wetlands International European Association: Santiago de Compostela, Spain, 2014; p. 6.
92. Lazarus, E.D.; Constantine, J.A. Generic theory for channel sinuosity. *Proc Natl Acad Sci USA* **2013**, *110*, 8447–8452. [[CrossRef](#)]
93. Turowski, J.M. Alluvial cover controlling the width, slope and sinuosity of bedrock channels. *Earth Surf. Dyn.* **2018**, *6*, 29–48. [[CrossRef](#)]
94. Ollier, C.; Payne, C. *Regolith, Soils and Landforms*; John Wiley: Chichester, UK, 1996; p. 326.
95. Scott, K.M.; Payne, C. *Regolith Science*; Springer: New York, NY, USA, 2009; p. 472.
96. Udden, J.A. Mechanical composition of clastic sediments. *Geol. Soc. Am. Bull.* **1914**, *25*, 655–744. [[CrossRef](#)]
97. Wentworth, C.K. A scale of grade and class terms for clastic sediments. *J. Geol.* **1922**, *30*, 377–392. [[CrossRef](#)]
98. Dill, H.G. A geological and mineralogical review of clay mineral deposits and phyllosilicate ore guides in Central Europe—A function of geodynamics and climate change. *Ore Geol. Rev.* **2020**, *119*, 103304. [[CrossRef](#)]
99. Bergmann, J.; Friedel, P.; Kleeberg, R. BGMN—A new fundamental parameters based Rietveld program for laboratory X-ray sources, its use in quantitative analysis and structure investigations. *CPD Newsl.* **1998**, *20*, 5–8.
100. Chardon, E.S.; Livens, F.R.; Vaughan, D.J. Reactions of feldspar surfaces with aqueous solutions. *Earth-Sci. Rev.* **2006**, *78*, 1–26. [[CrossRef](#)]
101. Dultz, S. Effects of parent material and weathering on feldspar content in different particle size fractions from forest soils in NW Germany. *Geoderma* **2002**, *106*, 63–81. [[CrossRef](#)]
102. White, A.F.; Bullen, T.D.; Schulz, M.S.; Blum, A.E.; Huntington, T.G.; Peters, N.E. Differential rates of feldspar weathering in granitic regoliths. *Geochim. Cosmochim. Acta* **2001**, *65*, 847–869. [[CrossRef](#)]
103. Yuan, G.; Cao, Y.; Schulz, H.-M.; Hao, F.; Gluyas, J.; Liu, K.; Yang, T.; Wang, Y.; Xi, K.; Li, F. A review of feldspar alteration and its geological significance in sedimentary basins: From shallow aquifers to deep hydrocarbon reservoirs. *Earth-Sci. Rev.* **2019**, *191*, 114–140. [[CrossRef](#)]
104. Dill, H.G.; Klosa, D. Heavy mineral-based provenance analysis of Mesozoic continental-marine sediments at the western edge of the Bohemian Massif, SE Germany: With special reference to Fe–Ti minerals and the crystal morphology of heavy minerals. *Int. J. Earth Sci.* **2010**, *100*, 1497–1513. [[CrossRef](#)]
105. Joshi, K.B.; Banerji, U.S.; Dubey, C.P.; Oliveira, E.P. Heavy minerals in provenance studies: An overview. *Arab. J. Geosci.* **2021**, *14*. [[CrossRef](#)]
106. Makuluni, P.; Kirkland, C.L.; Barham, M.; Tyrrell, S. Zircon grain shape holds provenance information: A case study from southwestern Australia. *Geol. J.* **2018**, *54*, 1279–1293. [[CrossRef](#)]
107. Morton, A.; Chenery, S. Detrital Rutile Geochemistry and Thermometry as Guides to Provenance of Jurassic-Paleocene Sandstones of the Norwegian Sea. *J. Sediment. Res.* **2009**, *79*, 540–553. [[CrossRef](#)]
108. Barudžija, U.; Velić, J.; Malvić, T.; Trenc, N.; Matovinović Božinović, N. Morphometric Characteristics, Shapes and Provenance of Holocene Pebbles from the Sava River Gravels (Zagreb, Croatia). *Geosciences* **2020**, *10*, 92. [[CrossRef](#)]
109. Daxue, X. Magnetism and provenance analysis of high position gravel layer in the middle reaches of Yangtze River. *J. Jilin Univ. (Earth Sci. Ed.)* **2014**, *44*, 1669–1677.
110. James, D.E.; DeVaughn, A.M.; Marsaglia, K.M. Sand and gravel provenance in the Waipaoa River system: Sedimentary recycling in an actively deforming forearc basin, North Island, New Zealand. In *Sedimentary Provenance and Petrogenesis: Perspectives from Petrography and Geochemistry*; Arribas, J., Johnsson, M.J., Critelli, S., Eds.; Geological Society of America: Boulder, CO, USA, 2007. [[CrossRef](#)]
111. Koning, D.J.; Jochems, A.P.; Morgan, G.S.; Lueth, V.W.; Peters, L. Stratigraphy, gravel provenance, and age of early Rio Grande deposits exposed 1–2 km northwest of downtown Truth or Consequences, New Mexico. In *Guidebook 67—Geology of the Belen Area*; Frey, B.A., Karlstrom, K.E., Lucas, S.G., Williams, S., Ziegler, K., McLemore, V., Ulmer-Scholle, D.S., Eds.; New Mexico Geological Society 67th Annual Fall Field Conference Guidebook; New Mexico Geological Society: Socorro, NM, USA, 2016; pp. 459–478.

112. McClenaghan, M.B.; Thorleifson, L.H.; DiLabio, R.N.W. Till geochemical and indicator mineral methods in mineral exploration. *Ore Geol. Rev.* **2000**, *16*, 145–166. [[CrossRef](#)]
113. Francou, B. Stratification mechanisms in slope deposits in high subequatorial mountains. *Permafrost Periglacial Process* **1990**, *1*, 249–263. [[CrossRef](#)]
114. Millar, S.W.S.; Nelson, F.E. Sampling-surface orientation and clast macrofabric in periglacial colluvium. *Earth Surf. Process. Landf.* **2001**, *26*, 523–529. [[CrossRef](#)]
115. Mills, H.H. Clast Orientation in Mount St. Helens Debris-Flow Deposits, North Fork Toutle River, Washington. *SEPM J. Sediment. Res.* **1984**, *54*. [[CrossRef](#)]
116. Nieuwenhuijzen, M.E.; van Steijn, H. Alpine debris flows and their sedimentary properties. A case study from the French Alps. *Permafrost Periglacial Process* **1990**, *1*, 111–128. [[CrossRef](#)]
117. Bari, Z.; Rajib, M.; Majid, M.; Sayem, H. Textural analyses of the bar sands of the Gorai River: Implications for depositional phase and environment. *Jahangirnagar Univ. Environ. Bull.* **2012**, *1*, 25–34. [[CrossRef](#)]
118. Liro, M. Differences in the reconstructions of the depositional environment of overbank sediments performed using the C/M diagram and cumulative curve analyses. *Landf. Anal.* **2015**, *29*, 35–40. [[CrossRef](#)]
119. Passega, R.; Byramjee, R. Grain-Size Image of Clastic Deposits. *Sedimentology* **1969**, *13*, 233–252. [[CrossRef](#)]
120. Visher, G.S. Grain Size Distributions and Depositional Processes. *SEPM J. Sediment. Res.* **1969**, *39*. [[CrossRef](#)]
121. Guerit, L.; Barrier, L.; Liu, Y.; Narteau, C.; Lajeunesse, E.; Gayer, E.; Métivier, F. Uniform grain-size distribution in the active layer of a shallow, gravel-bedded, braided river (the Urumqi River, China) and implications for paleo-hydrology. *Earth Surf. Dyn.* **2018**, *6*, 1011–1021. [[CrossRef](#)]
122. Janaka, G.H.A.; Kumara, J.; Hayano, K.; Ogiwara, K. Image Analysis Techniques on Evaluation of Particle Size Distribution of Gravel. *Int. J. GEOMATE* **2012**, *3*, 290–297.
123. Khan, U.A.; Valentino, R. Investigating the Granulometric Distribution of Fluvial Sediments through the Hybrid Technique: Case Study of the Baganza River (Italy). *Water* **2022**, *14*, 1511. [[CrossRef](#)]
124. Blott, S.J.; Pye, K. Particle shape: A review and new methods of characterization and classification. *Sedimentology* **2007**, *55*, 31–63. [[CrossRef](#)]
125. Illenberger, W.K. Pebble Shape (and Size!). *SEPM J. Sediment. Res.* **1991**, *61*. [[CrossRef](#)]
126. Powers, M.C. Comparison Chart for Estimating Roundness and Sphericity. Amer. Geol. Inst., Data Sheet 18.1. of terrain analysis and geomorphological mapping. *Geomorphology* **1982**, *95*, 236–259.
127. Matsumoto, N.; Ogawa, M.; Takayasu, K.; Hirayama, M.; Miura, T.; Shiozawa, K.; Abe, M.; Nakagawara, H.; Moriyama, M.; Udagawa, S. Quantitative sonographic image analysis for hepatic nodules: A pilot study. *J. Med. Ultrason (2001)* **2015**, *42*, 505–512. [[CrossRef](#)] [[PubMed](#)]
128. Owczarek, P. The variation in clasts orientation in mid-mountain river channels under the influence of coarse-grained regolith supply, Polish Flysch Carpathians. *Stud. Geomorphol. Carpato-Balc.* **2003**, *37*, 97–110.
129. Puig, J.M.; Cabello, P.; Howell, J.; Arbués, P. Three-dimensional characterisation of sedimentary heterogeneity and its impact on subsurface flow behaviour through the braided-to-meandering fluvial deposits of the Castissent Formation (late Ypresian, Tremp-Graus Basin, Spain). *Mar. Pet. Geol.* **2019**, *103*, 661–680. [[CrossRef](#)]
130. Reineck, H.E.; Singh, I.B. *Depositional Sedimentary Environments: With Reference to Terrigenous Clastics*; Springer Science Business Media: New York, NY, USA, 2012; p. 551.
131. Schlunegger, F.; Gafalakis, P. Clast imbrication in coarse-grained mountain streams and stratigraphic archives as indicator of deposition in upper flow regime conditions. *Earth Surf. Dyn.* **2018**, *6*, 743–761. [[CrossRef](#)]
132. Bonnet, C.; Malavieille, J.; Mosar, J. Interactions between tectonics, erosion, and sedimentation during the recent evolution of the Alpine orogen: Analogue modeling insights. *Tectonics* **2007**, *26*. [[CrossRef](#)]
133. Cullum, C.; Rogers, K. *A Framework for the Classification of Drainage Networks in Savanna Landscapes*; Water Research Commission Report No. TT 498/11; Water Research Commission: Pretoria, South Africa, 2011; p. 116.
134. Demoulin, A.; Schiattarella, M.; Pedersen, V.K. Geomorphic response to active tectonics: Numerical and field-based approaches. *Earth Surf. Process. Landf.* **2018**, *43*, 2666–2668. [[CrossRef](#)]
135. Wilson, J.P.; Bishop, M.P. Geomorphometry. In *Treatise on Geomorphology*, Shroder, J., Bishop, M.P., Eds.; Academic Press: San Diego, CA, USA, 2013; Volume 3, pp. 162–186.
136. Xiong, L.; Li, S.; Tang, G.; Strobl, J. Geomorphometry and terrain analysis: Data, methods, platforms and applications. *Earth-Sci. Rev.* **2022**, *233*, 104191. [[CrossRef](#)]
137. Ebert, K.; Hall, A.M.; Hättstrand, C. Pre-glacial landforms on a glaciated shield: The inselberg plains of northern Sweden. *Nor. J. Geol.* **2012**, *92*, 1–17.
138. Evenstar, L.A.; Mather, A.E.; Hartley, A.J.; Stuart, F.M.; Sparks, R.S.J.; Cooper, F.J. Geomorphology on geologic timescales: Evolution of the late Cenozoic Pacific paleosurface in Northern Chile and Southern Peru. *Earth-Sci. Rev.* **2017**, *171*, 1–27. [[CrossRef](#)]

139. Godard, A.; Lagasquie, J.-J. *Basement Regions*; Springer: New York, NY, USA, 2012; p. 324.
140. Green, P.F.; Lidmar-Bergström, K.; Japsen, P.; Bonow, J.M.; Chalmers, J.A. Stratigraphic landscape analysis, thermochronology and the episodic development of elevated, passive continental margins. *Geol. Surv. Den. Greenl. Bull.* **2013**, *30*, 1–150. [[CrossRef](#)]
141. King, L.C. Canons of landscape evolution. *Bull. Geol. Soc. Am.* **1953**, *64*, 721–751. [[CrossRef](#)]
142. Marques, K.P.P.; dos Santos, M.; Peifer, D.; da Silva, C.L.; Vidal-Torrado, P. Transient and relict landforms in a lithologically heterogeneous post-orogenic landscape in the intertropical belt (Alto Paranaíba region, Brazil). *Geomorphology* **2021**, *391*, 107892. [[CrossRef](#)]
143. Penck, W. *Die Morphologische Analyse: Ein Kapitel der Physikalischen Geologie 2, Geographische Abhandlungen*; Engelhorn: Stuttgart, Germany, 1924; p. 283.
144. Twidale, C.R. Bornhardts and associated fracture patterns. *Rev. Asoc. Geol. Argent.* **2007**, *62*, 139–153.
145. Twidale, C.R.; Vital-Romani, J.R. *Landforms and Geology of the Granite Terrains*; Balkema: Leiden, The Netherlands, 2005; p. 344.
146. Wayland, E.J. Peneplains and Some Erosional Landforms. *Geol. Surv. Uganda. Ann. Rep. Bull.* **1934**, *1*, 77–79.
147. Bonnet, N.J.; Beauvais, A.; Arnaud, N.; Chardon, D.; Jayananda, M. First <sup>40</sup>Ar/<sup>39</sup>Ar dating of intense Late Palaeogene lateritic weathering in Peninsular India. *Earth Planet. Sci. Lett.* **2014**, *386*, 126–137. [[CrossRef](#)]
148. De Putter, T.; Ruffet, G. Supergene manganese ore records 75 Myr-long Campanian to Pleistocene geodynamic evolution and weathering history of the Central African Great Lakes Region—Tectonics drives, climate assists. *Gondwana Res.* **2020**, *83*, 96–117. [[CrossRef](#)]
149. Dill, H.G.; Hansen, B.; Keck, E.; Weber, B. Cryptomelane: A tool to determine the age and the physical–chemical regime of a Plio-Pleistocene weathering zone in a granitic terrain (Hagendorf, SE Germany). *Geomorphology* **2010**, *121*, 370–377. [[CrossRef](#)]
150. Dill, H.G.; Wemmer, K. Origin and K/Ar age of cryptomelane-bearing Sn placers on silcretes, SE Germany. *Sediment. Geol.* **2012**, *275–276*, 70–78. [[CrossRef](#)]
151. Hautmann, S.; Lippolt, H.J. <sup>40</sup>Ar/<sup>39</sup>Ar dating of central European K–Mn oxides—A chronological framework of supergene alteration processes during the Neogene. *Chem. Geol.* **2000**, *170*, 37–80. [[CrossRef](#)]
152. Carl, C.; Dill, H. Age of secondary uranium mineralizations in the basement rocks of northeastern Bavaria, F.R.G. *Chem. Geol. Isot. Geosci. Sect.* **1985**, *52*, 295–316. [[CrossRef](#)]
153. Dill, H.G.; Gerdes, A.; Weber, B. Cu-Fe-U phosphate mineralization of the Hagendorf-Pleystein pegmatite province, Germany: With special reference to laser-ablation inductively-coupled plasma mass spectrometry (LA-ICP-MS) of limonite-cored torbernite. *Mineral. Mag.* **2007**, *71*, 371–387. [[CrossRef](#)]
154. Bryan, R.; Yair, A. Perspectives on studies of badland geomorphology. In *Badland Geomorphology and Piping*; Bryan, R., Yair, A., Eds.; Geobooks: Norwick, UK, 1982; pp. 1–12.
155. Dill, H.G.; Buzatu, A.; Balaban, S.-I.; Ufer, K.; Gómez Tapias, J.; Birgăoanu, D.; Cramer, T. The “badland trilogy” of the Desierto de la Tatacoa, upper Magdalena Valley, Colombia, a result of geodynamics and climate: With a review of badland landscapes. *Catena* **2020**, *194*, 104696. [[CrossRef](#)]
156. Gallaert, F.; Albert, S.; Puigdefabregas, J.; Lazaro, R. Badlands in the Mediterranean. In *Dryland Rivers: Hydrology and Geomorphology of Semi-Arid Channels*; Bull, L.J., Kirkby, M.J., Eds.; John Wiley & Sons: Hoboken, NJ, USA, 2002; Volume 10, pp. 299–326.
157. Howard, A.D. *Badlands*. In *Geomorphology of Desert Environments*; Abrahams, A.D., Parsons, A.J., Eds.; Springer: Dordrecht, The Netherlands, 1994; pp. 213–242.
158. Kasanin-Grubin, M.; Yair, A.; Nadal-Romero, E.; Vergari, F.; Troiani, F.; Desloges, J.; Yan, L.; Moreno de las Heras, M.; Della Seta, M.; Hardenbicker, U.M. The role of lithological properties on badland development. *Geophys. Res. Abstr.* **2019**, *21*, 1.
159. Nadal-Romero, E.; Martínez-Murillo, J.F.; Kuhn, N.J. *Badlands Dynamics in a Context of Global Change*; William Andrew Publishing: New York, NY, USA, 2018; p. 336.
160. Hayakawa, Y.S.; Matsukura, Y. Factors influencing the recession rate of Niagara Falls since the 19th century. *Geomorphology* **2009**, *110*, 212–216. [[CrossRef](#)]
161. Royden, L.; Taylor Perron, J. Solutions of the stream power equation and application to the evolution of river longitudinal profiles. *J. Geophys. Res. Earth Surf.* **2013**, *118*, 497–518. [[CrossRef](#)]
162. Twidale, C.R. Pediments and platforms: Problems and solutions. *Géomorphologie: Relief Process. Environ.* **2014**, *20*, 43–56. [[CrossRef](#)]
163. De Putter, T.; Ruffet, G.; Yans, J.; Mees, F. The age of supergene manganese deposits in Katanga and its implications for the Neogene evolution of the African Great Lakes Region. *Ore Geol. Rev.* **2015**, *71*, 350–362. [[CrossRef](#)]
164. Decrée, S.; De Putter, T.; Yans, J.; Moussi, B.; Recourt, P.; Jamoussi, F.; Bruyère, D.; Dupuis, C. Iron mineralisation in Mio-Pliocene sediments of the Tamra iron mine (Nefza mining district, Tunisia): Mixed influence of pedogenesis and hydrothermal alteration. *Ore Geol. Rev.* **2008**, *33*, 397–410. [[CrossRef](#)]
165. Maher, K.; Chamberlain, C.P. Hydrologic regulation of chemical weathering and the geologic carbon cycle. *Science* **2014**, *343*, 1502–1504. [[CrossRef](#)]

166. Riffel, S.B.; Vasconcelos, P.M.; Carmo, I.O.; Farley, K.A. Goethite (U–Th)/He geochronology and precipitation mechanisms during weathering of basalts. *Chem. Geol.* **2016**, *446*, 18–32. [[CrossRef](#)]
167. Shuster, D.L.; Vasconcelos, P.M.; Heim, J.A.; Farley, K.A. Weathering geochronology by (U–Th)/He dating of goethite. *Geochim. Cosmochim. Acta* **2005**, *69*, 659–673. [[CrossRef](#)]
168. Velasco, F.; Herrero, J.M.; Suárez, S.; Yusta, I.; Alvaro, A.; Tornos, F. Supergene features and evolution of gossans capping massive sulphide deposits in the Iberian Pyrite Belt. *Ore Geol. Rev.* **2013**, *53*, 181–203. [[CrossRef](#)]
169. Verhaert, M.; Bernard, A.; Dekoninck, A.; Lafforgue, L.; Saddiqi, O.; Yans, J. Mineralogical and geochemical characterization of supergene Cu–Pb–Zn–V ores in the Oriental High Atlas, Morocco. *Miner. Depos.* **2017**, *52*, 1049–1068. [[CrossRef](#)]
170. Verhaert, M.; Madi, A.; El Basbas, A.; Elharkaty, M.; Oummouch, A.; Oumohou, L.; Malfliet, A.; Maacha, L.; Yans, J. Genesis of As–Pb–Rich Supergene Mineralization: The Tazalaght and Agoujgal Cu Deposits (Moroccan Anti-Atlas Copperbelt). *Econ. Geol.* **2020**, *115*, 1725–1748. [[CrossRef](#)]
171. Abdullayev, E.; Leroy, S.A.G. Provenance of clay minerals in the sediments from the Pliocene Productive Series, western South Caspian Basin. *Mar. Pet. Geol.* **2016**, *73*, 517–527. [[CrossRef](#)]
172. Adriaens, R.; Zeelmaekers, E.; Fettweis, M.; Vanlierde, E.; Vanlede, J.; Stassen, P.; Elsen, J.; Śródoń, J.; Vandenberghe, N. Quantitative clay mineralogy as provenance indicator for recent muds in the southern North Sea. *Mar. Geol.* **2018**, *398*, 48–58. [[CrossRef](#)]
173. Ambers, R.K.R. Evaluation of clay mineralogy as a sediment provenance indicator in Virginia. *Southeast. Geol.* **2008**, *45*, 245–254.
174. Likiby, B.; Kabeyene, K.; Beyala, V.; Ngapgue, F.; Ndomé Effoudou, C.; Parisot, J.C.; Ekodeck, G.E. Geochemistry and duricrusting of the weathering products on granite at Djoulgouf in the Lake Chad basin. *Syllabus Rev.* **2010**, *2*, 1–8.
175. Peel, M.C.; Finlayson, B.L.; McMahon, T.A. Updated world map of the Köppen–Geiger climate classification. *Hydrol. Earth Syst. Sci.* **2007**, *11*, 1633–1644. [[CrossRef](#)]
176. Schuler, U.; Baritz, R.; Willer, J.; Dill, H.G. *A revised approach to classify parent material for soil mapping. e-Soter, Version 1.3*; Federal Institute for Geosciences and Natural Resources: Hannover, Germany, 2010; p. 129.
177. Arancibia, G.; Matthews, S.J.; Pérez de Arce, C. K–Ar and  $^{40}\text{Ar}/^{39}\text{Ar}$  geochronology of supergene processes in the Atacama Desert, Northern Chile: Tectonic and climatic relations. *J. Geol. Soc.* **2022**, *163*, 107–118. [[CrossRef](#)]
178. Belogub, E.V.; Novoselov, K.A.; Yakovleva, V.A.; Spiro, B. Supergene sulphides and related minerals in the supergene profiles of VHMS deposits from the South Urals. *Ore Geol. Rev.* **2008**, *33*, 239–254. [[CrossRef](#)]
179. Bouchard, M.; Jolicoeur, S. Chemical weathering studies in relation to geomorphological research in southeastern Canada. *Geomorphology* **2000**, *32*, 213–238. [[CrossRef](#)]
180. Maksaev, V.; Townley, B.; Palacios, C.; Camus, F. Metallic ore deposits. In *The Geology of Chile*; Moreno, T., Gibbons, W., Eds.; The Geological Society of London: London, UK, 2008; p. 414.
181. Warren, I.; Archibald, D.A.; Simmons, S.F. Geochronology of epithermal Au–Ag mineralization, magmatic–hydrothermal alteration, and supergene weathering in the El Peñón District, Northern Chile. *Econ. Geol.* **2008**, *103*, 851–864. [[CrossRef](#)]
182. Xu, W.; Tosca, N.J.; McLennan, S.M.; Parise, J.B. Humidity-induced phase transitions of ferric sulfate minerals studied by in situ and ex situ X-ray diffraction. *Am. Mineral.* **2009**, *94*, 1629–1637. [[CrossRef](#)]
183. de Lima, G.G.; Marçal, M.; de Barros Correa, A.C.; de Lima, F.J. Landscape evolution of the Salamanca watershed, Araripe Plateau: Insights from a river channel morphological classification. *J. S. Am. Earth Sci.* **2021**, *107*, 103013. [[CrossRef](#)]
184. de Oliveira, M.A.T.; Santos, J.C.; Lemos, R. 80,000 years of geophysical stratigraphic record at the Serra da Capivara National Park, in northeastern Brazil: Uncovering hidden deposits and landforms at a canyon’s floor. *J. S. Am. Earth Sci.* **2020**, *104*, 102691. [[CrossRef](#)]
185. Grigorian, S.V. *Secondary Lithochemical Halos in Prospecting for Hidden Mineralization*; Nedra Publishing House: Moscow, Russia, 1985; p. 176.
186. Liu, L.-M.; Peng, S.-L. Prediction of hidden ore bodies by synthesis of geological, geophysical and geochemical information based on dynamic model in Fenghuangshan ore field, Tongling district, China. *J. Geochem. Explor.* **2004**, *81*, 81–98. [[CrossRef](#)]
187. Mahdiyanfar, H.; Farzaman, M. Identification of hidden mineralized and non-mineralized zones using spectral analysis of geochemical data. *Int. J. Min. Geo-Eng.* **2021**, *55*, 81–89.
188. Richards, J. Clues to hidden copper deposits. *Nat. Geosci.* **2016**, *9*, 195–196. [[CrossRef](#)]

**Disclaimer/Publisher’s Note:** The statements, opinions and data contained in all publications are solely those of the individual author(s) and contributor(s) and not of MDPI and/or the editor(s). MDPI and/or the editor(s) disclaim responsibility for any injury to people or property resulting from any ideas, methods, instructions or products referred to in the content.